Study on the Mechanical and Electrical Properties of Boron Nitride Nanotube-based Materials by *in situ* Transmission Electron Microscopy

Xin ZHOU

October 2019

Study on the Mechanical and Electrical Properties of Boron Nitride Nanotube-based Materials by *in situ* Transmission Electron Microscopy

Xin ZHOU

Doctoral Program in *Materials Science and Engineering*

Submitted to the Graduate School of

Pure and Applied Sciences

in Partial Fulfillment of the Requirements

for the Degree of Doctor of Philosophy in

Engineering

at the

University of Tsukuba

Contents

List of abbreviations

BNNTs	Boron nitride nanotubes
CNTs	Carbon nanotubes
CVD	Chemical vapor deposition
TEM	Transmission electron microscopy
SEM	Scanning electron microscopy
AFM	Atomic force microscopy
HRTEM	High-resolution transmission electron microscopy
EBID	Electron-beam-induced deposition
EELS	Electron energy loss spectroscopy
1D	1-dimensional
STM	Scanning tunneling microscopy
BOCVD	Boron and metal oxides assisted chemical vapor deposition
NASA	National Aeronautics and Space Administration
XRD	X-ray diffraction
SAED	Selected area electron diffraction

Chapter 1

Introduction

1.1 Hexagonal boron nitride nanotubes (h-BNNTs)

In history, hexagonal boron nanotubes were developed along with their counterparts-carbon nanotubes (CNTs). Structurally, BNNTs are regarded as analogs of CNTs, with alternating boron and nitrogen atoms substituting carbon atoms in the hexagonal lattice network (**Figure 1.1a** and **b**).[1-7] It's well-known that all the properties of a material depend on its structure. As expected, BN and carbon nanotubes possess some identical intrinsic characteristics, such as excellent mechanical properties[8-12] and thermal conductivity.[13-16] Both theoretical prediction and experimental measurements revealed that their elastic modulus can reach a TPa level and thermal conductivity can reach thousands of $W \cdot m^{-1} \cdot K^{-1}$at room temperature.[17-19] Despite these similarities, for a B-N bond, valence charges are concentrated around the N atoms because of different electronegativities of B and N atoms. This fact makes such a heteroatom bond to show a mixed covalent-ionic bonding character. In contrast, charge density is equally distributed around C atoms for a C-C bond, which possesses a purely covalent behavior (**Figure 1.1c** and **d**).[20] As a consequence, BNNTs show distinct physical and chemical properties compared to CNTs. For instance, BNNTs are highly electrical insulating with a bandgap of ~5.5 eV,[21,22] while CNTs could be semi-conducting or metallic depending on their chirality.[23-25] In addition, BNNTs present specific properties different from CNTs, such as high chemical stability,[26] oxidation resistance (up to ~ 900 ℃),[27-29] large neutron capture cross-section[30,31] as well as piezoelectricity.[32-34] The comprehensive comparison between BNNTs and CNTs is summarized in **Table 1.1**. Owing to all these fascinating properties, BNNTs have attracted tremendous attention in a variety of practical applications, such as mechanical reinforcement of composites,[35-37] insulating thermal conductors,[35-37] dielectric gates,[38,39] protective coatings/shields and so on.[38,39]

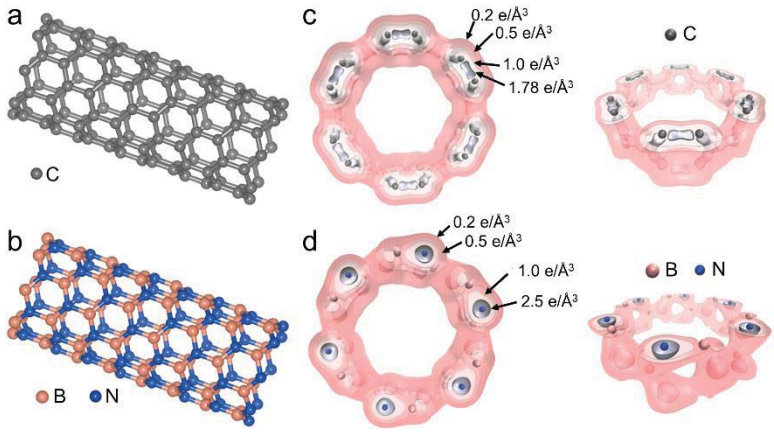

Figure 1.1 (a) and (b) Structural models of single-wall CNT and BNNT, respectively. (c) and (d) Total valence electron distributions of a (6,6) CNT and BNNT at various isovalues of charge densities as indicated, respectively

Table 1.1 Comparison of the main properties of BNNTs and CNTs

Properties	BNNTs	CNTs
Bond length (Å)	1.47	1.42
Bond energy (eV)	4.0	3.7
Elastic modulus (TPa)	0.5-1.3	0.8-1.5
Thermal conductivity at 25 ℃ (10^3 W·m^{-1}·K^{-1})	0.5-2.4	2.0-6.0
Oxidation resistance (℃)	~900.0	~600.0
Bandgap (eV)	~5.6	~0
Appearance	white	black

1.2 Synthesis of BNNTs

Obviously, the massive production of BNNTs with high quality and purity comes first to realize their applications in practical environments. Since the pioneering work on the first synthesis of BNNTs reported by Chorpa *et. al via* applying the arc-discharge method,[40] many approaches have been established to achieve large scale and high-quality synthesis of BNNTs, including, but not limited to chemical vapor deposition (CVD),[41,42] ball milling method[43,44] and plasma jet method.[45,46] With the development of synthesis methods, researchers gradually achieved the high production rate (35 g/h), and high yield (up to 80% against existing by-products) synthesis of BNNTs.

1.2.1 Arc discharge method

Following the widely used arc discharge method to prepare CNTs, Chopra *et al.* firstly adopted this method to successfully synthesize BNNTs in 1995.[40] In their design, a hollow tungsten electrode with an h-BN rod inside was used as a compound anode, and a pure copper electrode was used as a cathode. The as-obtained BNNTs had multi-wall structure, with inner diameter around 1 to 3 nm, outer diameter around 6 to 8 nm, and lengths exceeding 200 nm, **Figure 1.2a**. However, some metal particles were found in the nanotube, **Figure 1.2b**. Then, Loiseau *et al.* modified this system by replacing the anode with hafnium diboride (HfB_2) rods, and graphite used as a cathode, in order to improve the arc process. BNNTs with only one or two walls were prepared using this method, **Figure 1.2c**. Most of the tubes had closed ends, while some of them revealed triangular facets at the caps, which can be ascribed to three 120° disclinations, as shown in **Figure 1.2d and e**. Then, Narita *et al.*,[47] Cumings *et al.*[48] and Yeh *et al.*[49] reported the BNNTs synthesis by applying a similar method but using different materials as cathodes and anodes. However, there were still two main drawbacks for the arc discharge process, (i) low purity with respect to carbon contamination and metal particles residual, since graphite and metal electrodes were used; (ii) limited yields, as the reaction zone at the arc core was confined in a small zone.

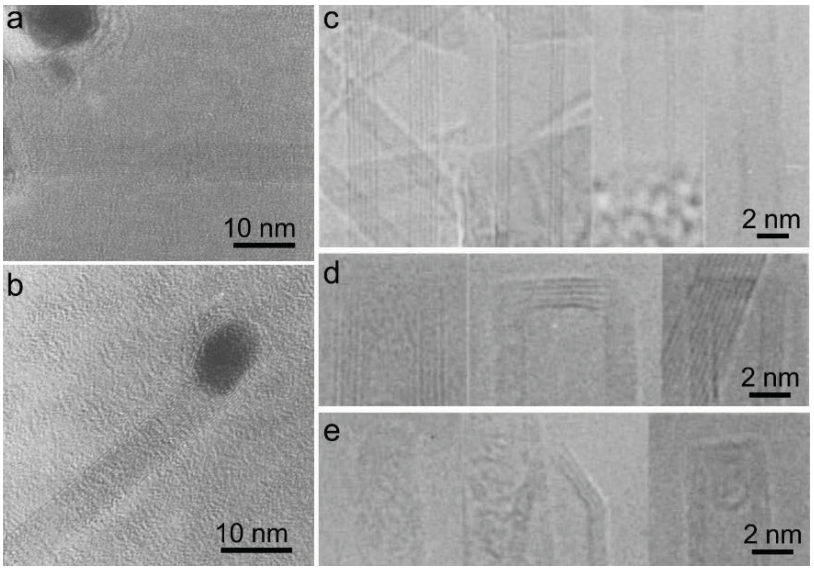

Figure 1.2 (a) and (b) HRTEM images of the multi-wall BNNTs. A metal particle is seen in (b). (c-e) HRTEM images showing BNNTs with a different number of walls and shapes of tube ends, respectively.

1.2.2 Ball milling method

The ball milling method is a mature and widely used approach to achieve industrial scale synthesis of various kinds of materials. Chen *et al.* used boron powder as a starting material, milled it under ammonia gas atmosphere for 150 h, then annealed the powder at a temperature $\geqslant$1000 ºC under N_2 or Ar atmosphere to prepare BNNTs.[50] The product had outer diameter of tens of nanometers, with a dominant phase of h-BN and an impurity phase of iron boride ($Fe_{2.12}B_{103.36}$). Later, they achieved millimeter scale BNNTs at a large scale *via* the optimized ball milling and annealing process and found that the annealing temperature had played an essential role in the growth of BNNTs.[51] TEM characterization showed that the BNNTs had a bamboo-type

structure and iron particles at the ends of tubes (**Figure 1.3**). In addition, it was found that the regarded metal particles, as well as appropriate milling condition are crucial for the production of high yield BNNTs. Though the yields were remarkably improved (> 85%), it should be pointed out that the purity had still been relatively low. The tubes commonly contained amorphous boron and metal particles.

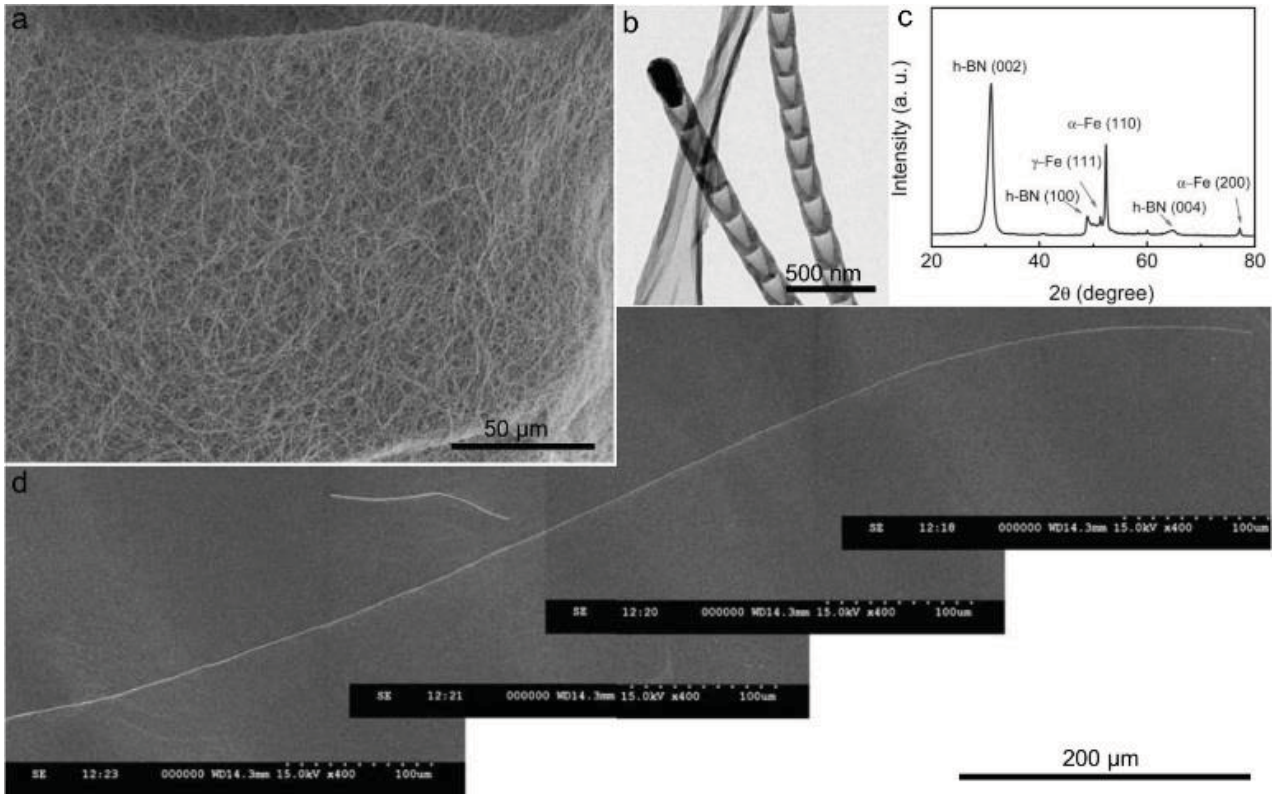

Figure 1.3 (a) and (d) Scanning electron microscopy (SEM) images of BNNTs. (b) TEM image showing the bamboo-like structure of the BN sample. (c) X-ray powder diffraction (XRD) pattern of BNNTs, showing the existence of iron impurity.

1.2.3 Chemical vapor deposition (CVD) method

Chemical vapor deposition (CVD) method is the most commonly adopted approach for thin film deposition was also used to prepare BNNTs with high purity and crystallinity. In this method, boron or boron nitride acted as a boron source, ammonia gas as a nitrogen source, and transition metals as catalysts to produce BNNTs. Tang *et al.* reported the gram scale synthesis of BNNTs through the reaction between B, MgO and NH_3 gas within a temperature range of 1000 ºC to 1700 ºC in a high-frequency induction furnace.[52] The nanotubes obtained in this way had a diameter around tens of nanometers and a length of dozens of micrometers. No carbon contamination or metal residuals were found, implying the high quality of the samples. Later, additional experimental results revealed that substituting MgO with other metal oxides, like FeO, Li_2O, and Ga_2O_3 could also realize the high yield synthesis of BNNTs (**Figure 1.4a-c**). Then, Lee *et al.* realized the preparation of BNNTs by using the similar starting raw materials inside a conventional horizontal furnace having a quartz tube vacuum chamber.[53] The as prepared BNNTs had a similar structure size as in previous reports and had a band-gap of ~5.9 eV, as was estimated from the UV-vis absorption spectra. (**Figure 1.4d-h**). Later, they realized

the pattern growth of BNNTs and confirmed that BNNTs are good insulators.

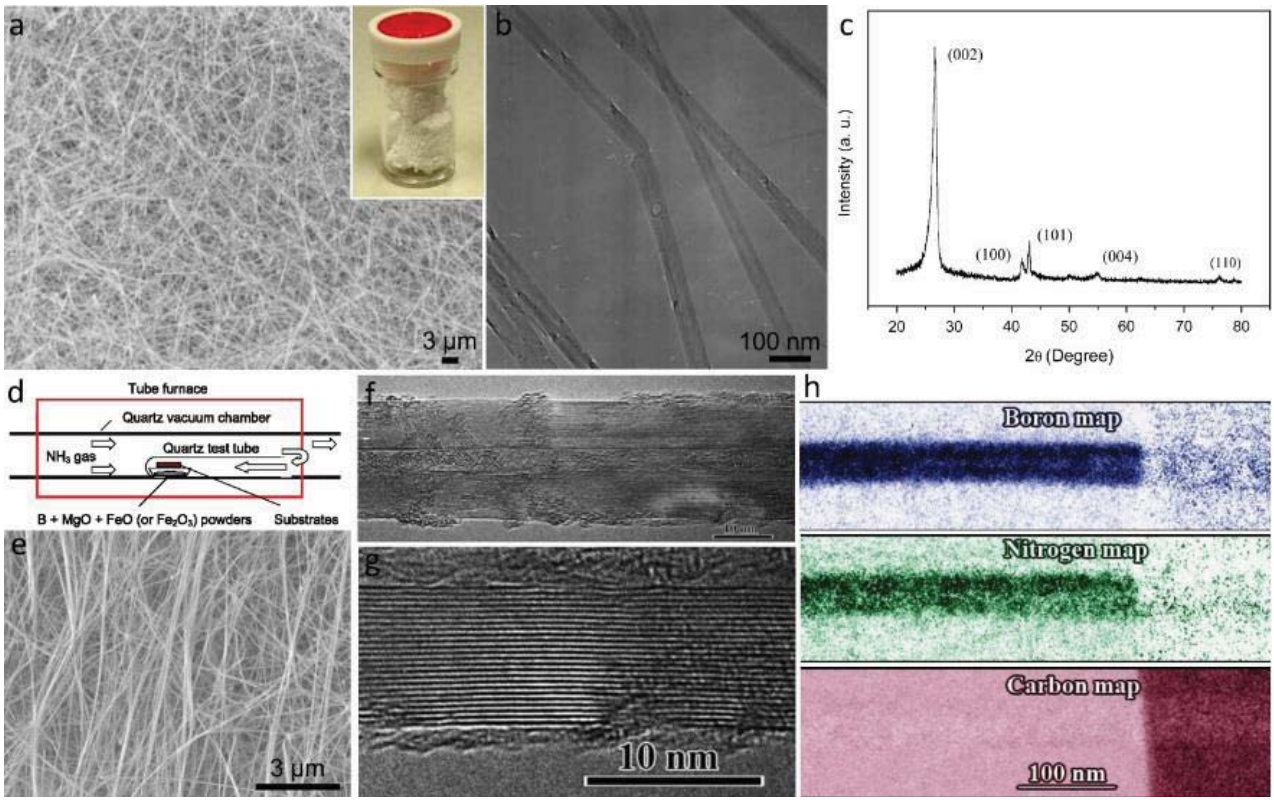

Figure 1.4 (a) and (b) SEM and TEM images of BNNTs, no metal particles were detected. (c) XRD pattern of BNNTs, showing no impurities. Inset of (a) is a photograph of BNNTs of white color appearance. (d) Schematic illustration of the BNNTs synthesis inside a horizontal furnace. (e-g) Electron microscopy of BNNTs. (h) Energy filtered imaging showing that these nanotubes consist of boron and nitrogen atoms, and have no carbon.

1.2.4 Plasma jet method

Though CVD provided the large-scale synthesis of BNNTs with high quality, the production rate was still limited, only around several milligrams per hour. Thus, scalable and quick synthesis of BNNTs became a hot pursuit for the scientific community. Shimizu *et al.* proposed a plasma jet method to prepare BNNTs. Various kinds of structures, like nanotubes, webs and amorphous phase were formed using this strategy.[54] Later, researchers at the National Research Council Canada achieved the preparation of BNNTs at a significantly high rate of ~20g/h through a similar method and using hydrogen as catalyst instead of the metal catalysts. The as-obtained BNNTs had small diameter (~ 5 nm) with several walls of high crystallinity. (**Figure 1.5a** and **b**). Then, Fathalizadeh *et al.* further improved the production rate to 35g/h by using inductively-coupled plasma system (EPIC).[45] Their results also showed a high yield (up to 80%) of pure BNNTs, with outer diameter spanning from 4 to 6 nm and wall number ranging from 2 to 6. (**Figure 1.5c-e**)

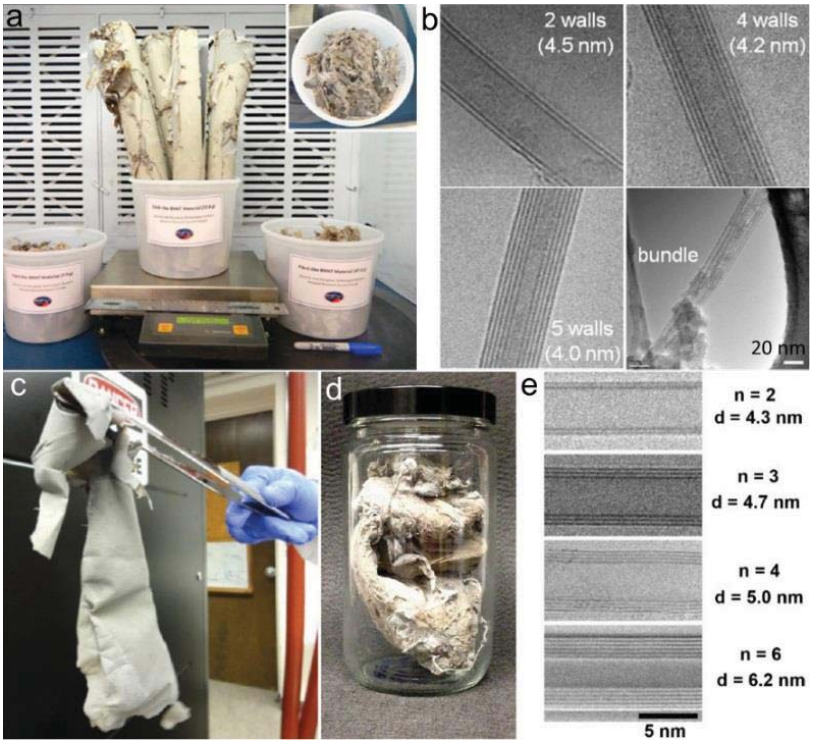

Figure 1.5 (a) 192 g of BNNTs collected from a single experiment, demonstrating a production rate of 20 g/h. (b) TEM images of individual BNNTs and BNNT bundle. (c-d) BNNTs obtained after a further improvement of yield rate to 35g/h. (e) TEM images showing that BNNTs have wall numbers spanning from 2 to 6 nm.

1.3 Mechanical properties and applications of BNNTs

Then, the properties and related applications of BNNTs came into the spotlight. Among these attractive properties, the excellent mechanical performances of BNNTs, including high specific modulus (~500 GPa/(g/cm^3) and high specific strength (~20 GPa/(g/cm^3), which are comparable to CNTs but much higher than those of the metals and their alloys at room temperature, were particularly noticed. (**Figure 1.6a**) Most importantly, even at high temperature (700 ºC), BNNTs still maintain these characters, while CNTs and most of the metals lost all their mechanical features.[55] (**Figure 1.6b**) Owing to these excellent mechanical properties, BNNTs are regarded as important candidates for mechanical applications, especially in extreme environments, such as high temperature and oxidative atmosphere. For example, Bhuiyan *et al.* reported that BNNTs reinforced titanium (Ti) matrix composites exhibited a higher compressive strength than that of pure Ti both at room and high temperature (500 ºC).[56] In addition, the National Aeronautics and Space Administration (NASA) proposed that BNNTs can be used for space applications because of their light-weight nature and good shielding capability, the important concept is the space application.[55] All these facts suggest the importance of studying the mechanical properties of BNNTs to further clarify on their applications.

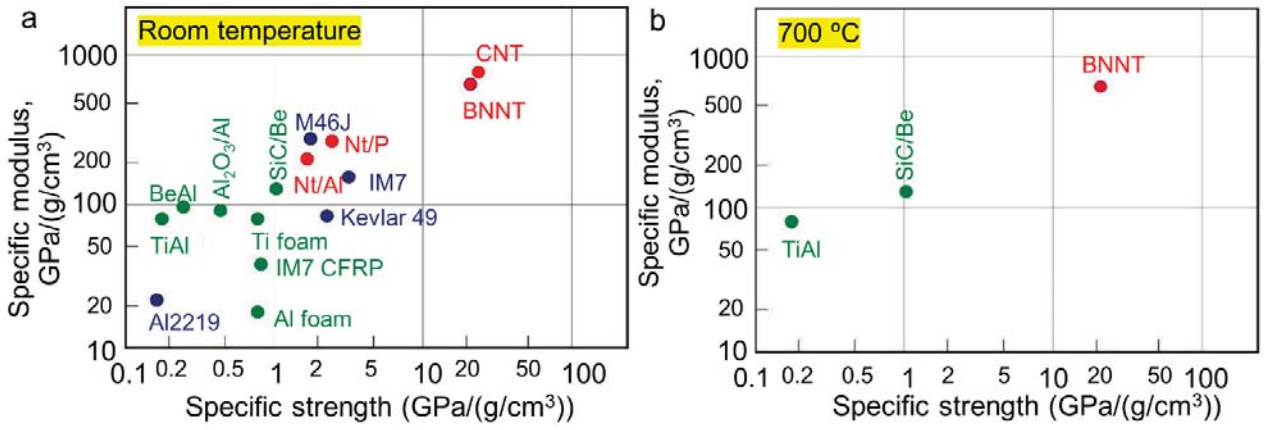

Figure 1.6 Comparison of mechanical properties of several aerospace materials, CNTs and BNNTs at (a) room temperature and (b) 700 ℃, showing the excellent mechanical properties of BNNTs both at room and high temperatures.

1.4 Transport properties and applications of BNNTs

Despite the fact that BNNTs are structurally similar to CNTs, they have totally opposite transport properties. The bandgap of BNNT is about 5.6 eV, and it is almost not related to the tube morphology.[57] Therefore, BNNTs are normally electrical insulating. By contrast, CNTs are metals or semiconductors, the transport properties highly depend on tubes' helicity. In the meantime, theoretical calculations have shown that deformation or decrease in tube diameter down to 0.4-1 nm or less, or application of a transverse electric field (Stark effect), can remarkably reduce the bandgap, thus further affecting their transport behaviors.[58] For instance, through the computation in the frame of local density approximation (LDA), the bandgap of a single wall BNNT can be reduced to 2.25 eV under a transverse electrical field of 0.1 V/ Å. In terms of a single-layered BNNT with an intrinsic bandgap of 4.5 eV, a transverse electric field of 0.1 V/Å was found to reduce the bandgap to 2.25 eV, whereas a field of 0.19 V/Å even eliminated the bandgap entirely.[58] Furthermore, Mele and Kral predicted a piezoelectric behavior in BNNTs and calculated the piezoelectric constants, which were found to be essentially saturated in BNNTs.[59,60] All these striking theoretical predictions have paved the way to the real piezoelectric devices based on BNNTs. In addition, BNNTs can emit electrons into a vacuum when an external electric field is applied and concentrated at the tip of the tube. Such kind of field emission (FE) phenomena appeared at a very low external electric field, which makes BNNTs good candidates for displays.[61]

1.5 Developing approaches to measure the electro-mechanical properties at nanoscale

When the material structure decreases to a nanoscale size, the questions on how to 'see, fix, manipulate, apply load' to the target become critical with respect to getting a deep insight into its properties. In the meantime, with further explorations, it's been revealed that the size, crystal orientations, interfaces, as well as defects play essential roles in determining the mechanical properties of a nanomaterial. With the development of modern characterization techniques, corresponding measurement systems have been designed to evaluate

the electro-mechanical behaviors of one-dimensional (1D) materials in micro- or nano size, including *in situ* SEM, *in situ* AFM, as well as *in situ* TEM methods.

1.5.1 *In situ* SEM method

In 2000, Yu *et al.* reported the tensile test of individual carbon nanotubes inside a scanning electron microscope.[62,63] Their experimental setup consisting of two AFM tips with different force constants (K_c) used as soft (K_{c1}<0.1N·m^{-1}) and rigid (K_{c2}>10 N·m^{-1}) cantilevers. (**Figure 1.7a**) Individual CNTs were picked up and fixed on each end of the AFM tips. (**Figure 1.7b**) The tensile load was applied by moving the rigid AFM tip, which is controlled by a piezotube. Then accurate value of the force (F) can be obtained by recording the deflection distance (d) of the soft cantilever and the length change (ΔL) of CNTs can be obtained simultaneously *via* the SEM observation. Finally, the stress (σ) and strain (ε) were determined as follow:

$$\sigma = \frac{F}{A} = \frac{K_{c1} \cdot d/cos\theta}{A} \quad (1.1) \text{ and } \varepsilon = \frac{\Delta L}{L} \quad (1.2)$$

where A and L are the cross-section area and original length of the selected nanotubes, respectively. θ is the angle between the direction of the cantilever deflection and the tube axis. After analyzing the stress-strain curve of 19 nanotubes, an average Young's modulus ranging from 270 to 950 GPa was calculated for the outermost layers. (**Figure 1.7c**) Different mechanical properties of various materials, like Si nanowires,[64,65]ZnO nanowires,[66] Co nanowires,[67] SiC nanowires, [68,69] Ag nanowires,[70] were studied through tensile tests inside an SEM.

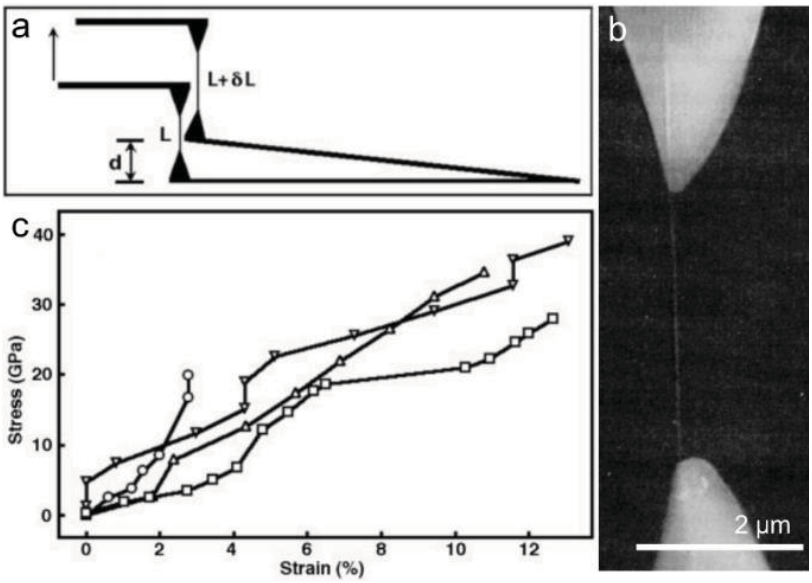

Figure 1.7 (a) Illustration of the experimental setup for tensile test on a single CNT. (b) SEM image showing a CNT clamped between two opposite AFM tips. (c) Plots of stress-strain curves for different CNTs.

1.5.2 *In situ* AFM method

Atomic force microscopy is the most commonly used equipment to conduct mechanical measurements on different kinds of materials, such as ta three-point bending test and a cantilever bending test. Wu *et al.* designed

an AFM-based system to perform a three-point bending test on Au nanowires.[71] Au nanowires were clamped to the trench edges by electron-beam-induced deposition of Pt lines. Trenches with a width of 0.3- 4 μm and a depth of 250-500 nm were fabricated on the SiO_2 substrate *via* focus-ion-beam milling. (**Figure 1.8b** and **c**) Then, lateral load (*F*) was applied to the Au wire by AFM tip sweeping, and the lateral deflection (*d*) of the cantilever was recorded using a four-quadrant photodiode. (**Figure 1.8a**) Finally, Young's modulus (*E*) of Au wire was obtained from the *F-d* curve.

$$E = \frac{FL^3}{196dI} \quad (1.3)$$

Where *L* is the suspended length subjected to a load *F*, *r* is the wire radius, and $I=(\pi r^4)/4$ is the area moment of inertia of the wire. The authors found that the results had been consistent with the classic beam-bending theory. The elastic modulus of Au wires was determined to be 70 ±11 GPa, independent of their sizes. While, the yield strengths for 40 nm Au wires were 5.6±1.4 GPa, larger than that of 200 nm Au wires, implying the diameter-dependent behavior. (**Figure 1.8d**) *Via* applying this method, mechanical properties of various 1D nanomaterials were evaluated, including carbon naotubes,[72] GaN nanowires,[73] Si nanowires,[74,75] ZnO nanowires,[76-79] Germanium nanowires,[80] and so on.

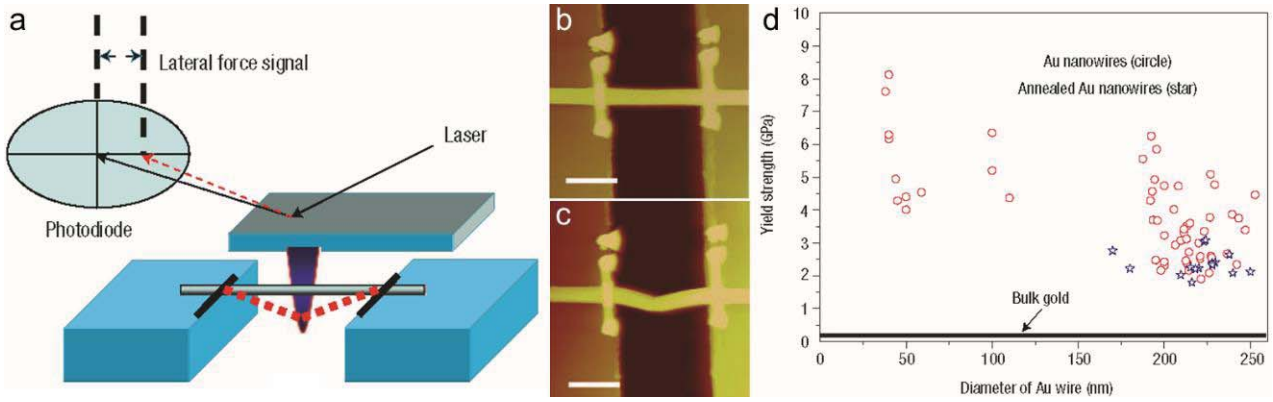

Figure 1.8 (a) Schematic of a bending test on a fixed Au wire. (b) and (c) AFM images of the Au wire after elastic and plastic bending, respectively. (d) Relationship between the yield strength and Au wire diameter.

1.5.3 *In situ* TEM method

Although *in situ* methods based on SEM or AFM setups witnessed success in the evaluation of mechanical properties of 1D materials, there have still been several disadvantages. The main one is the difficulty in estimating the structural information directly, like the growth orientation, defects, *etc.* By contrast, these problems could perfectly be solved inside a TEM because of its high resolution, and capability of using electron diffraction to analyze the crystal structure. Thus, an atomic force microscope (AFM) system was integrated within the TEM holder (AFM-TEM holder) and utilized to analyze the mechanical behavior of nanomaterials.[53-56] For instance, Tang *et al.* reported the deformation and fracture mechanisms of Si nanowires under uniaxial tension.[85] A Si nanowire was selected and clamped on the tip of a W probe and then transferred to the AFM-TEM holder. (**Figure 1.9a**) The opposite end of Si nanowire was firmly fixed to the AFM

cantilever by using the electron-beam-induced deposition (EBID). Similar to *in situ* SEM tensile test, the elongation of nanowire and the cantilever displacement was recorded *via* moving the W probe backward. (**Figure 1.9b**) Stress-strain curves revealed that the nanowires deformed elastically until abrupt brittle fracture. (**Figure 1.9c**) The elastic modulus of Si nanowires was estimated to be ~201 GPa on average and their strength showed a clear size-dependent behavior, *i.e*., strength decreases along with an increase of wire diameters.

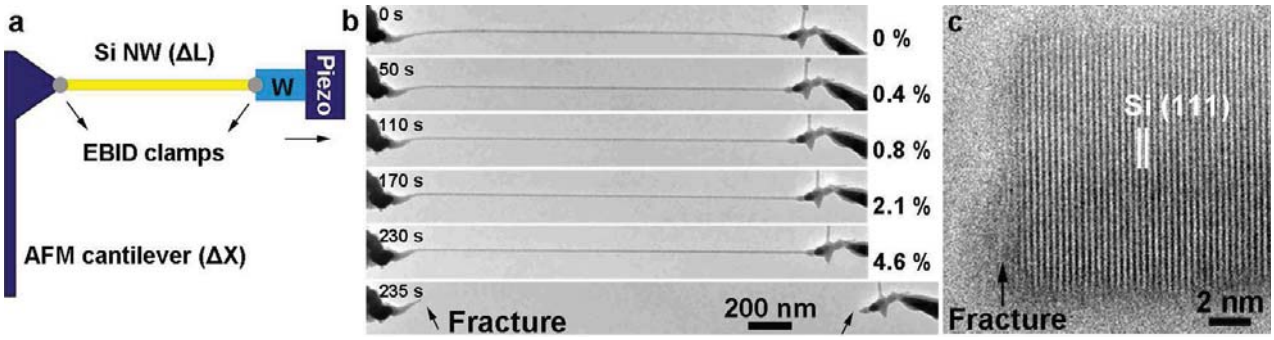

Figure 1.9 (a) Schematic of the tensile test on a Si nanowire by using the AFM-TEM holder. (b) Elongation of a nanowire under different strains and the final fracture. (c) HRTEM image of the fracture surface of Si nanowire.

As for the AFM-TEM holder system, one of the obstacles is the difficulty in obtaining the exact alignment between the cantilever and the sample during the tensile test. In order to overcome these drawbacks, in 1996, Treacy *et al.* first reported the elastic modulus measurements on individual CNTs by a thermal-induced vibration method inside TEM.[86] Their results showed a huge distribution range of the moduli, from 0.4 TPa to 4.1 TPa, and an exceptionally high value of 1.8 TPa on average. Being limited by a small vabriation amplitude and the difficulty in accurate estimation of local temperature, the precision was not satisfactory. Then, in 1999, Poncharal *et al.* developed an electrical-field-induced vibration method to evaluate the mechanical behavior of CNTs. In their design, CNTs were clamped to one electrode and inserted into a TEM holder, a metal probe was used as a counter electrode. An alternating current (*AC*) sinusoidal signal was applied between the two electrodes, and mechanical resonance was activated *via* tuning the signal frequency. Based on the classic Euler-Bernoulli beam theory, the modulus (*E*) of the test specimen is given by:

$$E = \frac{\rho A L^4}{I}\left(\frac{2\pi f_i}{\beta_i{}^2}\right)^2 \quad (1.4)$$

Where ρ, A, L and I are the mass density, cross-section area, length and moment inertia of the speciment, respectively, f_i is the resonance frequency at the *ith* order and β_i is a constant for the *ith* order resonance. It's obvious all the related parameters for measuing the modulus can be easily obtained from TEM observation. Up to 2nd order harmonic resonace of an individual CNT was observed by the authors and the extimated bending moulus of CNTs showed a size-depend behavior, *i.e.* modulus decreasing along with the increasing of CNTs diameter. (**Figure 1.10 a-c**) Thus this resonance method was widely adopted in electron microscopy to evaluate the elasticity of materials.[87-96]

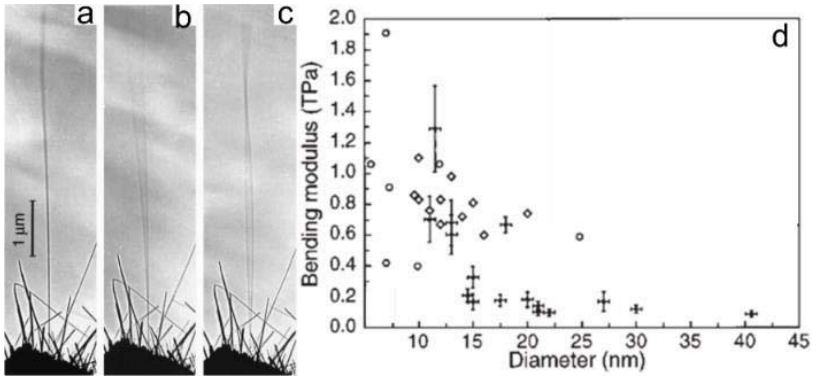

Figure 1.10 (a-c) TEM images showing the original view and the resonance of an individual CNT; (d) The measured bending modulus distribution as a function of tube diameter

1.5.4 Advantages of *in situ* TEM method

In situ TEM based method stands out of the other methods for evaluation of electro-mechanical properties on account of the numerous advantages it has. These are namely:

(1) High spatial resolution. Conventional TEM usually has a nanometer resolution, which is much superior to a conventional SEM or an optical microscope. Thus, this allows for a high precision determination of the structure parameters, like the length, and cross-section area of the sample, both parameters are important for determining the electro-mechanical properties of a nanoscale object.

(2) Knowledge of pre-existing defects, crystalline structure, elemental composition, and species distribution, and surface quality of the specimen. All these make it possible to understand the effects of defects and crystallographic orientations on the mechanical properties of the target sample.

(3) Precise measurements of forces and displacements/strains. The development of modern micro-electromechanical systems (MEMS) allowed us to determine the applied load/force with an nN precision.

(4) Real-time or near real-time observation of the measurement process. This is essential to understand the cause-effect relations, structural variation, as well as the mechanisms of fracture or failure, thus making it possible to establish the property-structure-process relationship.

1.6 Motivations and objectives of this study

BNNTs have attractive electro-mechanical properties and are fully applicable for *in situ* TEM techniques to further explore their physical properties and functions. There are several unsolved issues with respect to BNNTs related research.

(1) Intrinsic elastic properties have not been precisely determined.

Though theoretical calculations have shown that the elastic modulus of BNNTs is around 1 TPa,[10,97-100] precise experimental measurements are largely lacking. Up to now, several groups have reported on Young's moduli evaluation of individual BNNTs, however, their results exhibited wide-scattered data with large a

modulus distribution range, from ~500 to ~1500 GPa, and large standard deviation. (**Figure 1.11a-c**) Importantly, why the moduli exhibited such a large distribution range? Is it originated from the measurement methods or the imperfection of the materials? Thus, it is important to develop a high precision method to evaluate the modulus of BNNTs and correlate them with their microstructures.

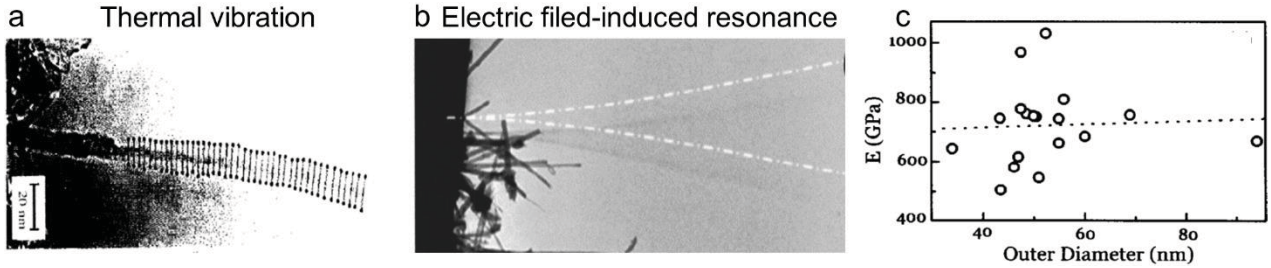

Figure 1.11 (a) and (b) TEM images of 1st order resonances of individual BNNTs excited by thermal and electric field-induced method, respectively. (c) Corresponding moduli distribution obtained from the method used in (b).

(2) The extrinsic effects on the electro-mechanical properties of BNNTs are not well understood.

(2.1) Effects of extrinsic defects are not properly studied.

National Aeronautics and Space Administration (NASA) has reported that BNNT is a promising candidate for shielding space irradiation due to its large neutron capture cross-section. However, it is undoubtable that the knock-out collision caused by cosmic rays will introduce defects in the materials and deteriorate the overall material properties. Thus, it is critical to reliably assess the BNNT shielding capability and to study the effects of possible radiation-induced defects on the mechanical properties. Previously, electron irradiation has been used to mimic the irradiation process, create structural defects in BNNTs and the mechanisms for the defects generation, and their growth was widely studied.[103-107] (**Figure 1.12**) However, the relation between the defect structure and the elastic properties has not been established.

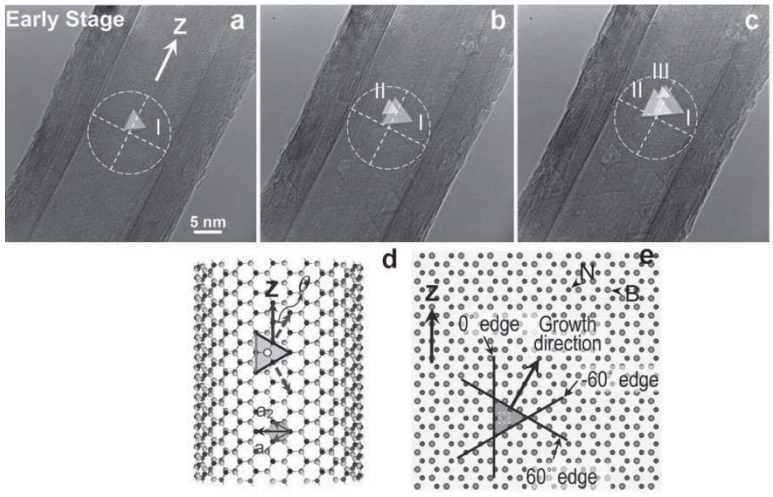

Figure 1.12 (a-c) TEM images showing the introduction and growth of triangle-shaped vacancy defects under different irradiation stage. (d) Schematic illustration of a single vacancy in a single BNNT. (e) Schematic

illustration of the growth direction of the irradiation-induced vacancy.

(2.2) Effects of composition-heterostructure design.

BNNTs, CNTs, and metals are indeed good candidates for mechanical and electrical applications. However, all of them have constant elastic moduli and electrical conductivities, which cannot be easily and widely tuned. Furthermore, there are still big gaps between adjustments of mechanical and electrical properties for a given material. (**Figure 1.13**)[108] Thus, designing materials with tunable physical properties to cover these gaps will be promising to accomplish diverse applications. One prospective approach to achieve this goal is to fabricate BN-C heterostructures, usually regarded as nanoscale "Lego" blocks, and provide the engineers with diverse possibilities for tuning properties and promoting advanced applications.

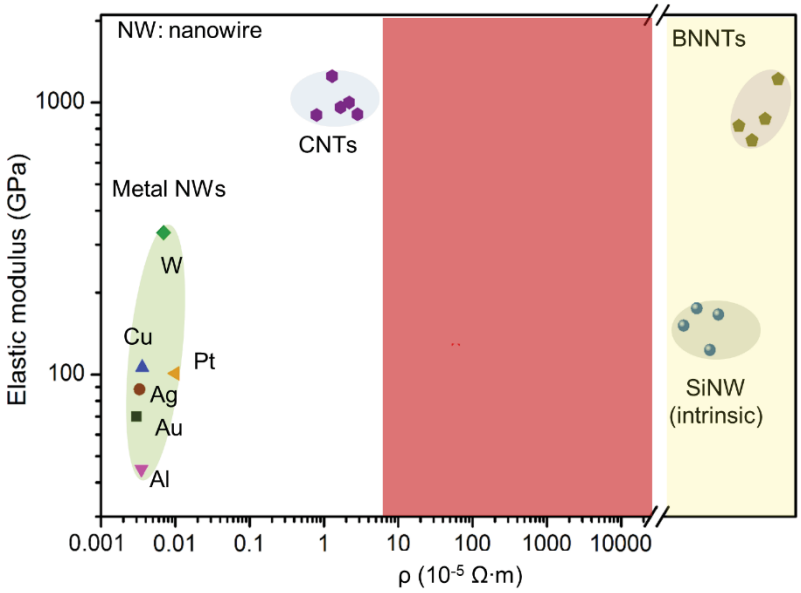

Figure 1.13 Elastic moduli and electric resistivities for various nanostructured materials.

(3) Electrical and mechanical responses to the external deformation are still not clear.

Though enormous progress has been achieved on designing the BNNT-based heterostructures, for instance, Xiang *et al.* have reported a BN@C heterostructure to modulate their properties,[109] several questions remain not answered, *e.g.* (i) What kind of transport properties such heterostructure would have? (ii) What are the bending effects on their electrical behavior? (iii) How such heterostructures would bare a heavy bending deformation? (iv) Would BN and C tubular domains separate or their interface break under bending; and if yes, how this would affect the overall structural integrity and physical properties? All these issues call for a direct study on bending deformation of coaxial hybrid BN-C nanotubes.

In this Thesis, a high-order electric-filed-induced resonance method was developed to precisely evaluate the elastic moduli of BNNTs, which is crucial for their practical mechanical applications. Then, external defects were deliberately introduced into the BNNTs by using the electron beam irradiation, to understand the influence of the external defect on modulating their mechanical properties and estimation their shielding capability. Subsequently, novel BN-C coaxial nanotubes were designed and synthesized to realize the simultaneous tuning of the elastic moduli

and electrical conductivity in a wide range, which fills the big gaps between metals, CNTs, and BNNTs. Finally, the kinking behavior and transport properties to the applied forces were studied with respect to their structural integrity and the electrical conducting stability, to further verify their potential applications in the modern flexible devices.

1.7 References

(1) Golberg, D.; Bando, Y.; Tang, C. C.; Zhi, C. Y. Boron Nitride Nanotubes. *Adv. Mater.* **2007**, 19, 2413-2432.

(2) Cohen, M. L.; Zettl, A. The Physics of Boron Nitride Nanotubes. *Phys. Today* **2010**, *63* (11), 34-38.

(3) Andrews, R.; Jacques, D.; Qian, D. L.; Rantell, T. Multiwall Carbon Nanotubes: Synthesis and Application. *Acc. Chem. Res.* **2002**, *35* (12), 1008-1017.

(4) Fischer, J. E.; Dai, H.; Thess, A.; Lee, R.; Hanjani, N. M.; Dehaas, D. L.; Smalley, R. E. Metallic Resistivity in Crystalline Ropes of Single-Wall Carbon Nanotubes. *Phys. Rev. B - Condens. Matter Mater. Phys.* **1997**, *55* (8), 4921-R4924.

(5) Golberg, D.; Bando, Y.; Huang, Y.; Terao, T.; Mitome, M.; Tang, C. C.; Zhi, C. Y. Boron Nitride Nanotubes and Nanosheets. *ACS Nano.* **2010**, *4*(6), 2979-2993.

(6) Oberlin, A.; Endo, M.; Koyama, T. Filamentous Growth of Carbon through Benzene Decomposition. *J. Cryst. Growth* **1976**, *32* (3), 335-349.

(7) Iijima, S. Helical Microtubules of Graphitic Carbon. *Nature* **1991**, *354*, 56-58.

(8) Kudin, K. N.; Scuseria, G. E.; Yakobson, B. I. C_2F, BN, and C Nanoshell Elasticity from *Ab Initio* Computations. *Phys. Rev. B - Condens. Matter Mater. Phys.* **2001**, *64* (23), 235406-1-10.

(9) Wei, X. L.; Wang, M. S.; Bando, Y.; Golberg, D. Tensile Tests on Individual Multi-Walled Boron Nitride Nanotubes. *Adv. Mater.* **2010**, *22* (43), 4895-4899.

(10) Fereidoon, A.; Mostafaei, M.; Ganji, M. D.; Memarian, F. Atomistic Simulations on the Influence of Diameter, Number of Walls , Interlayer Distance and Temperature on the Mechanical Properties of BNNTs. *Superlattices Microstruct.* **2015**, *86*, 126-133.

(11) Demczyk, B. G.; Wang, Y. M.; Cumings, J.; Hetman, M.; Han, W.; Zettl, A.; Ritchie, R. O. Direct Mechanical Measurement of the Tensile Strength and Elastic Modulus of Multiwalled Carbon Nanotubes. *Mater. Sci. Eng. A* **2002**, *334*, 173-178.

(12) Li, C. Y.; Chou, T. W. Elastic Moduli of Multi-Walled Carbon Nanotubes and the Effect of Van Der Waals Forces. *Compos. Sci. Technol.* **2003**, *63* (11), 1517-1524.

(13) Belkerk, B. E.; Achour, A.; Zhang, D. Y.; Sahli, S.; Djouadi, M.; Yap, Y. K. Thermal Conductivity of Vertically Aligned Boron Nitride Nanotubes. *Appl. Phys. Express* **2016**, *9*, 16-20.

(14) Fujii, M.; Zhang, X.; Xie, H. Q.; Ago, H.; Takahashi, K.; Ikuta, T.; Abe, H.; Shimizu, T. Measuring the Thermal Conductivity of a Single Carbon Nanotube. *Phys. Rev. Lett.* **2005**, *95* (6), 8-11.

(15) Berber, S.; Kwon, Y. K.; Tomanek, D. Unusually High Thermal Conductivity of Carbon Nanotubes. *Phys. Rev. Lett.* **2000**, *84* (20), 4613-4616.

(16) Jo, I.; Pettes, M. T.; Kim, J.; Watanabe, K.; Taniguchi, T.; Yao, Z.; Shi, L. Thermal Conductivity and Phonon Transport in Suspended Few-Layer Hexagonal Boron Nitride. *Nano Lett.* **2013**, *13*, 550-554.

(17) Trivedi, S.; Sharma, S. C.; Harsha, S. P. Evaluations of Young 's Modulus of Boron Nitride Nanotube Reinforced Nano-Composites. *Procedia Mater. Sci.* **2014**, *6*, 1899-1905.

(18) Tao, J. X.; Xu, G. M.; Sun, Y. Z. Elastic Properties of Boron-Nitride Nanotubes through an Atomic Simulation Method. *Math. Probl. Eng.* **2015**, *2015*, 1-5.

(19) Chang, C. W.; Fennimore, A. M.; Afanasiev, A.; Okawa, D.; Ikuno, T.; Garcia, H.; Li, D.; Majumdar, A.; Zettl, A. Isotope Effect on the Thermal Conductivity of Boron Nitride Nanotubes. *Phys. Rev. Lett.* **2006**, *97* (8), 085901-1-4.

(20) Shin, H.; Guan, J. W.; Zgierski, M. Z.; Kim, K. S.; Kingston, C. T.; Simard, B. Covalent Functionalization of Boron Nitride Nanotubes *via* Reduction Chemistry. *ACS Nano* **2015**, *9* (12), 12573-12582.

(21) Zhi, C. Y.; Bando, Y.; Tang, C. C.; Golberg, D. Engineering of Electronic Structure of Boron-Nitride Nanotubes by Covalent Functionalization. *Phys. Rev. B - Condens. Matter Mater. Phys.* **2006**, *74* (15), 153413-1-4.

(22) Li, X. L.; Wu, X. J.; Zeng, X. C.; Yang, J. L. Band-Gap Engineering *via* Tailored Line Defects in Boron-Nitride Nanoribbons, Sheets, and Nanotubes. *ACS Nano* **2012**, *6* (5), 4104-4112.

(23) Lu, X.; Chen, Z. F. Curved Pi-Conjugation, Aromaticity, and the Related Chemistry of Small Fullerenes ($< C_{60}$) and Single-Walled Carbon Nanotubes. *Chem. Rev.* **2005**, *105* (10), 3643-3696.

(24) Laird. E. A.; Kuemmeth, F.; Steele, G. A.; Grove-Rasmussen, K.; Nygard, J.; Flensberg, K.; Kouwenhoven, L. P. Quantum Transport in Carbon Nanotubes. *Rev. Mod. Phys.* **2015**, *87*, 703-764.

(25) Wildöer, J. W. G.; Venema, L. C.; Rinzler, A. G.; Smalley, R. E.; Dekker, C. Electronic Structure of Atomically Resolved Carbon Nanotubes. *Nature* **1998**, *391*, 59-62.

(26) Arenal, R.; Blase, X.; Loiseau, A. Boron-Nitride and Boron-Carbonitride Nanotubes: Synthesis, Characterization and Theory. *Adv. Phys.* **2010**, *59* (2), 101-179.

(27) Chen, Y.; Zou, J.; Campbell, S. T.; Caer, G. L. Boron Nitride Nanotubes : Pronounced Resistance to Oxidation. *Appl. Phys. Lett.* **2004**, *84 (13)*, 2430-2432.

(28) Liu, Z.; Gong, Y. J.; Zhou, W.; Ma, L. L.; Yu, J. J.; Idrobo, J. C.; Jung, J.; Macdonald, A. H.; Vajtai, R.; Lou, J.; Ajayan, P. M. Ultrathin Higherature Oxidation-Resistant Coatings of Hexagonal Boron Nitride.

Nat. Commun. **2013**, *4*, 1-8.

(29) Lavrenko, V. A.; Alexeev, A. F. High-Temperature Oxidation of Boron Nitride. *Ceram. Int.* **1986**, *12* (1), 25-31.

(30) Estevez, J. E.; Ghazizadeh, M.; Ryan, J. G.; Kelkar, A. D. Simulation of Hydrogenated Boron Nitride Nanotubes Mechanical Properties for Radiation Shielding Applications. *Int. J. Mater. Metall. Eng.* **2014**, *8* (1), 63-67.

(31) Li, J.; Dahal, R.; Majety, S.; Lin, J. Y.; Jiang, H. X. Hexagonal Boron Nitride Epitaxial Layers as Neutron Detector Materials. *Nucl. Instruments Methods Phys. Res. A* **2011**, *654* (1), 417-420.

(32) Qi, J. S.; Qian, X. F.; Qi, L.; Feng, J.; Shi, D. N.; Li, J. Strain-Engineering of Band Gaps in Piezoelectric Boron Nitride Nanoribbons. *Nano Lett.* **2012**, *12* (3), 1224-1228.

(33) Michel, K. H.; Verberck, B. Theory of Elastic and Piezoelectric Effects in Two-Dimensional Hexagonal Boron Nitride. *Phys. Rev. B - Condens. Matter Mater. Phys.* **2009**, *80* (22), 224301-1-10.

(34) Nakhmanson, S. M.; Calzolari, A.; Meunier, V.; Bernholc, J.; Nardelli, M. B. Spontaneous Polarization and Piezoelectricity in Boron Nitride Nanotubes. *Phys. Rev. B - Condens. Matter Mater. Phys.* **2003**, *67* (23), 235406-1-5.

(35) Rafiee, M. A.; Narayanan, T. N.; Hashim, D. P.; Sakhavand, N.; Shahsavari, R.; Vajtai, R.; Ajayan, P. M. Hexagonal Boron Nitride and Graphite Oxide Reinforced Multifunctional Porous Cement Composites. *Adv. Funct. Mater.* **2013**, *23* (45), 5624-5630.

(36) Choi, S. R.; Bansal, N. P.; Garg, A. Mechanical and Microstructural Characterization of Boron Nitride Nanotubes-Reinforced SOFC Seal Glass Composite. *Mater. Sci. Eng. A* **2007**, *460-461*, 509-515.

(37) Wang, W. L.; Bi, J. Q.; Wang, S. R.; Sun, K. N.; Du, M.; Long, N. N.; Bai, Y. J. Microstructure and Mechanical Properties of Alumina Ceramics Reinforced by Boron Nitride Nanotubes. *J. Eur. Ceram. Soc.* **2011**, *31* (13), 2277-2284.

(38) Jang, S. K.; Youn, J.; Song, Y. J.; Lee, S. Synthesis and Characterization of Hexagonal Boron Nitride as a Gate Dielectric. *Sci. Rep.* **2016**, *6*, 1-9.

(39) Dean, C. R.; Young, A. F.; Meric, I.; Lee, C.; Wang, L.; Sorgenfrei, S.; Watanabe, K.; Taniguchi, T.; Kim, P.; Shepard, K. L.; Hone, J.. Boron Nitride Substrates for High-Quality Graphene Electronics. *Nat. Nanotechnol.* **2010**, *5* (10), 722-726.

(40) Chopra, N. G.; Luyken, R. J.; Cherrey, K.; Crespi, V. H.; Cohen, M. L.; Louie, S. G.; Zettl, A. Boron Nitride Nanotubes. *Science* **1995**, *269*, 966-968.

(41) McLean, B.; Eveleens, C. A.; Mitchell, I.; Webber, G. B.; Page, A. J. Catalytic CVD Synthesis of Boron Nitride and Carbon Nanomaterials-Synergies between Experiment and Theory. *Phys. Chem. Chem. Phys.* **2017**, *19* (39), 26466-26494.

(42) Pakdel, A.; Zhi, C. Y.; Bando, Y.; Nakayama, T.; Golberg, D. A Comprehensive Analysis of the CVD Growth of Boron Nitride Nanotubes. *Nanotechnology* **2012**, *23* (21), 215601-1-10.

(43) Chen, Y.; Gerald, J. F.; Williams, J. S.; Bulcock, S. Synthesis of Boron Nitride Nanotubes at Low Temperatures Using Reactive Ball Milling. *Chem. Phys. Lett.* **2006**, *299*, 260-264.

(44) Chen, Y.; Chadderton, L. T.; Gerald, J. F.; Williams, J. S. A Solid-State Process for Formation of Boron Nitride Nanotubes. *Appl. Phys. Lett.* **1999**, *74* (20), 2960-2962.

(45) Fathalizadeh, A.; Pham, T.; Mickelson, W.; Zettl, A. Scaled Synthesis of Boron Nitride Nanotubes, Nanoribbons, and Nanococoons Using Direct Feedstock Injection into an Extended-Pressure, Inductively-Coupled Thermal Plasma. *Nano Lett.* **2014**, *14* (8), 4881-4886.

(46) Lee, C. M.; Choi, S. I.; Choi, S. S.; Hong, S. H. Synthesis of Boron Nitride Nanotubes by Arc-Jet Plasma. *Curr. Appl. Phys.* **2006**, *6* (2), 166–170.

(47) Narita, I.; Oku, T. Synthesis of Boron Nitride Nanotubes by Using YB_6 Powder. *Solid State Commun.* **2002**, *122*, 465-468.

(48) Cumings, J.; Zettl, A. Mass-Production of Boron Nitride Double-Wall Nanotubes and Nanococoons. *Chem. Phys. Lett.* **2000**, 316, 211-216.

(49) Yeh, Y. W.; Raitses, Y.; Koel, B. E.; Yao, N. Stable Synthesis of Few-Layered Boron Nitride Nanotubes by Anodic Arc Discharge. *Sci. Rep.* **2017**, *7*, 1-7.

(50) Chen, Y.; Conway, M.; Williams, J. S.; Zou, J. Large-Quantity Production of High-Yield Boron Nitride Nanotubes. *J. Mater. Res.,* **2006**, *17* (8), 1896-1899.

(51) Chen, H.; Chen, Y.; Liu, Y.; Fu, L.; Huang, C.; Llewellyn, D. Over 1.0 mm-Long Boron Nitride Nanotubes. *Chem. Phys. Lett.* **2008**, *463*, 130-133.

(52) Tang, C. C.; Bando, Y.; Sato, T.; Kurashima, K. A Novel Precursor for Synthesis of Pure Boron Nitride Nanotubes. *Chem. Commun.*. **2002**, *2* (12), 1290-1291.

(53) Lee, C. H.; Xie, M.; Kayastha, V.; Wang, J. S.; Yap, Y. K. Patterned Growth of Boron Nitride Nanotubes by Catalytic Chemical Vapor Deposition. *Chem. Mater.* **2010**, *22* (5), 1782-1787.

(54) Shimizu, Y.; Moriyoshi, Y.; Tanaka, H.; Komatsu, S. Boron Nitride Nanotubes, Webs, and Coexisting Amorphous Phase Formed by the Plasma Jet Method. *Appl. Phys. Lett.* **1999**, *75* (7), 929-931.

(55) Hales, S. J.; Alexa, J. A.; Jensen, B. J.; Thomsen, D. L. Radio Frequency Plasma Synthesis of Boron Nitride Nanotubes (BNNTs) for Structural Applications: Part I. **2016**.

(56) Bhuiyan, M. M. H.; Wang, J. T.; Li, L. H.; Hodgson, P.; Agarwal, A.; Qian, M.; Chen, Y. Boron Nitride Nanotube Reinforced Titanium Metal Matrix Composites with Excellent High-Temperature Performance. *J. Mater. Res.* **2017**, *32* (19), 3744-3752.

(57) Blase, X.; Rubio, A.; Louie, S. G.; Cohen, M. L. Stability and Band-Gap Constancy of Boron-Nitride Nanotubes. *Europhys. Lett.* **1994**, *28*, 335–340.

(58) Chen, C. W.; Lee, M. H.; Clark, S. J. Band Gap Modification of Single-Walled Carbon Nanotube and Boron Nitride Nanotube under a Transverse Electric Field. *Nanotechnology* **2004**, *15* (12), 1837-1843.

(59) Mele, E. J.; Král, P. Electric Polarization of Heteropolar Nanotubes as a Geometric Phase. *Phys. Rev. Lett.* **2002**, *88* (5), 056803-1-4.

(60) Král, P.; Mele, E. J.; Tománek, D. Photogalvanic Effects in Heteropolar Nanotubes. *Phys. Rev. Lett.* **2000**, *85* (7), 1512-1515.

(61) Yun, K. N.; Lee, S. H.; Han, J. S.; Song, Y. H.; Lee, C. J. Field Emission Behavior of Boron Nitride Nanotubes. *Nanotechnology* **2018**, *29* (8), 085203-1-5.

(62) Yu, M. F.; Lourie, O.; Dyer, M. J.; Moloni, K.; Kelly, T. F.; Ruoff, R. S. Strength and Breaking Mechanism of Multiwalled Carbon Nanotubes Under Tensile Load. *Science* **2000**, *287*, 637-641.

(63) Yu, M. F.; Files, B. S.; Arepalli, S.; Ruoff, R. S. Tensile Loading of Ropes of Single Wall Carbon Nanotubes and Their Mechanical Properties. *Phys. Rev. Lett.* **2000**, *84* (24), 5552-5555.

(64) Hsin, C. L.; Mai, W.; Gu, Y.; Gao, Y.; Huang, C. Te; Liu, Y.; Chen, L. J.; Wang, Z. L. Elastic Properties and Buckling of Silicon Nanowires. *Adv. Mater.* **2008**, *20* (20), 3919-3923.

(65) Tao, X. Y.; Li, X. D. Catalyst-Free Synthesis, Structural, and Mechanical Characterization of Twinned $Mg_2B_2O_5$ Nanowires. *Nano Lett.* **2008**, *8* (2), 505-510.

(66) Xu, F.; Qin, Q. Q.; Mishra, A.; Gu, Y.; Zhu, Y. Mechanical Properties of ZnO Nanowires under Different Loading Modes. *Nano Res.* **2010**, *3* (4), 271-280.

(67) Zhang, D. F.; Breguet, J. M.; Clavel, R.; Phillippe, L.; Utke, I.; Michler, J. *In Situ* Tensile Testing of Individual Co Nanowires inside a Scanning Electron Microscope. *Nanotechnology* **2009**, *20* (36), 365706-1-7.

(68) Zeng, H. J.; Li, T.; Bartenwerfer, M.; Fatikow, S.; Wang, Y. L. *In Situ* SEM Electromechanical Characterization of Nanowire Using an Electrostatic Tensile Device. *J. Phys. D. Appl. Phys.* **2013**, *46* (30), 305501-1-8.

(69) Zhu, Y. F.; Han, X. D. Zheng, K.; Zhang, X. N.; Fu, J. Y.; Ji. Y.; Hao, Y. J.; Guo, X. Y.; Wang, Z. L. Direct Observation of Super-Plasticity of Beta-SiC Nanowires at Low Temperature. *Adv. Funct. Mater.* **2007**, *17* (17), 3435-3440.

(70) Zhu, Y.; Qin, Q. Q.; Xu, F.; Fan, F. R.; Ding, Y.; Zhang, T.; Wiley, B. J.; Wang, Z. L. Size Effects on Elasticity, Yielding, and Fracture of Silver Nanowires: *In Situ* Experiments. *Phys. Rev. B - Condens. Matter Mater. Phys.* **2012**, *85* (4), 045443-1-7.

(71) Wu, B.; Heidelberg, A.; Boland, J. J. Mechanical Properties of Ultrahigh-Strength Gold Nanowires.

Nat. Mater. **2005**, *4* (7), 525-529.

(72) Salvetat, J. P.; Kulik, A. J.; Bonard, J. M.; Briggs, G. A. D.; Stöckli, T.; Méténier, K.; Bonnamy, S.; Béguin, F.; Burnham, N. A.; Forró, L. Elastic Modulus of Ordered and Disordered Multiwalled Carbon Nanotubes. *Adv. Mater.* **1999**, *11* (2), 161-165.

(73) Chen, Y.; Stevenson, I.; Pouy, R.; Wang, L.; McIlroy, D. N.; Pounds, T.; Grant Norton, M.; Eric Aston, D. Mechanical Elasticity of Vapour-Liquid-Solid Grown GaN Nanowires. *Nanotechnology* **2007**, *18* (13), 135708-1-8.

(74) Kim, Y. J.; Son, K.; Choi, I. C.; Choi, I. S.; Park, W. II; Jang, J. I. Exploring Nanomechanical Behavior of Silicon Nanowires: AFM Bending Versus Nanoindentation. *Adv. Funct. Mater.* **2011**, *21* (2), 279-286.

(75) Sohn, Y. S.; Park, J.; Yoon, G.; Song, J.; Jee, S. W.; Lee, J. H.; Na, S.; Kwon, T.; Eom, K. Mechanical Properties of Silicon Nanowires. *Nanoscale Res. Lett.* **2010**, *5* (1), 211-216.

(76) Song, J. H.; Wang, X. D.; Riedo, E.; Wang, Z. L. Elastic Property of Vertically Aligned Nanowires. *Nano Lett.* **2005**, *5* (10), 1954-1958.

(77) Espinosa, H. D.; Bernal, R. A.; Filleter, T. *In-Situ* TEM Electromechanical Testing of Nanowires and Nanotubes. *Small* **2012**, *8* (21), 191-226.

(78) Hoffmann, S.; Östlund, F.; Michler, J.; Fan, H. J.; Zacharias, M.; Christiansen, S. H.; Ballif, C. Fracture Strength and Young's Modulus of ZnO Nanowires. *Nanotechnology* **2007**, *18* (20), 205503-1-5.

(79) Wen, B. M.; Sader, J. E.; Boland, J. J. Mechanical Properties of ZnO Nanowires. *Phys. Rev. Lett.* **2008**, *101* (17), 175502-1-4.

(80) Ngo, L. T.; Almécija, D.; Sader, J. E.; Daly, B.; Petkov, N.; Holmes, J. D.; Erts, D.; Boland, J. J. Ultimate-Strength Germanium Nanowires. *Nano Lett.* **2006**, *6* (12), 2964-2968.

(81) Zhang, H. T.; Tersoff, J.; Xu, S.; Chen, H. X.; Zhang, Q. B.; Zhang, K. L.; Yang, Y.; Lee, C. S.; Tu, K. N.; Li, J.; Lu, Y. Approaching the Ideal Elastic Strain Limit in Silicon Nanowires. *Sci Adv.* **2016**, *2*, 2-10.

(82) Peng, B.; Locascio, M.; Zapol, P.; Li, S.; Mielke, S. L.; Schatz, G. C.; Espinosa, H. D. Measurements of Near-Ultimate Strength for Multiwalled Carbon Nanotubes and Irradiation-Induced Crosslinking Improvements. *Nat. Nanotechnol.* **2008**, *3* (10), 626-631.

(83) Espinosa, H. D.; Zhu, Y.; Moldovan, N. Design and Operation of a MEMS-Based Material Testing System for Nanomechanical Characterization. *J. Microelectromech. Syst.* **2007**, *16* (5), 1219-1231.

(84) Yang, Y.; Cui, Y.; Fu, Z. Q.; Li, T.; Xu, F.; Wang, Y. L. Size-Dependent Mechanical Behavior of a-Silicon Carbide Nanowires under *In-Situ* Transmission Electron Microscopy. *Mater. Res. Express* **2019**, *6*, 045009-1-9.

(85) Tang, D. M.; Ren, C. L.; Wang, M. S.; Wei, X. L.; Kawamoto, N.; Liu, C.; Bando, Y.; Mitome, M.; Fukata, N.; Golberg, D. Mechanical Properties of Si Nanowires as Revealed by *In Situ* Transmission Electron Microscopy and Molecular Dynamics Simulations. *Nano Lett.* **2012**, *12*, 1898-1904.

(86) Treacy, M. M. J.; Ebbesen, T. W.; Gibson, J. M. Exceptionally High Young's Modulus Observed for Individual Carbon Nanotubes. *Nature* **1996**, *381* (20) 678-680.

(87) Feng, X. L.; He, R. R.; Yang, P. D.; Roukes, M. L. Very High Frequency Silicon Nanowire Electromechanical Resonators. *Nano Lett.***2007**, *7* (7), 1953-1959.

(88) Shi, Y.; Chen, C. Q.; Zhang, Y. S.; Zhu, J.; Yan, Y. J. Determination of the Natural Frequency of a Cantilevered ZnO Nanowire Resonantly Excited by a Sinusoidal Electric Field. *Nanotechnology* **2007**. *18*, 075709-1-6.

(89) Li, P. F.; Liao, Q. L.; Yang, S. Z.; Bai, X. D.; Huang, Y. H.; Yan, X. Q.; Zhang, Z.; Liu, S.; Lin, P.; Kang, Z.; Zhang, Y. *In Situ* Transmission Electron Microscopy Investigation on Fatigue Behavior of Single ZnO Wires under High-Cycle Strain. *Nano Lett.* **2014**, *14*, 480-485.

(90) Biedermann, L. B.; Tung, R. C.; Raman, A.; Reifenberger, R. G.; Yazdanpanah, M. M.; Cohn, R. W. Characterization of Silver-Gallium Nanowires for Force and Mass Sensing Applications. *Nanotechnology* **2010**. *21*, 305701-1-10.

(91) Qin, Q. Q.; Xu, F.; Cao, Y. Q.; Ro, P. I.; Zhu, Y. Measuring True Young's Modulus of a Cantilevered Nanowire : Effect of Clamping on Resonance Frequency. *Small* **2012**, *8* (16), 2571-2576.

(92) Yang, Y. T.; Callegari, C.; Feng, X. L.; Ekinci, K. L.; Roukes, M. L. Zeptogram-Scale Nanomechanical Mass Sensing. *Nano Lett.* **2006**, *6* (4), 583-586.

(93) Yu, M. F.; Wagner, G. J.; Ruoff, R. S.; Dyer, M. J. Realization of Parametric Resonances in a Nanowire Mechanical System with Nanomanipulation inside a Scanning Electron Microscope. *Phys. Rev. B* **2002**, *66*, 073406-1-4.

(94) Gao, P.; Liu, K. H.; Liu, L.; Wang, Z. Z.; Liao, Z. L.; Xu, Z.; Wang, W. L.; Bai, X. D.; Wang, E. G.; Li, Y. Q. Higher-Order Harmonic Resonances and Mechanical Properties of Individual Cadmium Sulphide Nanowires Measured by *in Situ* Transmission Electron Microscopy. *J. Electron Microsc.* **2010**, *59* (4), 285-289.

(95) Wang, Z. L.; Dai, Z. R.; Gao, R. P.; Gole, J. L. Measuring the Young's Modulus of Solid Nanowires by *In Situ* TEM. *J. Electron Microsc.* **2002**, *51*, 79 - 85.

(96) Wang, M. S.; Kaplan-Ashiri, I.; Wei, X. L.; Rosentsveig, R.; Wagner, H. D.; Tenne, R.; Peng, L. M. *In Situ* TEM Measurements of the Mechanical Properties and Behavior of WS_2 Nanotubes. *Nano Res.* **2008**, *1* (1), 22-31.

(97) Verma, V.; Jindal, V. K.; Dharamvir, K. Elastic Moduli of a Boron Nitride Nanotube. *Nanotechnology*

2007. *18*, 435711-1-6.

(98) Oh, E. Elastic Properties of Various Boron-Nitride Structures. *Met. Mater. Int.* **2011**, *17* (1), 21-27.

(99) Peng, Y. J.; Zhang, L. Y.; Jin, Q. H.; Li, B. H.; Ding, D. T. Ab Initio Studies of Elastic Properties and Electronic Structures of C and BN Nanotubes. *Physica E* **2006**, *33*, 155-159.

(100) Griebel, M.; Hamaekers, J.; Heber, F. A Molecular Dynamics Study on the Impact of Defects and Functionalization on the Young Modulus of Boron - Nitride Nanotubes. *Comput. Mater. Sci.* **2009**, *45* (4), 1097-1103.

(101) Chopra, N. G.; Zettl, A. Measurement of The Elastic Modulus of A Multi-walled Boron Nitride Nanotubes. *Solid State Commun.* **1998**, *105 (5)*, 297–300.

(102) Suryavanshi, A. P.; Yu, M. F.; Wen, J.; Tang, C. C.; Bando, Y. Elastic Modulus and Resonance Behavior of Boron Nitride Nanotubes. *Appl. Phys. Lett.* **2004**, *84 (14)*, 2527–2529.

(103) Alem, N.; Erni, R.; Kisielowski, C.; Rossell, M. D.; Gannett, W.; Zettl, A. Atomically Thin Hexagonal Boron Nitride Probed by Ultrahigh-Resolution Transmission Electron Microscopy. *Phys. Rev. B* **2009**, *80*, 155425-1-7.

(104) Celik-Aktas, A.; Stubbins, J. F.; Zuo, J. M. Electron Beam Machining of Nanometer-Sized Tips from Multiwalled Boron Nitride Nanotubes. *J. Appl. Phys.* **2007**, *102* (2), 024310-1-6.

(105) Zobelli, A.; Ewels, C. P.; Gloter, A.; Seifert, G.; Stephan, O.; Csillag, S.; Colliex, C. Defective Structure of BN Nanotubes: From Single Vacancies to Dislocation Lines. *Nano Lett.* **2006**, *6* (9), 1955-1960.

(106) Cheng, G.; Yao, S.; Sang, X.; Hao, B.; Zhang, D.; Yap, Y. K.; Zhu, Y. Evolution of Irradiation-Induced Vacancy Defects in Boron Nitride Nanotubes. *Small* **2016**, *12* (6), 818-824.

(107) Cretu, O.; Lin, Y. C.; Suenaga, K. Inelastic Electron Irradiation Damage in Hexagonal Boron Nitride. *Micron* **2015**, *72*, 21-27.

(108) Zhou, X.; Hsia, F. C.; Xue, Y.; Tang, D. M.; Cretu, O.; Zhang, C.; Mitome, M.; Bando, Y.; Sasaki, T.; Golberg, D. Tunable Mechanical and Electrical Properties of Coaxial BN-C Nanotubes. *Phys. Status Solidi - Rapid Res. Lett.* **2019**, *13* (3), 1-7.

(109) Xiang, R.; Inoue, T.; Zheng, Y.; Kumamoto, A,; Qian, Y.; Sato Y, Liu, M.; Gokhale, D.; Guo, J.; Hisama, K.; Yotsumoto, S.; Ogamoto, T.; Arai, H.; Kobayashi, Y.; Zhang, H.;, Hou, B.; Anisimov, A.; Miyata, Y.; Okada, S.; Chiashi, S.; Li, Y.; Kong, J.; Kauppinen, E.; Ikuhara, Y., Suenaga, K.; Maruyama, S. One-Dimensional van Der Waals Heterostructures. arXiv:1807.06154.

Chapter 2

Intrinsic elastic moduli of BNNTs precisely measured inside a transmission electron microscope

2.1 Introduction

Boron nitride nanotubes (BNNTs), represent an important member of the one-dimensional nanomaterial family and gained a lot of attention from the scientific community. Structurally, it has been regarded as the inorganic analogue of carbon nanotubes (CNTs) but composed of boron and nitrogen atoms by substituting carbon atoms in a hexagonal lattice network.[1–4] Comparing with CNTs, BNNTs are the light substance with white appearance, possess quite similar elastic property to CNTs,[5–7] but superior chemical and thermal stability than CNTs, which make BNNTs important for mechanical applications in extreme environments.[8–10] Regarding these practical applications, precise evaluation of the intrinsic elastic properties will be crucial. However, up to now, their intrinsic elastic properties have not been precisely evaluated, and importantly, the properties-structures relations have not been established. While theoretical calculations have shown that the elastic modulus of BNNTs is around 1 TPa,[11–13] precise experimental measurements are largely lacking. For instance, Wei *et al.* reported *in situ* TEM tensile tests of individual BNNTs,[14] which showed the elastic moduli in a range of 725-1343 GPa with a standard deviation of 26.9 %. Thermal and electric field-induced vibrations at 1st order resonance on individual cantilevered BNNTs have been reported by Chopra *et al.* and Suryavanshi *et al*.. These works showed wide ranges of measured moduli from 980 GPa to 1460 GPa, and from 505 GPa to 1030 GPa, at standard deviations of 19.8 % and 20.6 %, respectively. Thus, at a current stage, it is important to more precisely elucidate the intrinsic elastic properties of BNNTs and to understand the origin of the deviation of the measured elastic moduli.

Herein, in this Chapter, intrinsic elastic properties of multiwalled BNNTs have been precisely measured using a high-order resonance technique in a high-resolution transmission electron microscope (HRTEM). Resonances up to 4th order for normal modes and 3rd order for parametric modes have been initiated in the cantilevered tubes, and the recorded frequencies were found to be well consistent with the theoretical calculations with a discrepancy of only ~ 1 %. The elastic moduli of the BNNTs measured from high-order

resonance were about 906 GPa on average, with a standard deviation of 9.3 %, which was found to be closely related to the intrinsic defect as cavities in the nanotube walls.

2.2 Synthesis and characterization of BNNTs

2.2.1 Synthesis of BNNTs

Firstly, pure and high-quality BNNTs were prepared by the boron and metal oxide-assisted chemical vapor deposition method (BOCVD) in and induction furnace, which has been reported by our group before. In the synthesis process, boron and magnesium oxide powder as a precursor, and ammonia gas as a nitrogen source. The synthesis was proceeded in an induction furnace at 1300 ºC. After this process, the as-obtained BNNTs were further purified at a temperature of 1800 ºC to remove the possible residues, as schematically shown in **Figure 2.1**.

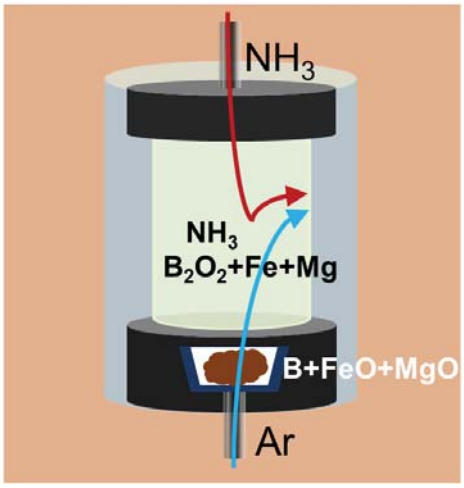

Figure 2.1 Schematic illustration of BN nanotubes' synthesis.

2.2.2 Characterization of BNNTs

The morphology of the as-obtained product was studied by using a field emission scanning electron microscope JEOL SM-67F, operated at an accelerating voltage of 10 kV. The SEM images in **Figure 2.2a** revealed that the BNNTs have diameters of around tens of nanometers, and lengths of up to several micrometers. X-ray diffraction (XRD) analysis of BNNTs was performed on a RINT2000 Ultima III diffractometer by using Cu-Kα radiation (λ=1.5403 Å) at room temperature and the results are shown in **Figure 2.2b**. All the recorded peaks can be assigned to an *h*-BN phase,[15–17] confirming that no other phases were introduced during high temperature synthesis process. Optical photographs (inset to the SEM image) showed the white color of the sample, common to BN materials. **Figure 2.2c** shows the Raman spectrum for BNNTs, which was measured at a 514.5 nm excitation wavelength using a Horiba-Jovin Yvon T64000 spectrometer. The peak at 1367 cm^{-1} is attributable to the E_{2g} vibration mode of the sp^2- bonded BNNTs with a layered graphitic structure.[18,19]

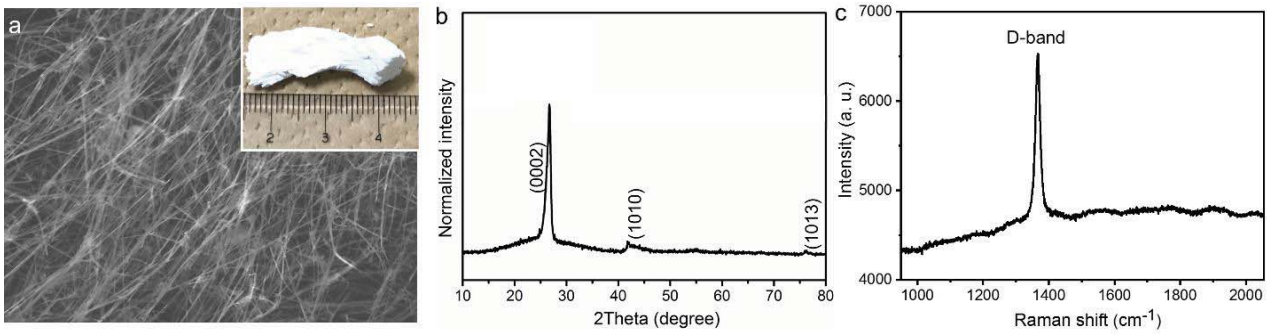

Figure 2.2 (a) SEM image of as-prepared BNNTs. Inset is a photograph of BN sample. (b) and (c) XRD pattern and Raman spectrum of BNNTs.

The structure and quality of the sample were further studied under TEM characterization. TEM image shown in **Figure 2.3a** clearly revealed the hollow tubular structure of the sample. HRTEM image (**Figure 2.3b**) confirms its good crystallinity of BNNTs. These show straight tube walls with an average spacing of 0.335 nm. The fringes close to the tube axis have a spacing of 0.219 nm, which are assigned to the (1010) planes of *h*-BN. **Figure 2.3c** presents the diameter distributions of BNNTs collected from 120 individual nanotubes, showing that the diameters od BNNTs mainly range from 30 nm to 100 nm, with an average value, ~57 nm.

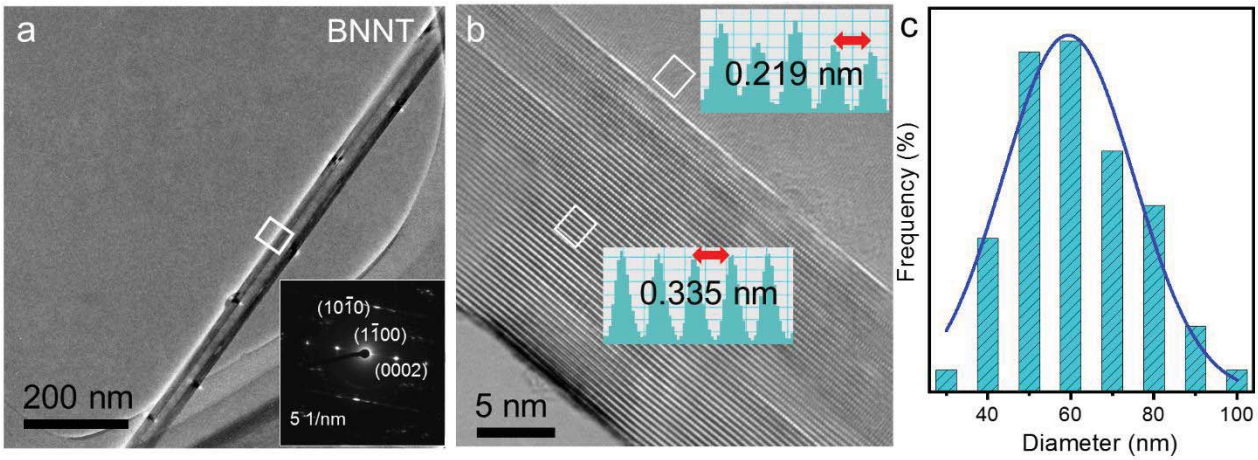

Figure 2.3 (a) Low-magnification TEM image, (b) High-resolution TEM image, (e) Outer diameter distribution diagram for BNNTs. The inset in (a) is SAED pattern taken from BNNT.

2.3 Methods

2.3.1 Experimental set-up

In situ experiments, as well as high-resolution imaging, were conducted inside an energy-filtering JEOL 3100FEF(Omega filter) TEM, operated at 300 kV. *In situ* electromechanical resonances on individual BNNTs were initiated using a scanning tunneling microscopy (STM)-TEM holder (Nanofactory Instruments AB). The experimental setup is shown in **Figure 2.4**. BNNTs were attached to a flat Au edge using silver epoxy. A freshly electrochemically etched Au probe was used as a counter electrode, which was moved by a piezo-motor in

three dimensions with a sub-nanometer precision. The Au probe was firstly moved to contact its free end and to ensure that the two are located at the same height, then the Au probe was moved backward ~40 nm. An alternating current (AC) signal was applied to excite the mechanical resonance. The AC sinusoidal signal was generated by a Tektronix Arbitrary Function Generator (AFG3152C) with a frequency range of 1 μHz-150 MHz. The maximum vibration amplitude was achieved *via* fine tuning of frequency to accurately determine the resonance frequency.

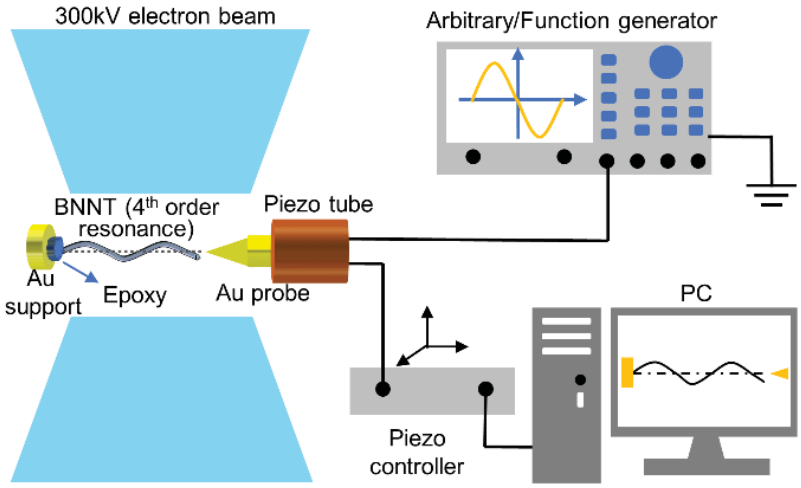

Figure 2.4 Schematic of the experimental setup of *in situ* TEM high-order resonance for measuring the elastic moduli. BNNTs were attached to an Au support by silver epoxy. An Au probe, used as a counter electrode, was controlled by a piezo-motor. An arbitrary/function generator provides a sinusoidal signal. By carefully tuning the signal frequency, up to 4th order normal and parametric resonances were excited.

2.3.2 Basics for electric field-induced resonance method

The electric-field-induced mechanical resonance of nanotubes was firstly proposed by Poncharal *et al.*. It is based on the electromechanical coupling between the nanotube and the applied electric field. In practical experiments, a constant voltage V_{dc} and an oscillating voltage $V_{ac}cos2\pi f_d t$ are applied across the BNNT, where V_{ac} is the amplitude and f_d is the driving frequency. The driving force acting on the BNNT is the product of the electrical field (denoted as αV, where α is related to the geometry and distance between BNNT and Au probe and V is the total potential between nanotube and Au probe) and induced charge on the tip of nanotube (denoted as βV, where β is a proportional constant):[20–22]

$$F(t) = (\alpha V)\cdot(\beta V) = \alpha\beta(\Delta V + V_{dc} + V_{ac}cos2\pi f_d t)^2$$

$$= \alpha\beta\left[\alpha\beta(\Delta V + V_{dc})^2 + 2(\Delta V + V_{dc})V_{ac}cos2\pi f_d t + \frac{1}{2}{V_{ac}}^2 + \frac{1}{2}{V_{ac}}^2 cos4\pi f_d t\right]$$

$$= F^{(0)} + F^{(1)}cos2\pi f_d t + F^{(2)}cos4\pi f_d t \quad (2.1)$$

where ΔV is the spontaneous electrical potential because of the difference in work function between BNNT and Au probe. According to the expression, it is supposed that the resonances will be initiated at two independent frequencies: f_d and $2f_d$. In addition to these two possible resonance frequencies, other research results even showed 3 or 4 resonance frequencies, which can be ascribed to the parametric resonance. And, it

has been proposed that for a single-degree-of-freedom mechanical system as we constructed inside TEM, parametric resonance can be described by the Mathieu equation:[23,24]

$$\frac{d^2Y}{dt^2} + \frac{dY}{dt} + (a + 2\varepsilon cos\omega t)Y = 0 \qquad (2.2)$$

where Y is an angular or displacement variable, a and ε are system parameters, $\mu$is the damping constant. In our case, it can be considered that the system undamped (μ=0) system on account of the ultrahigh vacuum inside TEM, and the theory predicts instabilities at a=n^2/4 (n is an integer, n≥1). Such instabilities cause parametric resonances of the system at driving frequencies of $f_{ni} = \frac{2}{n} f_i$, where f_i is the natural resonance frequencies of the system and n is defined as the number of parametric order (n=1, 2, 3,…). Obviously, with n=2 one can get the natural resonance.

According to the classic Euler-Bernoulli equation for a cantilevered beam and considering the hollow cylindrical cross-section of BNNT, the natural resonance frequency f_i can be expressed as:[25,26]

$$f_i = \frac{{\beta_i}^2 \sqrt{{D_o}^2 + {D_i}^2}}{8\pi L^2} \sqrt{\frac{E}{\rho}} \qquad (2.3)$$

Therefore, the elastic modulus E is given by:

$$E = \frac{64\pi^2 L^4}{{D_o}^2 + {D_i}^2} \left(\frac{f_i}{{\beta_i}^2} \right)^2 \qquad (2.4)$$

where D_o, D_i, ρ, L are the outer and inner diameter, mass density and length of the nanotubes, respectively. β_i is an eigenvalue, where β_1=1.875, β_2=4.694, β_3=7.855, β_4=10.996 and the integer subscripts i=1, 2, …. correspond to the 1st, 2nd, and higher eigenmodes.[27] Equation (2.4) clearly reveals that the elastic modulus is proportional to L^4, which makes the nanotube length calibration crucial to achieve the accurate value of the elastic modulus. The detailed discussion about the length calibration is discussed below.

2.3.3 Length calibration

A three-step process was carried out to insure an accurate length estimation of the studied BN-C NTs, as illustrated in **Figure 2.5**. This was necessary due to the fact that the TEM shows a projection of the structure along the direction of the electron beam (**Figure 2.5a**). Firstly, in-focus HRTEM images were taken from the free and clamped ends of the tube, allowing for the height difference between these points to be evaluated. Secondly, the spacing between BN walls and graphite layers is a constant value (0.335 nm), which was used to accurately measure the nanotube diameters using HRTEM images. In our case, it was found that the outer diameters estimated from HRTEM images (magnification: 150k to 300k) are always about 1.1 to 1.4 times larger than those estimated from low-magnification images (magnification: 5k to 10k). The final tube length was obtained by multiplying the length data calculated in the first step with this factor. Lastly, the node in the second mode harmonic resonance is located at 0.783 L from the anchor point according to classical beam mechanics. Thus, this number can be used to recheck the length of the resonating BNNTs. A comparison between the calibrated lengths and the lengths evaluated from the second mode can be found in **Figure 2.5b**.

The linear fitting with a slope of 1.033 and coefficient of determination (R^2) of 0.997 reveals good agreements between these two methods and implies that the BNNT lengths can precisely be determined.

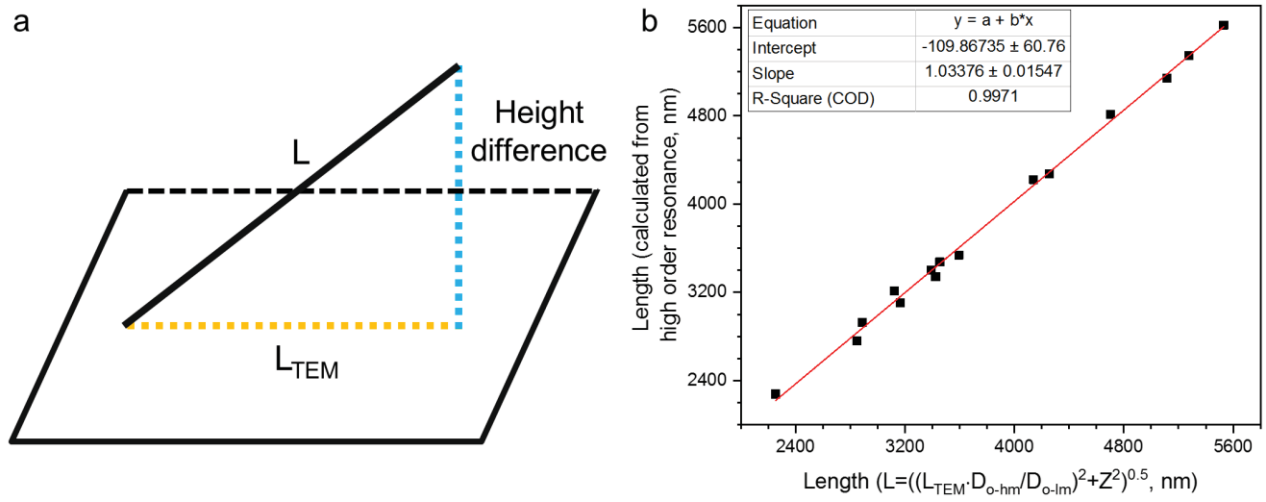

Figure 2.5 (a) Schematic drawing of the relation between the actual nanotube length (L) with the projected nanotube length (L_{TEM}) acquired under TEM imaging. (b) The relationship between nanotube lengths estimated from $L= (((D_{o\text{-}hm}/D_{o\text{-}lm})\cdot L_{TEM})^2+Z^2)^{1/2}$ and high order resonance.

2.4 Results

2.4.1 High-order resonances of individual BNNTs

Representative experimental results for a BNNT with natural resonance (n=2), up to 4th order, and parametric resonance (n=1), up to 3rd order, were recorded, as shown in **Figure 2.6**. **Figure 2.6a** depicts the natural resonances of a BNNT from 1st to 4th order at resonance frequencies of 3.425 MHz, 21.297 MHz, 60.104 MHz, and 122.018 MHz. According to Equation (2.4), the corresponding elastic moduli were calculated to be 922 GPa, 908 GPa, 922 GPa, and 989 GPa, at each resonance frequency. **Figure 2.6b** shows the 1st to 3rd parametric resonances of the same BNNT at frequencies twice of the corresponding natural resonance, as predicted by the Mathieu equation.[29] **Figure 2.6c** shows the relationship between resonance frequencies and mode orders. It can be seen that the resonance frequencies for natural resonance are following the β_i^2/β_j^2 relation with an average difference of 0.9 % (Equation (2.3), i and j denote different resonance orders), which are consistent with the E-B theory prediction. As for parametric resonance (n=1), the resonance frequencies are in good accordance with the $f_{ni} = \frac{2}{n} f_i$ relationship. Node positions for different orders are marked by blue circles in Figs 2a and 2b. Taking 4th order as an example, theoretically calculated nodes are at 0.358 L, 0.644 L and 0.906 L,[27] whereas experimental values are 0.368 L, 0.649 L, and 0.915 L, with an average difference of ~ 1.5 %. As also could be seen from additional results of BNNTs with high-order resonances (**Figure 2.7** and **Figure 2.8**), the precision of the measurement method is ~ 1 %, consistent with our previous reports.[28]

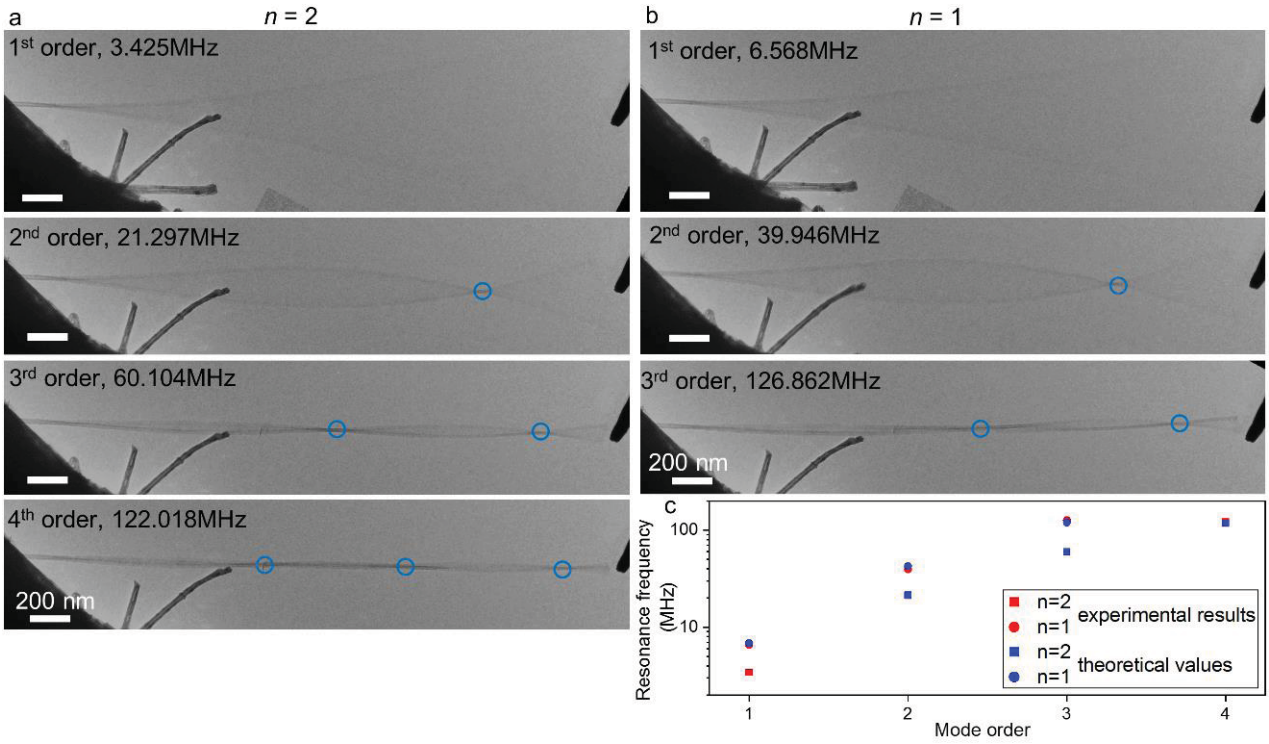

Figure 2.6 (a) and (b) TEM images showing a BNNT resonating at natural (*n*=2) and parametric (*n*=1) modes of from 1st to 4th and 1st to 3rd orders. Node positions are marked by blue circles. (c) The plot of experimentally recorded and theoretically predicted resonance frequencies for each resonance mode and order.

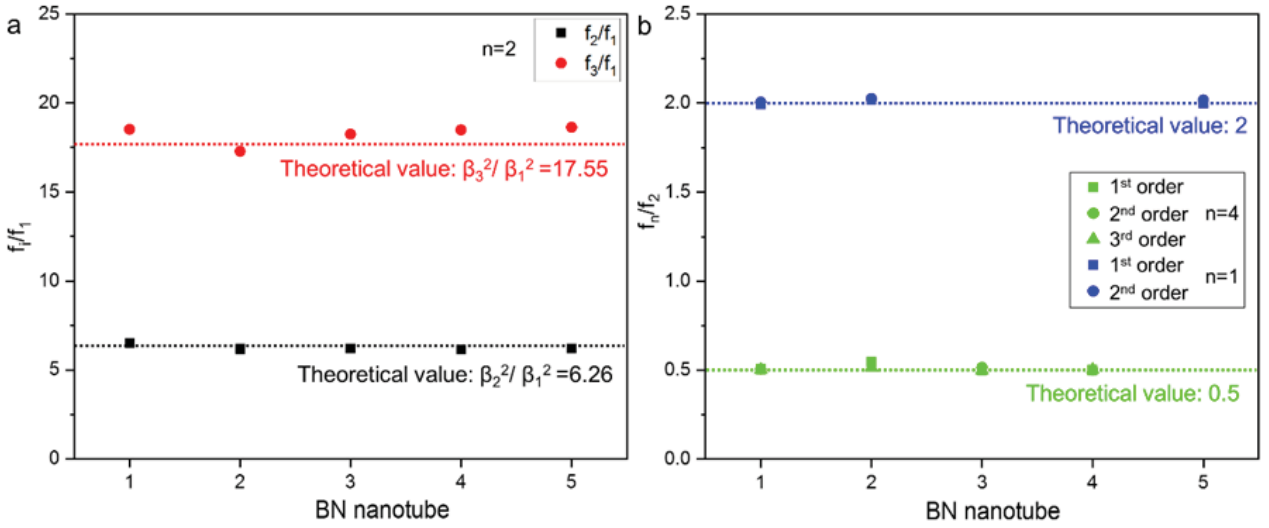

Figure 2.7 (a) Resonance frequencies ratio between high order and 1st order resonance for five BNNTs at the natural resonance mode (*n*=1, integer *i* denotes different resonance orders). (b) Resonance frequencies ratio between parametric (*n*=1 and n=*4*) and natural resonances (*n*=2) at different orders for five different BNNTs, *n* denotes different resonance modes. The dashed line represents the theoretical value.

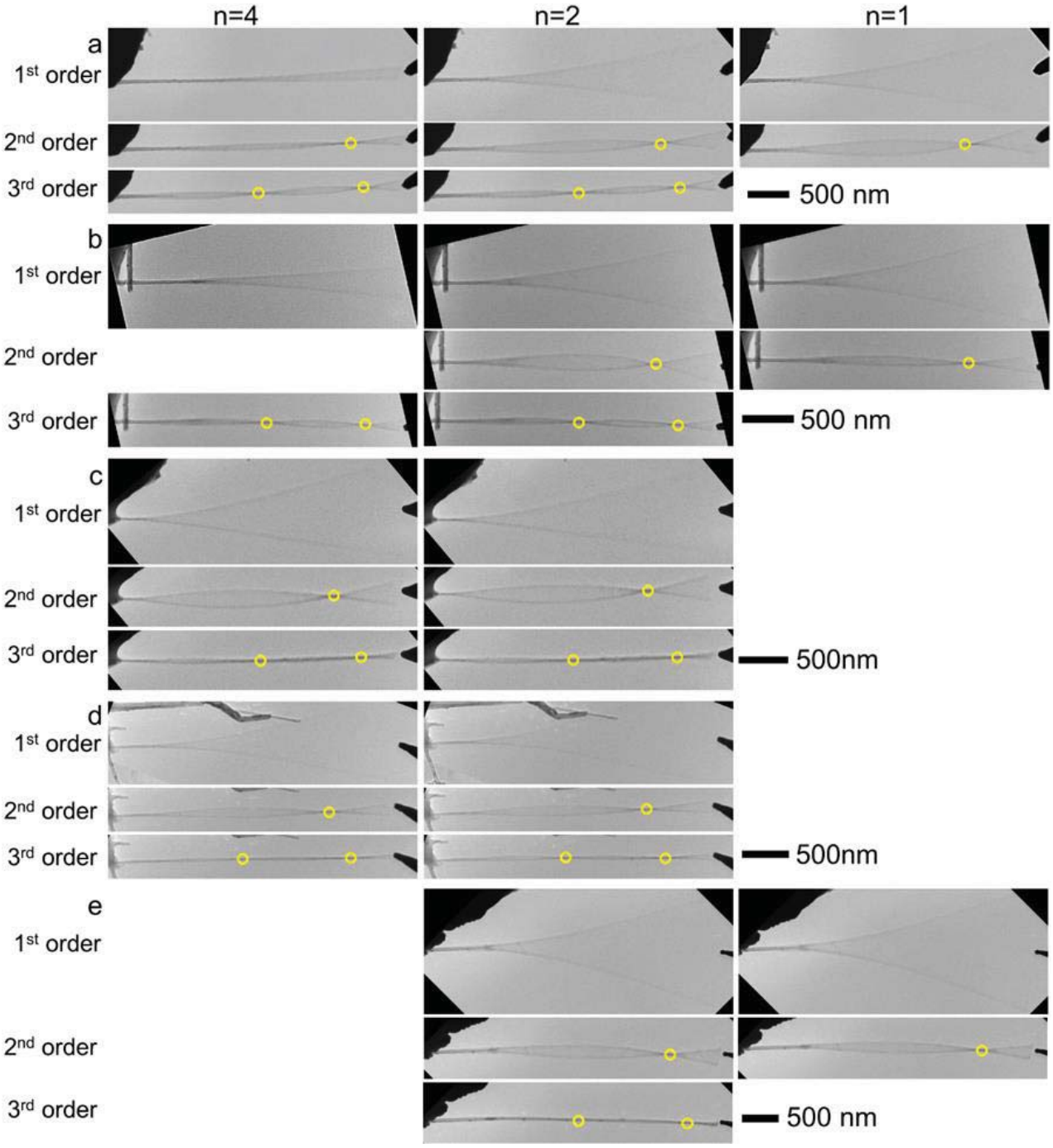

Figure 2.8 (a)-(e) Natural (n=2) and parametric (n=1 and n=4) resonance modes for 5 additional individual BNNTs at different resonance orders. Nodes in each resonance order and mode are marked by yellow circles.

2.4.2 Intrinsic elastic moduli of BNNTs

In total, 15 individual BNNTs were tested and their elastic moduli are summarized in **Figure 2.9** and **Table 2.1. Figure 2.9a** shows the distribution of elastic moduli acquired from the 1st order, with an average value of 952 GPa, at a standard deviation of 17.3 %. The average moduli estimated from 2nd and 3rd orders are 883 GPa and 913 GPa, respectively (**Figure 2.9b** and **c**). It is worth mentioning that the standard deviations for calculated results from 2nd and 3rd orders are much smaller, *i.e.* 9.5 % and 8.9 %, respectively. In addition, the

elastic modulus obtained from the parametric mode (n=4) is 934 GPa on average (**Table 2.2**), consistent with those measured from the natural mode, and also shows a smaller standard deviation at high resonance orders. For comparison, the previously reported results on BNNTs moduli are plotted in **Figure 2.9d**. The average value in our work is consistent with previous results, but the modulus has a much smaller distribution range and standard deviation, proving the high precision of the currently implemented high-order resonance method.

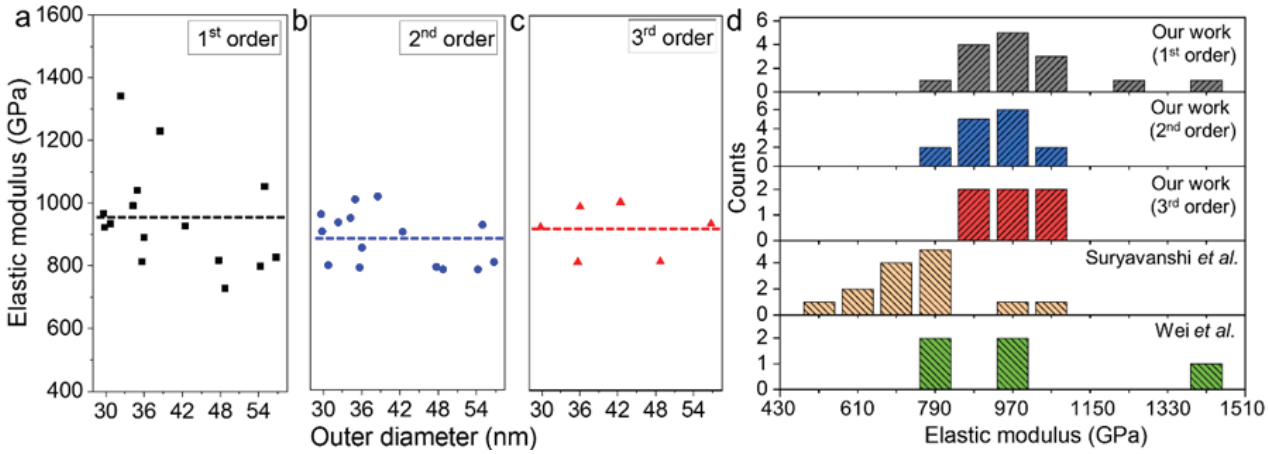

Figure 2.9 (a-c) Elastic moduli distribution for 15 individual BNNTs acquired from 1st, 2nd, and 3rd order resonance, respectively. The dashed line in each panel denotes the average value of elastic modulus. (d) Histograms showing the comparison of the elastic modulus distributions of BNNTs between our results and those reported in the literatures.

Table 2.1 Summary of structural parameters and elastic moduli obtained from natural resonance mode of all measured BNNTs

Sample number	Outer diameter (nm)	Inner diameter (nm)	Length (nm)	Elastic modulus evaluated from different resonance order (GPa)			
				1st order	2nd order	3rd order	4th order
1	30.7	13.1	2886.7	934	799	-	-
2	34.2	8.9	2253.4	991	951	-	-
3	35.0	11.7	2849.4	1040	1011	-	-
4	54.3	15.7	3424.1	799	786	-	-
5	54.9	10.2	3123.7	1053	929	-	-
6	48.7	21.9	5531.1	728	786	811	-
7	47.7	19.5	3454.2	817	794	-	-
8	42.4	12.9	4140.1	927	906	1002	-
9	35.7	13.2	4704.	813	792	810	-
10	29.8	8.6	5114.5	922	908	922	989
11	36.1	14.2	4256.3	890	856	987	-
12	38.5	14.8	3165.9	1229	1020	-	-
13	29.6	9.8	3392.2	966	963	-	-

14	32.3	11.6	3594.1	1341	937	-	-
15	56.7	25.8	5277.4	827.2	810	933	
Average				952	883	913	
Standard deviation				17.3%	9.5%	8.9%	

Table 2.2 Summary of elastic moduli obtained from parametric resonance mode (n=4) of those BNNTs in Table 1

Sample number	Elastic modulus evaluated from different resonance order (GPa)		
	1st order	2nd order	3rd order
2	1015	966	-
4	793	803	-
5	926	945	-
6	746	809	825
8	927	965	1006
9	831	-	840
10	971	-	951
11	893	859	997
12	1192	1082	983
13	1002	959	-
Average	930	923	934
Standard deviation	13.7%	10.2%	8.6%

2.4.3 Effects of intrinsic defects

Though the intrinsic moduli of BNNTs were precisely determined from the high order resonance method, it is also noticed that the measured moduli still have a standard deviation of around 9 %, which is much higher than the precision of the current method (~ 1 %). A careful HRTEM characterization revealed that intrinsic defects, mainly cavities within the walls could be observed, which are unavoidable for practical materials along a length of several micrometers. Representative intrinsic defects related to elastic moduli for different nanotubes are shown in **Figure 2.10a-c**. There are 6 cavities found for the BNNT in **Figure 2.10a**, and its modulus is calculated to be 812 GPa. Two cavities were found in the inner walls of the BNNT in **Figure 2.10b**, its modulus was calculated to be 929 GPa. For the defect-free BNNT in Figure 2.10c, the modulus was the highest one, *i.e.* 1011 GPa, consistent with the theoretical calculations. It is the first time that the intrinsic elastic properties of the BNNTs are precisely measured and directly correlated to the distribution of the intrinsic

defects.

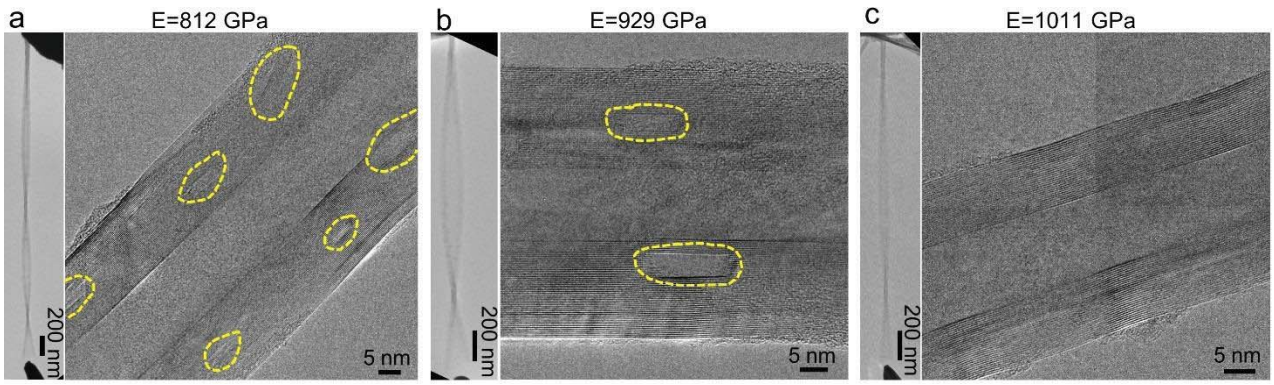

Figure 2.10 Resonances of three individual BNNTs with different moduli and HRTEM images showing the details of their structure. Cavities are marked by dashed yellow lines.

2.5 Summary

In this study, high quality BNNTs were synthesized *via* the BOCVD method. Then, a high-order resonance method was developed to precisely evaluate the elastic properties of BNNTs, and up to 4th order resonances of individual BNNTs were firstly observed. Significantly, the as-proposed method exhibits an ultra-high precision (1 %). Then, the average modulus of BNNTs was evaluated to be around 906 GPa with a standard deviation of ~ 8.9 %. All the recorded frequencies and node positions at high order resonances agree well with the E-B beam theory. In addition, a combination of the detailed structure investigation and the statistical analysis of the moduli for BNNTs led us to conclude that the intrinsic defects are responsible for the modulus distribution. The current technique provides a way to precisely determine the elastic properties of BNNTs, such method can also be applied for other 1D structures.

2.6 References

(1) Hao, S.; Zhou, G.; Duan, W.; Wu, J.; Gu, B. L. Transverse Pressure Induced Phase Transitions in Boron Nitride Nanotube Bundles and the Lightest Boron Nitride Crystal. *J. Am. Chem. Soc.* **2008**, *130* (15), 5257–5261.

(2) Wirtz, L.; Rubio, A.; De La Concha, R.; Loiseau, A. Ab Initio Calculations of the Lattice Dynamics of Boron Nitride Nanotubes. *Phys. Rev. B - Condens. Matter Mater. Phys.* **2003**, *68* (4), 1–13.

(3) Golberg, D.; Bando, Y.; Eremets, M.; Takemura, K.; Kurashima, K.; Tamiya, K.; Yusa, H. Boron Nitride Nanotube Growth Defects and Their Annealing-out under Electron Irradiation. *Chem. Phys. Lett.* **1997**, *279* (3–4), 191–196.

(4) Zheng, F. W.; Zhou, G.; Hao, S. G.; Duan, W H.. Structural Characterizations and Electronic Properties of Boron Nitride Nanotube Crystalline Bundles. *J. Chem. Phys.* **2005**, *123* (12), 124716-1-5.

(5) Oh, E. S. Elastic Properties of Boron-Nitride Nanotubes through the Continuum Lattice Approach. *Mater. Lett.* **2010**, *64* (7), 859–862.

(6) Wang, J.; Lee, C. H.; Yap, Y. K. Recent Advancements in Boron Nitride Nanotubes. *Nanoscale* **2010**, *2* (10), 2028–2034.

(7) Vaccarini, L.; Goze, C.; Henrard, L.; Hernández, E.; Bernier, P.; Rubio, A. Mechanical and Electronic Properties of Carbon and Boron-Nitride Nanotubes. *Carbon* **2000**, *38* (11), 1681–1690.

(8) Song, Y.; Sun, Y.; Shin, D. H.; Yun, K. N.; Song, Y. H.; Milne, W. I.; Lee, C. J. Excellent Oxidation Endurance of Boron Nitride Nanotube Field Electron Emitters. *Appl. Phys. Lett.* **2014**, *104* (16).

(9) Kang, J. H.; Sauti, G.; Park, C.; Yamakov, V. I.; Wise, K. E.; Lowther, S. E.; Fay, C. C.; Thibeault, S. A.; Bryant, R. G. Multifunctional Electroactive Nanocomposites Based on Piezoelectric Boron Nitride Nanotubes. *ACS Nano* **2015**, *9* (12), 11942–11950.

(10) Kim, K. S.; Kim, M. J.; Park, C.; Fay, C. C.; Chu, S. H.; Kingston, C. T.; Simard, B. Scalable Manufacturing of Boron Nitride Nanotubes and Their Assemblies: A Review. *Semicond. Sci. Technol.* **2017**, *32* (1), 013003-1-8.

(11) Bosak, A.; Serrano, J.; Krisch, M.; Watanabe, K.; Taniguchi, T.; Kanda, H. Elasticity of Hexagonal Boron Nitride: Inelastic x-Ray Scattering Measurements. *Phys. Rev. B - Condens. Matter Mater. Phys.* **2006**, *73* (4), 1–4.

(12) Ghassemi, H. M.; Yassar, R. S. On the Mechanical Behavior of Boron Nitride Nanotubes. *Appl. Mech. Rev.* **2010**, *63* (2), 1–7.

(13) Akdim, B.; Pachter, R.; Duan, X.; Adams, W. W. Comparative Theoretical Study of Single-Wall Carbon and Boron-Nitride Nanotubes. *Phys. Rev. B - Condens. Matter Mater. Phys.* **2003**, *67* (24), 1–8.

(14) Wei, X.; Wang, M. S.; Bando, Y.; Golberg, D. Tensile Tests on Individual Multi-Walled Boron Nitride Nanotubes. *Adv. Mater.* **2010**, *22* (43), 4895–4899.

(15) Koi, N.; Oku, T.; Inoue, M.; Suganuma, K. Structures and Purification of Boron Nitride Nanotubes Synthesized from Boron-Based Powders with Iron Particles. *J. Mater. Sci.* **2008**, *43* (8), 2955–2961.

(16) Lim, S. H.; Luo, J.; Ji, W.; Lin, J. Synthesis of Boron Nitride Nanotubes and Its Hydrogen Uptake. *Catal. Today* **2007**, *120*, 346–350.

(17) Han, W.; Bando, Y.; Kurashima, K.; Sato, T. Synthesis of Boron Nitride Nanotubes from Carbon Nanotubes by a Substitution Reaction. *Appl. Phys. Lett.* **1998**, *73* (21), 3085–3087.

(18) Arenal, R.; Ferrari, A. C.; Reich, S.; Wirtz, L.; Mevellec, J. Y.; Lefrant, S.; Rubio, A.; Loiseau, A. Raman Spectroscopy of Single-Wall Boron Nitride Nanotubes. *Nano Lett.* **2006**, *6* (8), 1812–1816.

(19) Saha, S.; Muthu, D. V. S.; Golberg, D.; Tang, C.; Zhi, C.; Bando, Y.; Sood, A. K. Comparative High Pressure Raman Study of Boron Nitride Nanotubes and Hexagonal Boron Nitride. *Chem. Phys. Lett.* **2006**, *421* (1–3), 86–90.

(20) Bai, X. D.; Wang, E. G.; Gao, P. X.; Wang, Z. L. Measuring the Work Function at a Nanobelt Tip and

at a Nanoparticle Surface. *Nano Lett.* **2003**, *3* (8), 1147-1149.

(21) Shi, Y.; Chen, C. Q.; Zhang, Y. S.; Zhu, J.; Yan, Y. J. Determination of the Natural Frequency of a Cantilevered ZnO Nanowire Resonantly Excited by a Sinusoidal Electric Field. *Nanotechnology* **2007**. *18*, 075709-1-6.

(22) Li, P. F.; Liao, Q. L.; Yang, S. Z.; Bai, X. D.; Huang, Y. H.; Yan, X. Q.; Zhang, Z.; Liu, S.; Lin, P.; Kang, Z.; Zhang, Y. *In Situ* Transmission Electron Microscopy Investigation on Fatigue Behavior of Single ZnO Wires under High-Cycle Strain. *Nano Lett.* **2014**, *14*, 480-485.

(23) Yu, M. F.; Wagner, G. J.; Ruoff, R. S.; Dyer, M. J. Realization of Parametric Resonances in a Nanowire Mechanical System with Nanomanipulation inside a Scanning Electron Microscope. *Phys. Rev. B* **2002**, *66*, 073406-1-4.

(24) Jia, Y.; Du, S.; Seshia, A. A. Twenty-Eight Orders of Parametric Resonance in a Microelectromechanical Device for Multi-Band Vibration Energy Harvesting. *Sci. Rep.*. **2016**, 6, 1-8.

(25) Wang, M. S.; Kaplan-Ashiri, I.; Wei, X. L.; Rosentsveig, R.; Wagner, H. D.; Tenne, R.; Peng, L. M. *In Situ* TEM Measurements of the Mechanical Properties and Behavior of WS_2 Nanotubes. *Nano Res.* **2008**, *1* (1), 22–31.

(26) Gibson, R. F.; Ayorinde, E. O.; Wen, Y. Vibrations of Carbon Nanotubes and Their Composites : A Review. *Compos. Sci. Technol.* **2007**, *67*, 1–28.

(27) Stokey, W. F. Harris' Shock and Vibration Handbook, Sixth Edition. Vibration of Systems Having Distributed Mass and Elasticity, *McGraw-Hill Professional, New York, USA*. **2002**, 1-50.

(28) Hsia, F. C.; Tang. D. M.; Jevasuwan, W.; Fukuta, N.; Zhou, X.; Mitome, M.; Bando, Y.; Nordling T. E. M.; Golberg, D. Realization and Direct Observation of Five Normal and Parametric Modes in Silicon Nanowire Resonators by *In Situ* Transmission Electron Microscopy. *Nanoscale Adv.* **2019**, *1*, 1784-1790.

Chapter 3

Effects of extrinsic defects on modulating the mechanical properties of BNNTs

3.1 Introduction

Under the context of a huge passion for human beings to long-term space travels and explorations and the existence of severe space irradiation, exploring structural materials which can suppress the irradiation to somewhat acceptable level and to ensure the safety would be essential and necessary.[1] As for BNNTs, the National Aeronautics and Space Administration (NASA) has shown that BNNTs are promising materials for shielding space radiation due to their large neutron capture cross-section.[1,2] high thermal and chemical stability, and good thermal conductivity.[2–4] Undoubtedly, irradiation may cause structure change and introduce defects in materials and further alter their physical properties and devices' performances. Electron beam irradiation has been regarded as an effective way to modify or engineer BN nanostructures among all known defect introduction approaches. Though many works have been done, all of them are concentrated on the defect formation mechanism in BNNTs and BN nanosheets during the irradiation process, while none of them studied the effects of irradiation-induced defects on the mechanical properties of BNNTs. Therefore, *via in situ* observation, we can get a clear idea about the irradiation process-microstructure (defects)-properties relationships, which can further guide the design of devices to realize the above-mentioned space shielding application of BNNTs.

Thus, in this Chapter, the defects engineering and their effects on affecting the elastic modulus of BNNTs were studied based on the above mentioned high-order resonance method. The defects were deliberately introduced by irradiating the sample under the 300 kV electron beam. In the meantime, the structure evaluation during the irradiation process was monitored and the moduli at different irradiation stages were studied. Experimental results manifested that defects generation and their aggregation are responsible for determining BNNTs' elastic modulus. The latter showed a quick decrease, then reached a stable plateau along with increasing the electron irradiation dose. A core-shell model was proposed that can explain such trend well.

3.2 Experimental set-up

The experimental set-up for the tensile test is illustrated in **Figure 3.1a** and **b**. For pristine BNNTs, they

were fixed on the Au support by using a silver epoxy, then the free end of a selected BNNT was clamped to the AFM cantilever by using the electron-beam-induced-deposition (EBID) technique.[5,6] The BNNTs were stretched by moving the Au support backward until they were ruptured. Part of the BNNT was still maintained on the AFM cantilever after its fracture, then we replaced the Au support with Au probe and irradiated the residual BNNT with different irradiation doses. After the irradiation at different stages, we welded the BNNT with Au probe or AFM cantilever (depends on where the fracture position occurred) *via* the EBID method. The BNNT was stretched by moving the Au support backward until it was ruptured in a "sword-in-sheath" manner (**Figure 3.1a**). The "sheath" part of the BNNT was still maintained on the AFM cantilever after its fracture, then we used an Au probe to test the tensile strength of the BNNT under increasing irradiation doses (**Figure 3.1b**).

Before the tensile experiments, the spring constant (k) of the AFM cantilever was calibrated by measuring its structural parameters using an optical microscope (**Figure 3.1c**) and SEM. The spring constant is given by:[7,8]

$$k = E \cdot w \cdot \frac{t^3}{4 \cdot l^3} \qquad (3.1)$$

where E is Young's modulus of the standard Si (100) materials, with a value about 160 GPa, w, t, and l are the width, thickness, and length of the AFM cantilever, respectively. In our work, the nominal spring constant of the used AFM cantilever was 3.1 N/m.

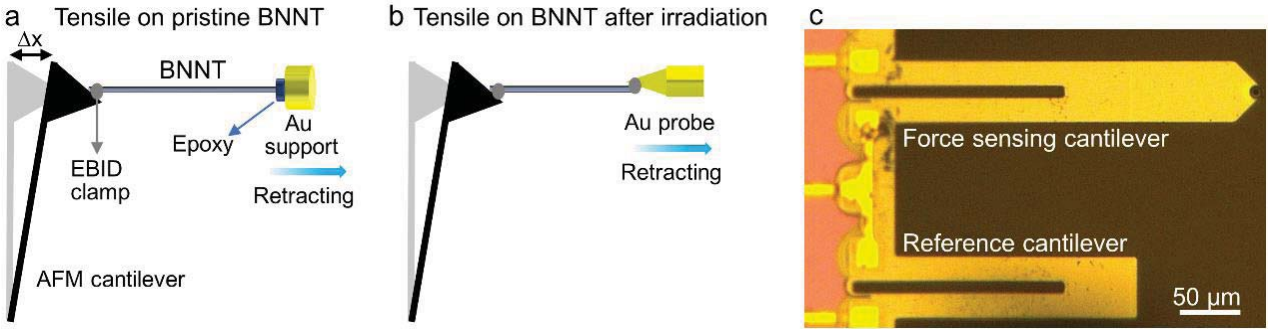

Figure 3.1 Schematic illustration of the experimental set-up for tensile test to evaluate the fracture strength of BNNTs: (a) for pristine BNNT, (b) the "sheath" of the BNNT in (a). The Au support or probe was manipulated by a piezo-motor to perform the tensile test. And the loading force is recorded by a Si cantilever. (c) Optical microscope image of the sensing cantilever along with a reference cantilever.

3.3 Results and discussion

3.3.1 Structure evolution of BNNTs during irradiation

Besides the intrinsic elastic properties, the effects of the extrinsic defects on properties have further been investigated. Such effects are critical for the mechanical applications in harsh environments, for example, for shielding coatings on spaceships, as envisioned by NASA.[1,2] The structural material for spacecraft must tolerate the irradiation from the high-energy cosmic rays. In our work, we have made use of the 300 keV electron beam and the associated knock-on effects to investigate the formation of defects and their influences

on the elastic properties. **Figure 3.2a** depicts a series of high-resolution TEM images for an individual BNNTs during the irradiation process, showing that the inner diameter of the tube kept almost unchanged, while the outer diameter kept decreasing. **Figure 3.2b** and **Figure 3.2c** summarize the changes of the outer and inner diameters for different irradiated BNNTs, respectively. All tubes exhibited a similar behavior, *i.e.* the outer diameter decreases, following a linear relationship with the irradiation dose, while the inner diameter was kept unchanged, implying that the defects have been mainly generated in the outer shells.

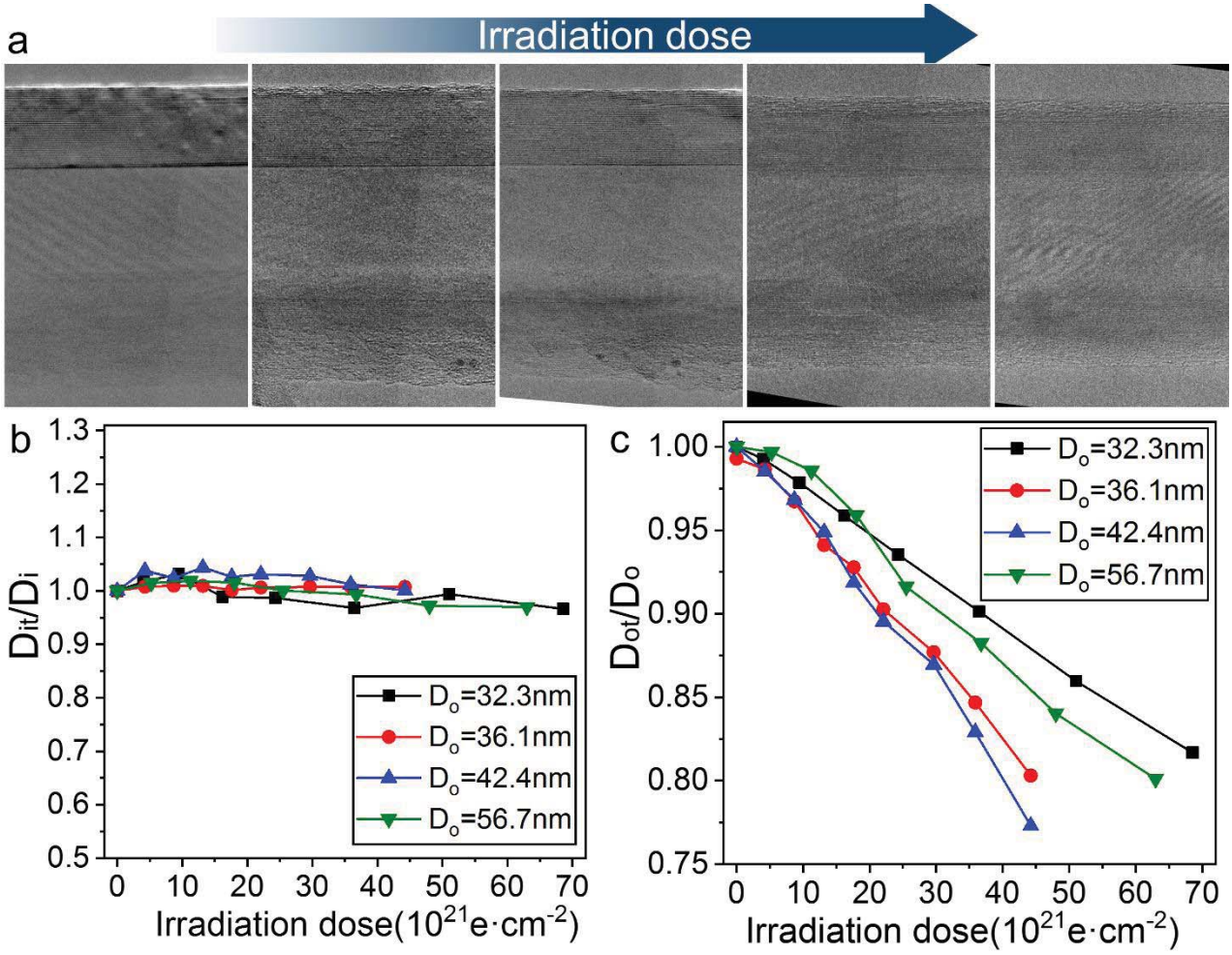

Figure 3.2 (a) HRTEM images of an individual BNNTs during irradiation process; (b) Variation of inner diameters of 4 individual BNNTs along with increasing irradiation dose. D_{it} and D_i denote the inner diameter at different irradiation dose and original inner diameters, respectively; (c)The reduction of outer diameters of 4 individual BNNTs with increasing irradiation dose.

3.3.2 Moduli change of BNNTs during irradiation

Figure 3.3a depicts the changes of resonance frequency along with increasing irradiation dose. The observed behavior can be divided into two stages, *i.e.* a quick decrease until a dose ~ 22.5×10^{21} e·cm^{-2}, and slowing down of this trend at the higher doses. Based on Equation (2.4), the reduction of the elastic modulus was estimated and plotted in **Figure 3.3b**. Along with the increase of the electron irradiation dose, the elastic modulus gradually decreases and then reaches a plateau. The reduction of modulus shows a size-dependent

behavior, *i.e.*, the smaller the diameter, the larger the modulus loss (the final modulus loss is 29.2%, 26.3%, 21.3% and 19.2% for BNNTs with the outer diameter of 32.3 nm, 36.1 nm, 42.4 nm, and 56.7 nm, respectively). Such behavior can be ascribed to a larger defect density in the smaller nanotubes because the curvature induced strain lowers the threshold energy for atom displacement.[9,10] Nevertheless, it is worth noting that BNNTs are still able to maintain a very high level of elastic modulus ~ 662.9 GPa, which is 3 times that of steel.[11]

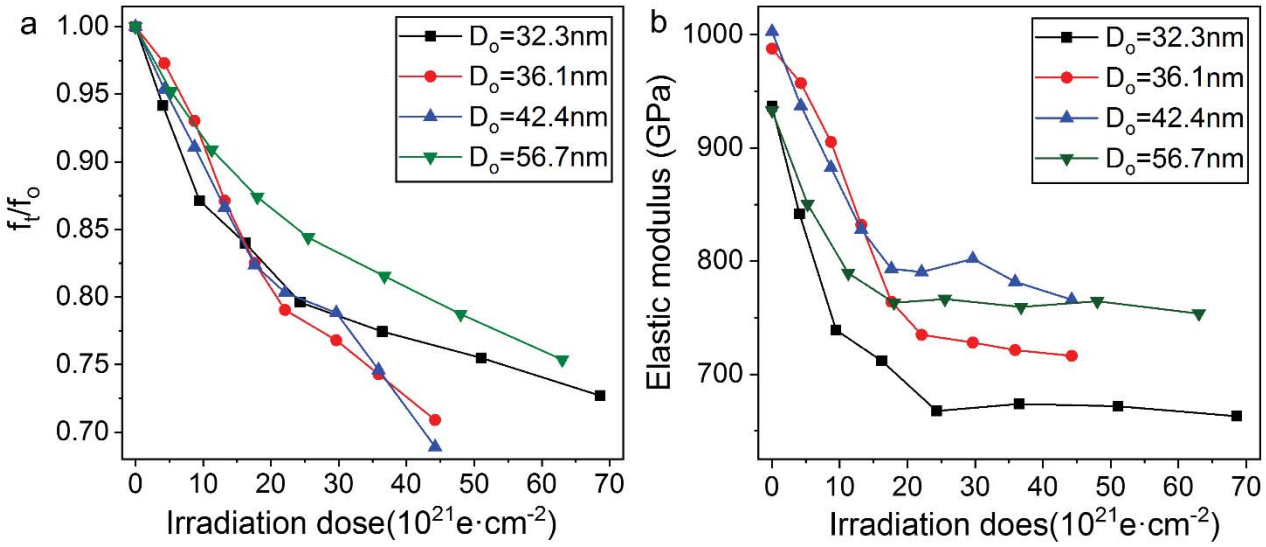

Figure 3.3 (a) The reduction of resonance frequencies of 4 individual BNNTs with increasing irradiation dose; (b) The relationship between elastic moduli of BNNTs and irradiation dose.

3.3.3 Fracture strength change of BNNTs during irradiation

Effects of irradiation on the fracture strength of BNNTs were studied by tensile test *via* applying a AFM-TEM holder. Representative results for a BNNT is shown in **Figure 3.4**. TEM images in the upper panel of Figure 3.4 reveal that the nanotube got ruptured, and the 'sword and sheath' behaviour was observed for the pristine BNNTs. HRTEM image in the middle panel depicts that the fracture end shows that the walls become defective after irradiation. The lower panel in **Figure 3.4** reveals the typical time-force (black) and time-stress (blue) curves. From the time-force curve, the maximum force drops were obtained and the values are 2564.9 nN, 2670.8 nN, 1557.1 nN and 1499.7 nN for the BNNT with increasing irradiation dose. Correspondingly, the fracture strength was evaluated using the following formula: $\sigma = \frac{F}{s} = \frac{k\Delta x/cos\theta}{s}$, where k is the spring constant of the AFM cantilever with a value of 3.1 N/m, Δx is the deflection of the cantilever, θ is the angle between the tube axis and the trace of cantilever deflection and $s = \frac{\pi({D_o}^2 - {D_i}^2)}{4}$ is the cross-section area of the fractured end, where D_o and D_i are the outer and inner diameters, respectively. Thus, the fracture strength was evaluated to be 11.2 GPa, 8.9 GPa, 7.4 GPa, and 6.4 GPa for the pristine BNNTs, and under the irradiation dose of 11.3×10^{21} e·cm^{-2}, 26.3×10^{21} e·cm^{-2}, 43.1×10^{21} e·cm^{-2}, respectively, this presents a decreasing tendency with increasing irradiation dose.

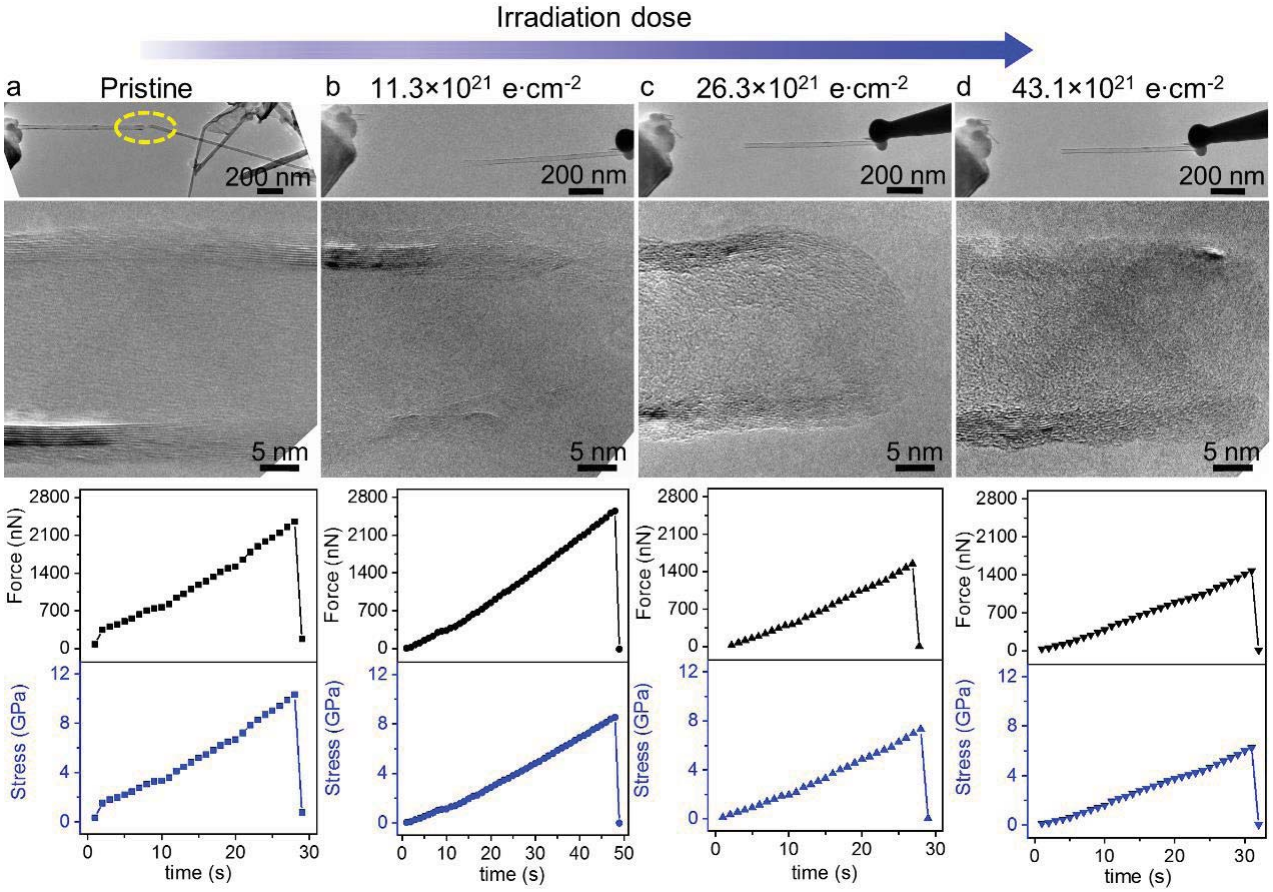

Figure 3.4 TEM images of the fractured BNNTs after the tensile test (upper panel), HRTEM images of the fractured BNNTs (middle panel), and time-force and time-stress curves of a pristine BNNT (a) and that subjected to different irradiation doses (b-d).

We summarized the dependence of the maximum forces when the fracture occurred on the irradiation dose for different BNNTs, as shown in **Figure 3.5a**. Overall, the maximum force exhibited a decreasing tendency. Subsequently, the relationship between the fracture strength and irradiation dose was evaluated, as depicted in **Figure 3.5b**. It is found that these BNNTs exhibit the original fracture strength in a range of 11.2 – 17.1 GPa, this agrees well with the previous work. And, it's clear that the fracture strength keeps decreasing along with irradiation dose. Meanwhile, it is worth noting that the loss of fracture strength (~53.4 %) is higher than the loss of the maximum force (~ 40.5 %), implying that the cross-section area increased along with irradiation. These results suggest that that some kind of interlinking bridges in BNNT appeared during electron beam irradiation.

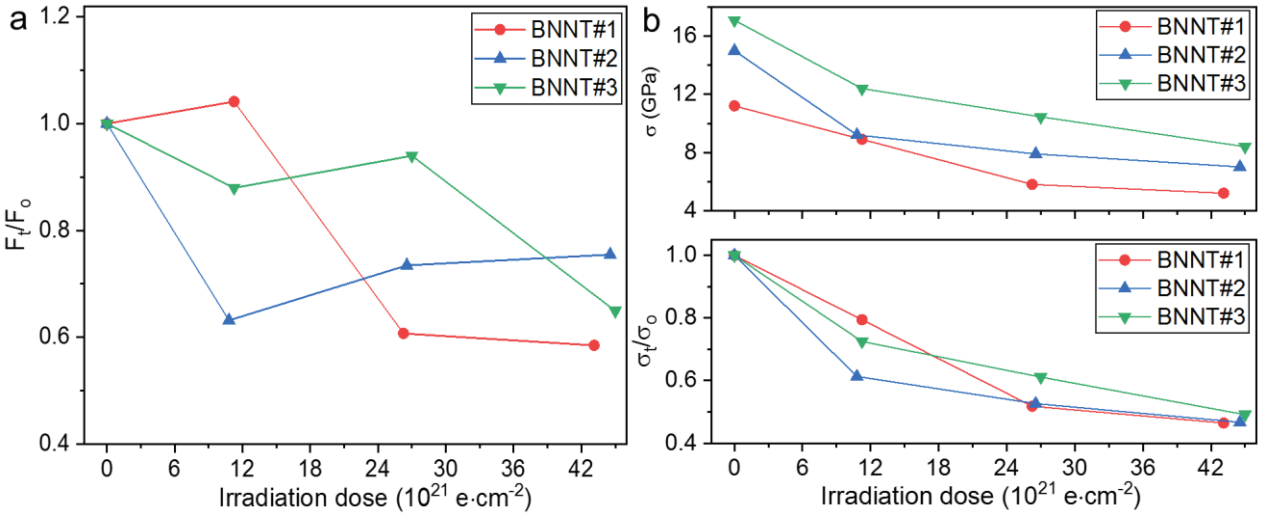

Figure 3.5 (a) Variation of the maximum force when the BNNT was fractured under a tensile test along with increasing the tube electron irradiation dose; (b) Reduction of fracture strength along with irradiation dose.

3.3.4 Comparative study on CNTs during irradiation

A comparative experimental study on the effects of irradiation-induced defects on alternating the elastic modulus of CNTs was then conducted. The CNTs were synthesized through an arc-discharge method and the experimental set-up was the same as that for BNNTs. **Figure 3.6a** and b show the 1st and 2nd resonance for a CNT, the frequency relationship between different orders, as well as the node position for the 2nd order, these follow well the *E-B* beam theory These results further document the high precision of the currently employed method. The pristine moduli for CNTs with outer diameters of 10.1 nm, 15.2 nm, and 44.8 nm were estimated to be 1146.9 GPa, 1030.6 GPa, and 913.2 GPa (**Figure 3.6e**), respectively, these values are in good accordance with the theoretical values and previous reports. Then, the experiments on structural evolution and moduli response to irradiation were carried out inside a 300 kV electron microscope. **Figure 3.6b** depicts a series of HRTEM images of a CNT (D_o=15.2 nm) during the electron beam irradiation process, corresponding to the points 1-8 in **Figure 3.6f**. Two main conclusions can be drawn comparing to BNNTs, (1) the originally straight walls become wavy, indicating that they become heavily defective and even amorphized owing to the knock-on effects; (2) instead of a continuous decrease in the outer diameter and the final core (intact)-shell (defective) structure formation for BNNTs during irradiation, no obvious size reduction is found for CNT, implying that the irradiation-induced defects are generated within the entire tube. **Figure 3.6c** summarizes the outer and inner diameters variation during irradiation, showing that both of them kept almost unchanged, further confirming that the defects are generated within the whole tube. **Figure 3.6d** depicts the reduction of resonance frequency along with increasing irradiation dose. Similar to BNNTs, the observed behavior can be divided into two stages. However, it reaches the boundary between the two stages at a relatively small dose of ~ 12.0×10^{21} e·cm^{-2}, which is about half of that for BNNTs. Subsequently, the modulus values are calculated based on Equation (2.4) and the reduction of modulus is plotted in **Figure 3.6e** and **f**. Comparing with modulus behavior of BNNTs during irradiation, both the similarity and difference can be pointed out: (1) the size-dependent

phenomenon was also observed for CNTs, *i.e.* the smaller the outer diameter, the larger the modulus loss, which can be ascribed to the existence of a higher strain in smaller nanotubes; (2) The moduli of CNTs show a much sharper decrease trend at the initial stage of electron irradiation than that of BNNTs (a dose less than ~ 12.0×10^{21} e·cm^{-2}). With further increasing irradiation dose, the moduli of CNTs keep decreasing with a smaller slope (instead of a plateau observed for BNNTs). Moreover, the CNTs breaks with the further increasing dose and the final modulus is measured to be around 284.2 GPa (before the tube is broken), which is half less than that of BNNTs (~ 662.9 GPa). In conclusion, irradiation-induced defects caused the modulus decrease for both BNNTs and CNTs. However, different structural evaluation process was observed for them, *i.e.* core (intact)-shell (defective) structure formed for BNNTs, where the whole tube become defective and even amorphized for CNTs. Moreover, the dependence of moduli for BNNTs and CNTs on irradiation dose clearly manifest that BNNTs maintain a much higher modulus (~ 662.9 GPa) at a higher irradiation dose (~ 68.4×10^{21} e·cm^{-2}) than that of CNTs (~ 284.2 GPa) at a dose of ~ 43.4×10^{21} e·cm^{-2}, implying their superior shielding capability over CNTs. We propose that these distinct behaviours for BNNTs and CNTS are originated from their different electrical characteristics, as well as different bond nature. It was found that the sizes of CNTs kept almost unchaged and the whole tube became defective with increasing irradiation dose. This comparision clearly indicates that BNNTs have a superior capability (over CNTs) with respect to irradiation resistance.

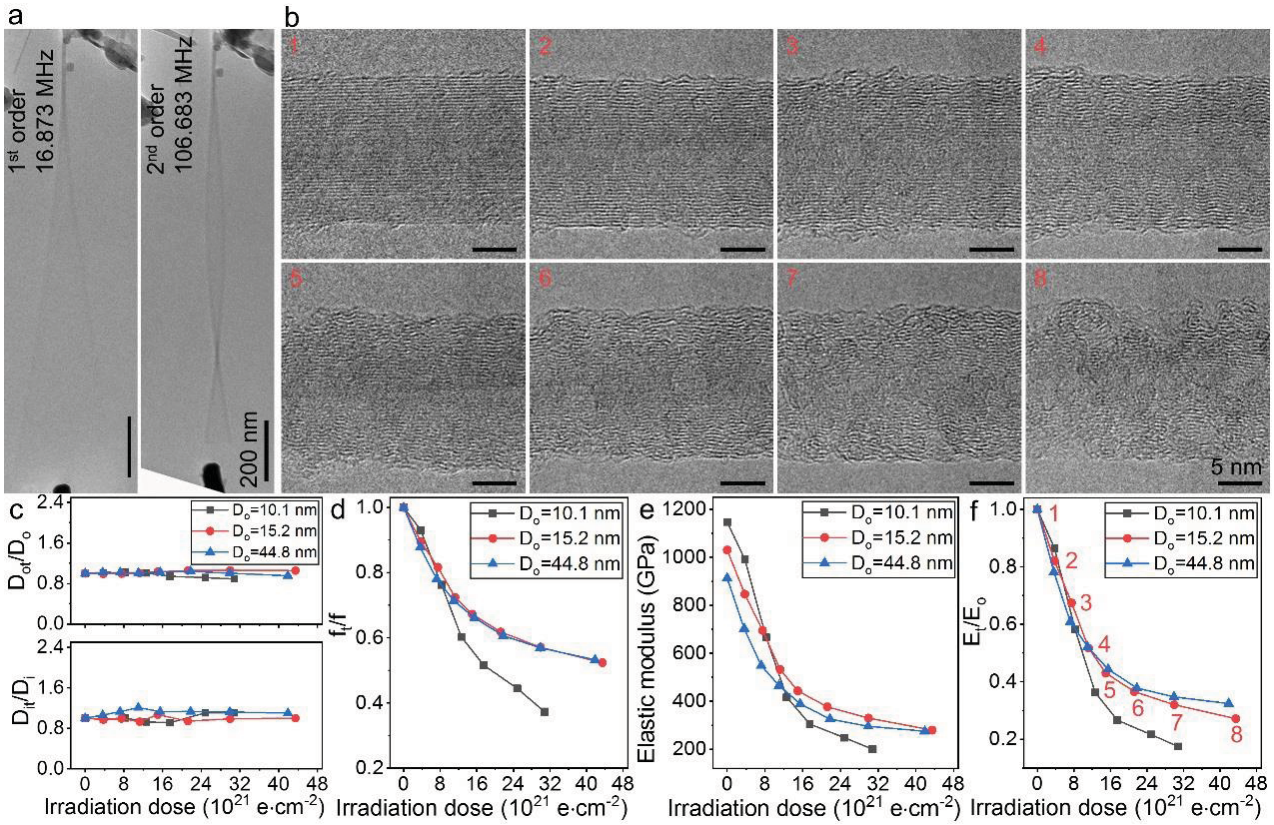

Figure 3.6 (a) TEM images showing the 1st and 2nd order resonances of a CNT. (b) A series of HRTEM images showing the structural evolution of a CNT during electron irradiation, corresponding to the points in (f). (c) Dependence of outer and inner diameters of CNTs on irradiation dose. (d) The reduction of resonance frequencies with increasing irradiation dose. (e) and (f) Modulus value change and reduction of modulus during

irradiation.

3.3.5 Mechanism for the moduli reduction of BNNTs

It is surprising that the modulus could be kept at a high level for BNNTs, instead of decreasing continuously under increasing the irradiation dose. A close-up examination of the structural evolution during the irradiation process was then conducted. **Figure 3.7** shows a series of HRTEM images of a selected BNNT (D_o=56.7nm) during the electron beam irradiation process. Irradiation-induced vacancies appear owing to the knock-on collisions,[12] then these vacancies merge and expand, and finally, lead to a complete shell removal, *i.e.* a continuous reduction of the outer diameter. At the same time, defective layers are formed on the outside of BNNT (marked by yellow rectangles and dashed lines in **Figure 3.7**). The thickness of defective layer increases with irradiation, and finally reaches an equilibrium thickness of ~ 3.2 nm. It reveals that the unique structure evolution (core(intact)-shell (defective), finally formed) is responsible for the peculiar modulus changing behavior of BNNTs during irradiation.

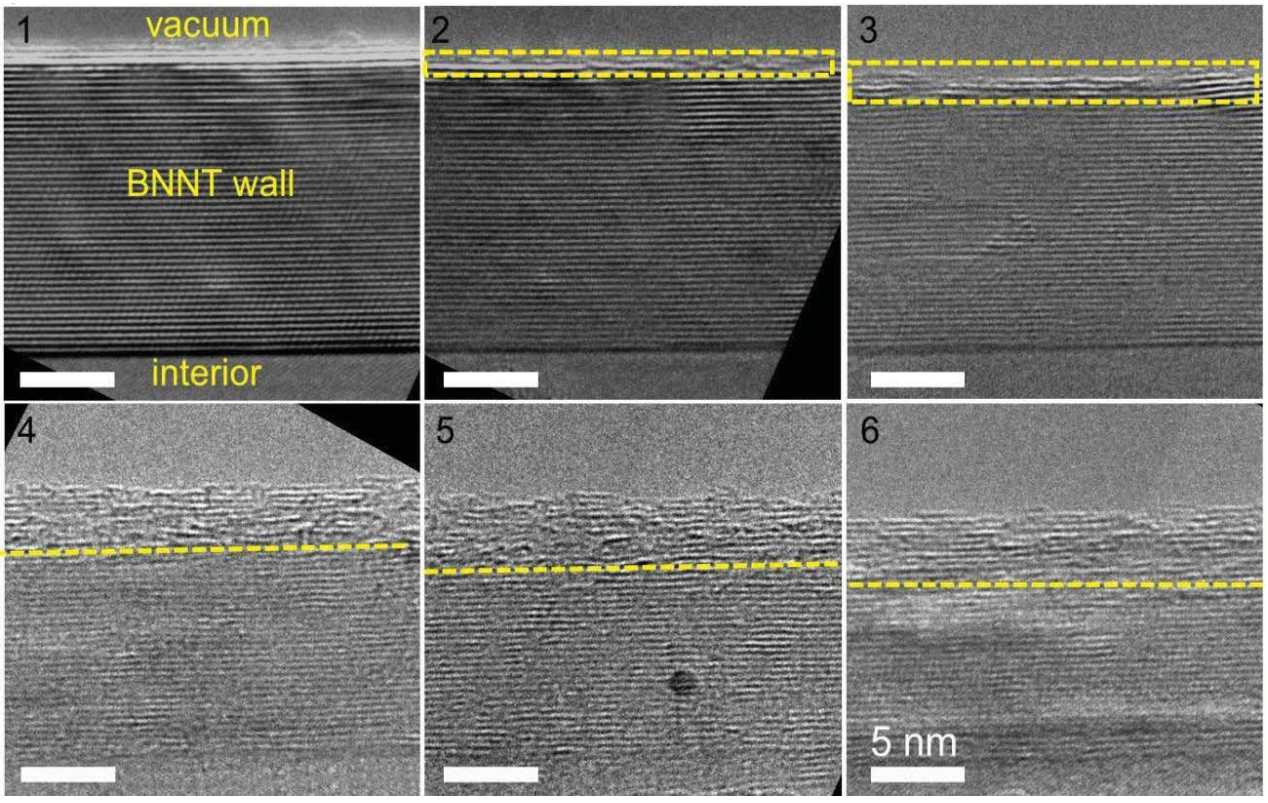

Figure 3.7 A series of HRTEM images illustrating the structural evolution of a BNNT during electron beam irradiation, this reveals a continuously decreased outer diameter and formation of a defective surface layer with a thickness of ~ 3.2 nm.

The defects density ($\rho(t)$) in the defective shell was estimated by employing the knock-on displacement theory. According to this theory, the atom number ($N(t)$) as a function of irradiation time (t) is expressed as:[13–15]

$$\frac{dN(t)}{dt} = -N(t) \cdot \sigma \cdot j \qquad (3.2)$$

where σ is the knock-on cross-section, and j is the beam current density. And the defects density ($\rho(t)$) can be determined as:

$$\rho(t) = \frac{N_k(t)}{N_0} = \frac{N_0 - N(t)}{N_0} = \frac{N_0 - N_0 e^{-\sigma j t}}{N_0} = 1 - e^{-\sigma j t} \qquad (3.3)$$

where $N_k(t)$ is the number of knocked-out atoms, and N_0 is the total number of atoms at the beginning of irradiation. Theoretical calculations have revealed that the knock-on cross-sections for B and N atoms vary for pristine structure and for those with vacancies under 300 keV beam irradiation.[12,16] In our case, a mean value of 30.2 barn was used and the calculated defects concentration against irradiation dose is plotted in Figure 3.8. From our *in situ* observations, the modulus reached the plateau and a defect layer with constant thickness formed at a dose ~ 22.5×10^{21} e·cm^{-2}. Accordingly, the defects density in the defective layer is estimated to be ~0.49.

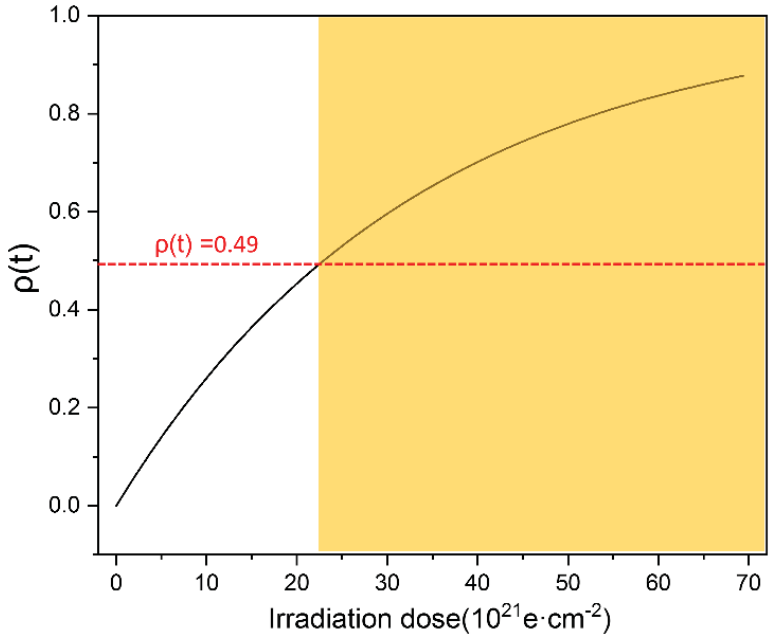

Figure 3.8 Defects density as a function of irradiation dose. Defects density is estimated *via* knock-on displacement theory.

Subsequently, the modulus of the defective shell was estimated by treating it as a porous material, since the atoms within such shell are removed during irradiation. The elastic modulus of porous solids can be described as:[17,18]

$$E_p \sim E_s \cdot \left(\frac{\rho_p}{\rho_s}\right)^m \qquad (3.4)$$

where E_p and E_s are the elastic moduli, ρ_p and ρ_s are the densities for porous and compact materials, respectively. It has been reported that the power m is ~1 for hexagonal solids.[19] Thus, in our case, the modulus of the defective shell can be estimated as:

$$E_{shell} \sim E_o \cdot (1 - \rho) = 0.51 E_o \quad (3.5)$$

where E_o is the original modulus of pristine BNNTs. The estimated values for shell modulus range from 477.8 GPa to 511.4 GPa, with an average value of 489.8 GPa.

Based on the above discussions, a core-shell model is proposed to understand the change of elastic modulus under electron beam irradiation: [20–22]

$$E_{eff} I_{eff} = E_{core} I_{core} + E_{shell} I_{shell} \quad (3.6)$$

where E_{eff} is the effective modulus of the core-shell BNNTs, which can be obtained *via* Equation (2.4), E_{core} and E_{shell} are the elastic moduli of the pristine core and defective shell, respectively. I_{eff}, $I_{core,}$ and I_{shell} are the moments of inertia of the cross-section for the whole nanotube, core, and shell, respectively. The modulus in the constant region and structural parameters (when the shell thickness became almost unchanged) were used to estimate the elastic modulus of the defective shell. The results are shown in **Figure 3.9**. It is found that the defective BN shells from these BNNTs have a consistent elastic modulus, not very different from each other, with an average value of around 521.5 GPa, and this value agrees well with the above-mentioned calculations. Furthermore, by combining this value with Equation (3.6), a thickness of the defective BN shell was estimated. The results agree well with the experimental measurements (**Figure 3.10**).

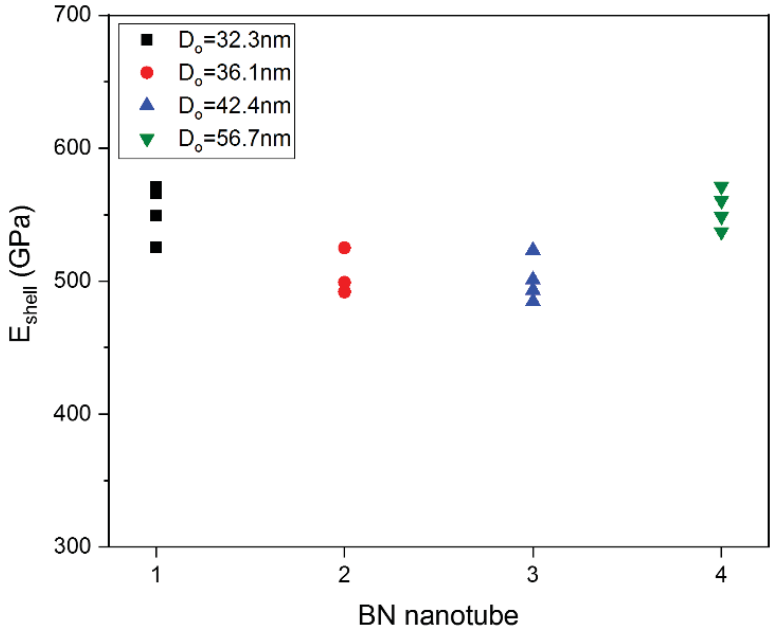

Figure 3.9 The elastic modulus of a defective shell evaluated from the steady modulus region for 4 BNNTs in Figure 4(c) *via* applying the core-shell model.

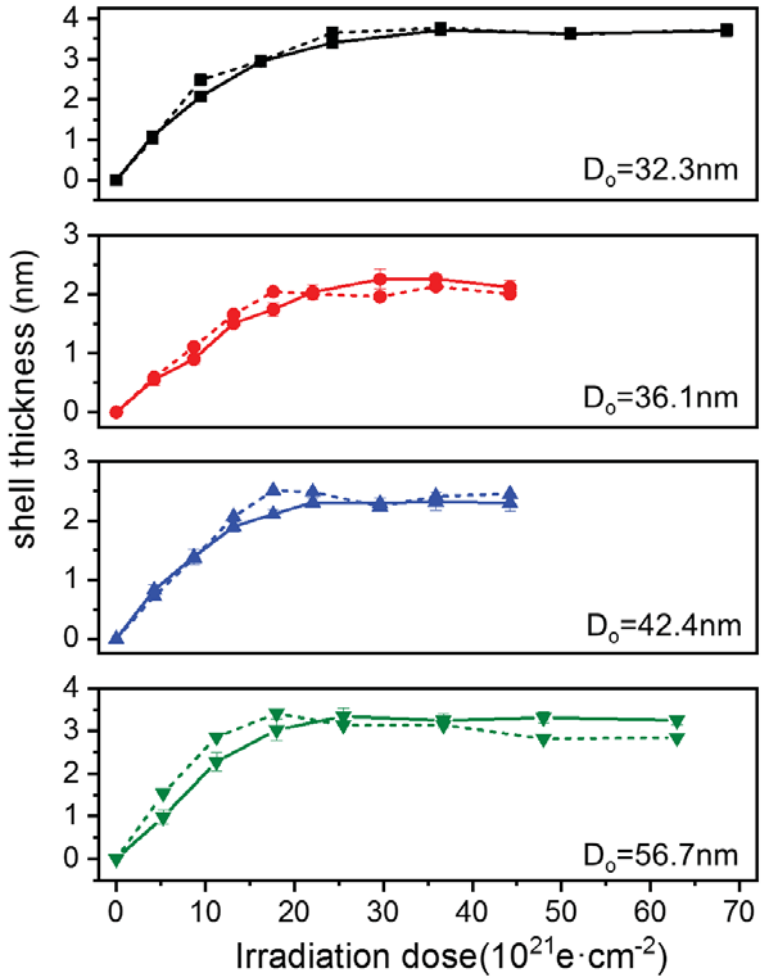

Figure 3.10 Comparison of shell thickness for BNNTs obtained from real-time HRTEM images (solid line) and the theoretical calculation results (dash line) *via* applying the core-shell model.

3.4 Summary

In this Chapter, the extrinsic effects of defects on affecting the mechanical properties of BNNTs were studied. The extrinsic defects were introduced under controlled electron beam irradiation in the microscope. It was found that due to the formation of an equilibrium defective surface layer the elastic modulus of BNNTs has decreased gradually to a plateau at ~ 662.9 GPa, it is noted that this number is still 3 times of that of steel. A comparative experimental study on the effects of irradiation-induced defects on alternating the elastic moduli of CNTs was then conducted. It was found that the moduli of CNTs kept decreasing with the irradiation dose and had a more remarkable loss than that of BNNTs, particularly at a high dose. In addition, the effects of irradiation on the fracture strength of BNNTs were investigated by conducting the tensile tests. Overall, it was found that both the ultimate force and the fracture strength exhibited a decreasing tendency along with the irradiation dose. Interestingly, the reduction of the ultimate force (~ 40.5 %) was not as significant as the loss of the strength (~ 53.4 %), implying that the loading cross-section area increased along with irradiation, suggesting that inter-plane bridges might have been formed between the walls during beam irradiation. Decent radiation-resistance prove that BNNTs could be a material of choice for applications in extreme environments,

such as those existing in space.

3.5 References

(1) Ghazizadeh, M.; Estevez, J. E.; Kelkar, A. D. Boron Nitride Nanotubes for Space Radiation Shielding. *Int. J. Nano Stud. Technol.* **2015**, *4*, 1–2.

(2) Kim, J. H.; Pham, T. V.; Hwang, J. H.; Kim, C. S.; Kim, M. J. Boron Nitride Nanotubes: Synthesis and Applications. *Nano Converg.* **2018**, *5*, 17-29.

(3) Jiang, X.; Weng, Q.; Wang, X.; Li, X.; Zhang, J.; Golberg, D.; Bando, Y. Recent Progress on Fabrications and Applications of Boron Nitride Nanomaterials: A Review. *J. Mater. Sci. Technol.* **2015**, 6, 2-30.

(4) Tiano, A. L.; Park, C.; Lee, J. W.; Luong, H. H.; Gibbons, L. J.; Applin, S. I.; Gnoffo, P.; Lowther, S.; Jung, H.; Danehy, P. M. Boron Nitride Nanotube : Synthesis and Applications. No. Cvd, 23-24.

(5) Tang, D. M.; Ren, C. L.; Wei, X.; Wang, M. S.; Liu, C.; Bando, Y.; Golberg, D. Mechanical Properties of Bamboo-like Boron Nitride Nanotubes by *in Situ* TEM and MD Simulations: Strengthening Effect of Interlocked Joint Interfaces. *ACS Nano* **2011**, *5* (9), 7362–7368.

(6) Carpena-Núñez, J.; Yang, D.; Kim, J. W.; Park, C.; Fonseca, L. F. Mechanical Characterization of Pristine and Hydrogen-Exposed Palladium Nanowires by *in Situ* TEM. *Nanotechnology* **2013**, *24* (3), 035701-1-10.

(7) Shaw, G. A.; Kramar, J.; Pratt, J. SI-Traceable Spring Constant Calibration of Microfabricated Cantilevers for Small Force Measurement. *Exp. Mech.* **2007**, *47* (1), 143–151.

(8) Gibson, C. T.; Weeks, B. L.; Abell, C.; Rayment, T.; Myhra, S. Calibration of AFM Cantilever Spring Constants. *Ultramicroscopy* **2003**, *97* (1–4), 113–118.

(9) Li, X.; Cheng, Y.; Zhao, L.; Zhang, Q.; Wang, M. Structural and Electrical Properties Tailoring of Carbon Nanotubes *via* a Reversible Defect Handling Technique. *Carbon* **2018**, *133*, 186–192.

(10) Krasheninnikov, A. V.; Nordlund, K. Ion and Electron Irradiation-Induced Effects in Nanostructured Materials. *J. Appl. Phys.* **2010**, *107 (7)*. 071301-1-70.

(11) ASM International, ASM International. Handbook Committee, and ASM International. Alloy Phase Diagram Committee. Metals Handbook: Properties and selection. *ASM International*, **1990**, 2.

(12) Zobelli, A.; Gloter, A.; Ewels, C. P.; Seifert, G.; Colliex, C. Electron Knock-on Cross Section of Carbon and Boron Nitride Nanotubes. *Phys. Rev. B - Condens. Matter Mater. Phys.* **2007**, *75* (24), 1–9.

(13) Cretu, O.; Lin, Y. C.; Suenaga, K. Inelastic Electron Irradiation Damage in Hexagonal Boron Nitride. *Micron* **2015**, *72*, 21–27.

(14) Peng, B.; Locascio, M.; Zapol, P.; Li, S.; Mielke, S. L.; Schatz, G. C.; Espinosa, H. D. Measurements of Near-Ultimate Strength for Multiwalled Carbon Nanotubes and Irradiation-Induced Crosslinking Improvements. *Nat. Nanotechnol.* **2008**, *3* (10), 626–631.

(15) Banhart, F. Irradiation Effects in Carbon Nanostructures Irradiation Effects in Carbon Nanostructures. *Nanotecnhnology* **1999**, *62*, 1181-1221.

(16) Kotakoski, J.; Jin, C. H.; Lehtinen, O.; Suenaga, K.; Krasheninnikov, A. V. Electron Knock-on Damage in Hexagonal Boron Nitride Monolayers. *Phys. Rev. B* **2010**, *82*, 1–4.

(17) Zheng, X. Y.; Lee, H.; Weisgraber, T. H.; Shusteff, M.; Deotte, J.; Duoss, E. B.; Kuntz, J. D.; Biener, M. M.; Ge, Q.; Jackson, J. A.; Kucheyev, S. O.; Fang, N. X.; Spadaccini, C. M. Ultralight, Ultrastiff Mechanical Metamaterials. *Science* **2014**, *344 (6190)*, 1373–1378.

(18) Kashani, H.; Ito, Y.; Han, J.; Liu, P.; Chen, M. Extraordinary Tensile Strength and Ductility of Scalable Nanoporous Graphene. *Sci. Adv.* **2019**, *1*, 1–7.

(19) Fan, H. Y.; Hartshorn, C.; Buchheit, T.; Tallant, D.; Assink, R.; Simpson, R.; Kissel, D. J.; Lacks, D. J.; Torquato, S.; Brinker, C. J. Modulus – Density Scaling Behaviour and Framework Architecture of Nanoporous Self-Assembled Silicas. *Nature Mater.* **2007**, *6*, 418-423.

(20) Chen, C. Q.; Shi, Y.; Zhang, Y. S.; Zhu, J.; Yan, Y. J. Size Dependence of Young's Modulus in ZnO Nanowires. *Phys. Rev. Lett.* **2006**, *96 (7)*, 075505-1–4.

(21) Ma, J.; Liu, Y.; Hao, P.; Wang, J.; Zhang, Y. Effect of Different Oxide Thickness on the Bending Young's Modulus of SiO_2 @SiC Nanowires. *Sci. Rep.* **2016**, *6*, 1–7.

(22) Zhou, X.; Hsia, F. C.; Xue, Y. M.; Tang, D. M.; Cretu, O.; Zhang, C.; Mitome, M.; Bando. Y.; Sasaki, T.; Golberg, D. Tunable Mechanical and Electrical Properties of Coaxial BN-C Nanotubes. *Phys. Status Solidi RRL* **2018**, 1800576.

Chapter 4

Extrinsic effects of composition on achieving tunable mechanical and electrical properties of coaxial BN-C heterostructures

4.1 Introduction

Heterostructures provide a great chance to tune the properties and functions of a nanomaterial. *e.g.* its mechanical and electrical properties, and thus allow for the design and realization of novel nanoelectromechanical devices. Boron nitride and carbon nanotubes, with similar structure and mechanical properties but dramatically different electrical properties, are ideal candidates for investigating nanoscale heterostructured materials. For example, carbon nanotubes have ultimately high elastic modulus and high electrical conductivity. In contrast, boron nitride nanotubes (BNNTs), with a similar crystalline structure but ionic bonding, have a similarly high modulus coupled with a high electrical resistivity.[1–3] To meet the requirement of a specific application, a specific combination of properties is necessary and may not be fulfilled by one material. For example, one great challenge for bio-implant materials is to find a bio-compatible material with the elastic modulus comparable with that of the tissues such as the bones. Heterostructures constructed from two distinct components, with their individual advantages, can be an effective way to modulate the nanomaterial physical properties.[4] Several research efforts have been directed towards realizing such engineering. Wei *et al*. used substitutional carbon doping for an individual nanotube *via in situ* electron beam irradiation to form a ternary B-C-N compound and finally realized a transformation from insulating to metallic behavior by adjusting the irradiation time.[5] Wang *et al.* used perylene-3,4,9,10-tetracarboxylic acid tetrapotassium salt (PTAS) functionalization and succeeded in C substitution to form coaxial B-C-N/BN nanotubes with modified electrical properties.[6]

Precise measurement of mechanical and electrical properties of individual nanotubes represents a challenging task. Nowadays, several microscopic measurement methods have been developed to understand the mechanical and electrical behaviors of 1D nanomaterials, including *in situ* transmission electron microscopy (TEM), [7,8] *in situ* scanning electron microscopy,[9,10] and atomic force microscopy (AFM). [11,12] Among these methodologies, *in situ* TEM has the advantages of high-resolution real-time imaging and spatially-resolved chemical analysis. [13–15] For example, Tang *et al.* studied the mechanical properties of

bamboo-like BNNTs and realized a strengthening effect of interlocked joint interfaces.[16] Treacy *et al.* observed an exceptionally high Young's modulus for individual CNTs. Wang *et al.* revealed the size effects on the bending modulus of CNTs.[17] Li *et al.* found that wurtzite InAs nanowires have a remarkable piezoelectric effect, which is strongly depended on the crystal orientation and can be suppressed by occasional stacking faults. [18] Zhang *et al.* comparatively studied the photoelectrical performances of pure CdS and composite CdS/ZnO nanobelts and found that a CdS/ZnO heterostructure brings notable advantages over CdS with respect to the photocurrent-to-dark current ratio and responsivity time.[19] Thus, there is no doubt that *in situ* TEM would provide us with a perfect platform to understand the microstructure-properties-processing relationships of the nanosized materials and guide the design of devices with tunable performances.

In this Chapter, the large-scale production of BN-C coaxial nanotubes was realized, allowing for a wide-range adjustment of their electrical and mechanical properties. *In situ* TEM experiments were performed in order to comparably study the mechanical properties of composite BN-C and pure BN nanotubes, as well as the electronic behavior of hybrid BN-C nanocables. As a function of the coated carbon content, the elastic modulus obtained from second order harmonic resonance of heterostructured nanotubes could be tuned from ~140 GPa to ~700 GPa, and their electrical resistivity could be adjusted within three orders of magnitude from ~0.16 Ω·m to ~2.5×10^{-4} Ω·m. This work opens the way for making custom-designed heterostructures for the requirements of specific applications.

4.2 Materials synthesis and characterization

4.2.1 Synthesis of BN-C heterostructures

Tubular BN-C heterostructures were synthesized *via* a three-step chemical vapor deposition (CVD) method, as illustrated in **Figure 4.1** Firstly, high-quality BNNTs were prepared by boron and metal oxide-assisted method (BOCVD) in an induction furnace.[20] Subsequently, a carbon coating was deposited on them *via* another CVD process in a horizontal electrical furnace. The coating was performed under ambient pressure, at a temperature of 1100 ºC for 60 s, with Ar gas and hexane vapor acting as a carrier gas and a carbon source, respectively. Finally, the carbon coated BNNT samples were annealed at 1800 ºC for 6 h to induce complete graphitization and to remove possible impurities.

Some of the BN-C nanotubes underwent subsequent treatment at 650 ℃ for 10 min under a flow of 500 mL/min Ar and 80 mL/min O_2 in a horizontal furnace, in order to remove the coated graphite layers, in agreement with reported thermogravimetric (TG) results.[21]

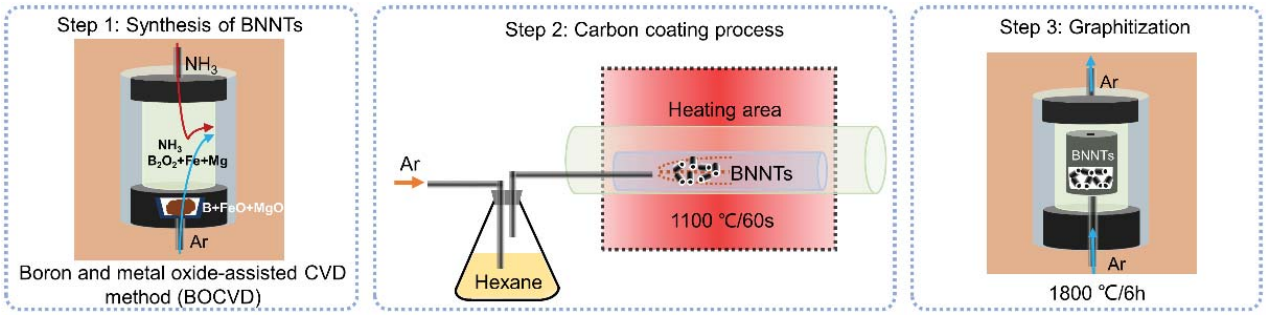

Figure 4.1 Schematic illustration of the core-shell BN-C nanotubes' synthesis.

4.2.2 Characterization of BN-C heterostructures

The SEM image in **Figure 4.2a** shows the morphology BN-C nanotubes, implying that the BN-C sample has diameters of around tens of nanometers, and lengths of up to several micrometers. This confirms that the sample morphology was maintained after the high temperature carbon coating and graphitization process. The optical photographs (inset of the SEM image) distinctly manifest the sample appearance changed from white to black, thus make us believe that the carbon coating was successful. **Figure 4.2b** shows the of the Raman spectra for BN-C NTs. For the BN-C sample, the peaks in the range of 1320-1380 cm^{-1} can be attributed to BNNTs and to the D-band of graphite, while the ones at 1580 cm^{-1} and 1612 cm^{-1} vibrations correspond to the graphite G and D'bands.[22,23]

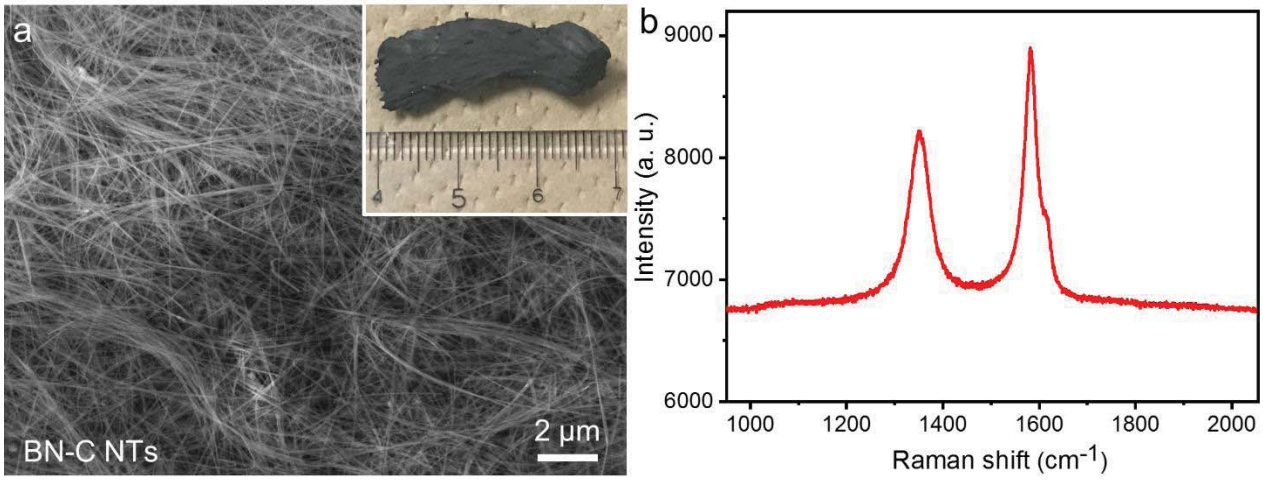

Figure 4.2 (a) SEM image of core-shell BN-C nanotubes. Inset is the photograph of BN-C sample. (b) Raman spectrum of the sample.

Low-magnification TEM image shown in **Figure 4.3a** verified that the hollow and tubular structure was well maintained. High-resolution TEM (HRTEM) HRTEM image (**Figure 4.3b**) reveals the good crystallinity of a BN-C nanotube. In addition, several curved layers are discerned from the HRTEM image of BN-C nanotube, implying that the graphite layers of high quality are successfully and mainly coated on the outside of the BNNTs. **Figure 4.3c** presents the diameter distributions of BN-C nanotubes collected from around 120 individual nanotubes, all of them exhibit the diameters ranging from 30 nm to 100 nm, which match SEM results very well. Meanwhile, the diameter of BN-C NTs is averaged at ~63 nm which is slightly larger than

that of pristine BNNTs (diameter averaged at ~57 nm) and this may result from the carbon coating. The electron energy loss spectrum (EELS) of the samples is depicted in **Figure 4.3d**. Two distinct absorption features corresponding to the known K-shell ionization edges of the B and N atoms starting from 188 and 401 eV, respectively, revealing sharp π* peaks and σ* bands, which is the typical sp^2 bonding configuration [24,25]. While after a careful comparison between the EELS data presented in **Figure 4.3d**, it can be found that in addition to the core-loss K-edges of B and N, the core-loss K-edge of C at 284 eV with well-defined sharp π* and σ* peaks ware also identified in the spectrum of BN-C NTs [5,26], which obviously confirmed that sp^2-hybridized C species had been added to BNNTs.

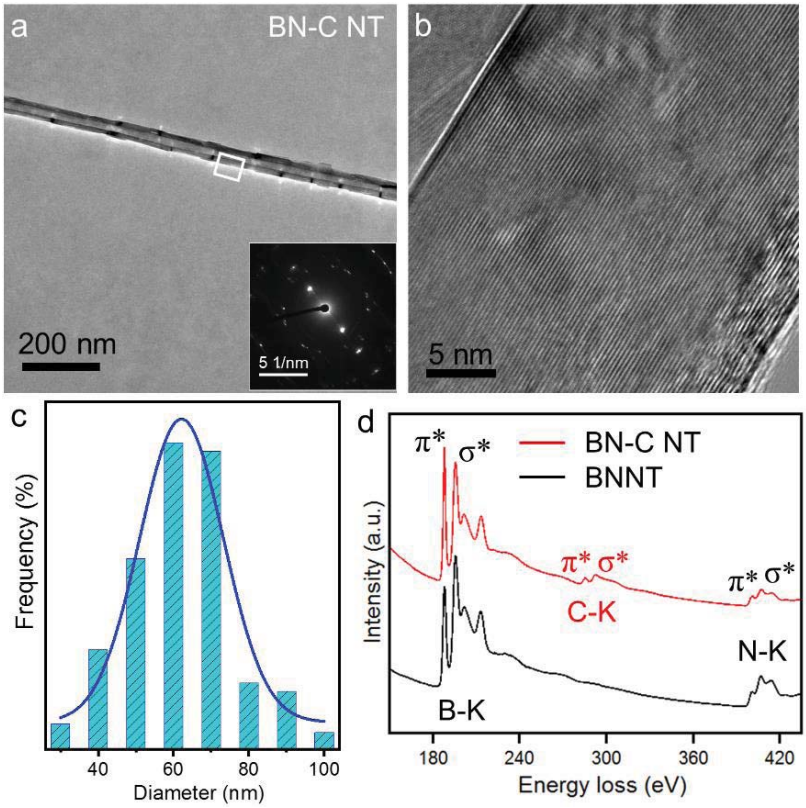

Figure 4.3 (a) Low-magnification TEM image, (b) High-resolution TEM image, (c) Outer diameter distribution diagram of BN-C sample; (d) Comparision of EEL spectra for BNNTs and core-shell BN-C NTs, respectively. The inset in (a) is SAED pattern taken from the BN-C nanotube.

EELS mapping was used in order to determine the spatial distributions of the elements in the sample, which was performed on a JEOL JEM 3000F TEM, operated at 300 kV, using a heating TEM holder to avoid/minimize the possible carbon contamination/deposition during the beam scanning. **Figure 4.4a** shows a HRTEM image from a BN-C nanotube. The high quality of the structure agrees with our previous observations. **Figure 4.4b** shows an annular dark-field (ADF) STEM image of the same tube, acquired ~50 nm from the previous area. **Figure 4.4c** shows a RGB composite map of the exactly same region. It is immediately apparent that the C layers surround the BN scaffold. This is confirmed by looking at spectra "1" and "3" in **Figure 4.4d**, extracted from the outermost regions of the tube, which show only the C signature. Further insight can be gained from analyzing the concentration profiles in **Figure 4.4e**. Here, all three elements display the

characteristic “M”-shaped profile which is expected from a hollow tube. This implies that, at least at this scale, there has been no intermixing between C and B/N. The structure can be regarded as a superposition of two structurally-intact nanotubes. Quantification of the EELS data allows us to estimate around 11 graphite layers, which is in excellent agreement with the result obtained by analyzing the diameter distribution histograms. We can conclude that our nanotubes form unique heterostructured coaxial nanocables.

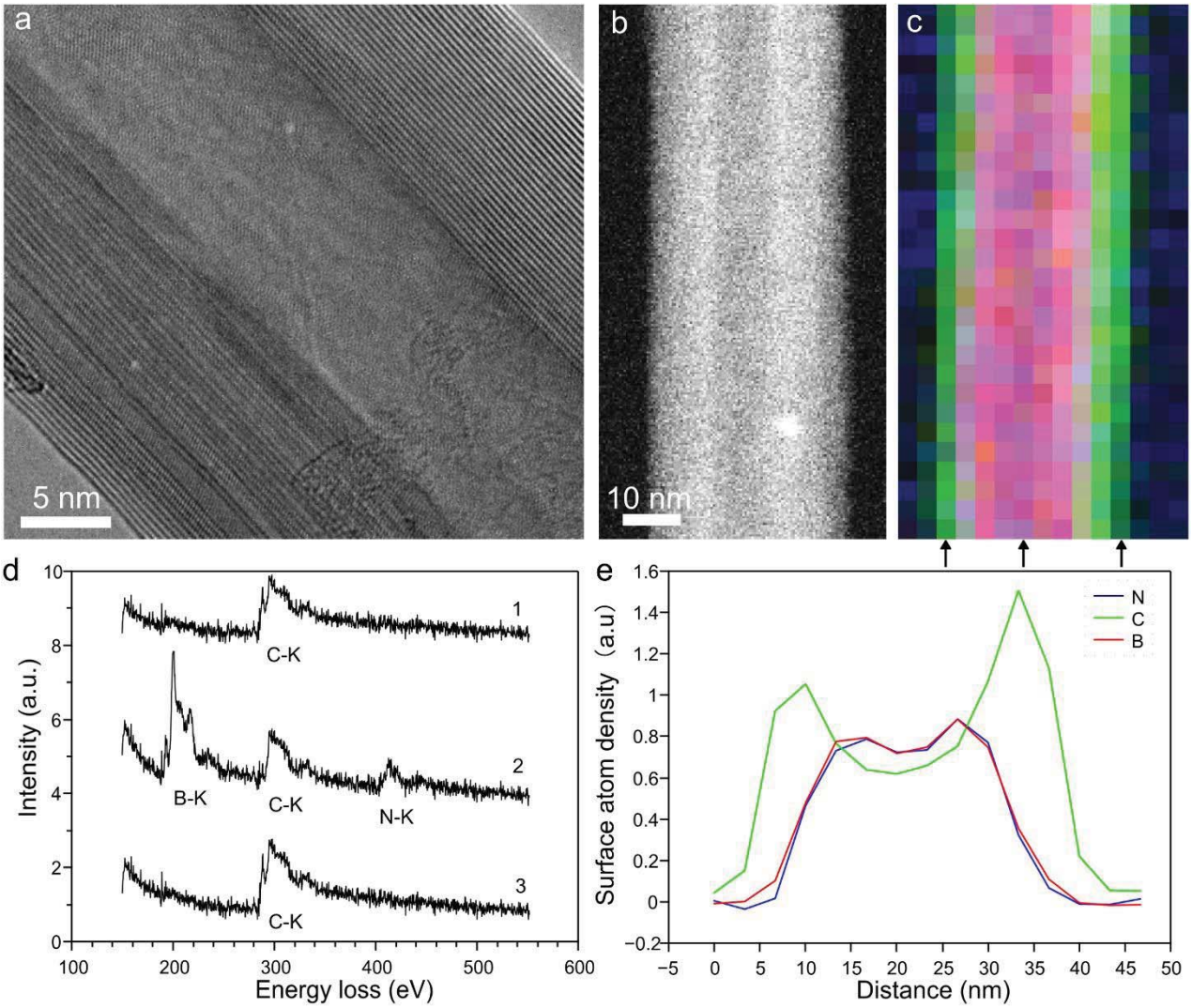

Figure 4.4 (a) HRTEM image of a BN-C nanotube. (b) ADF STEM image acquired next to the area in (a). (c) RGB composite map of the region in (b), showing the distribution of B (red), C (green) and N (blue) species. (d) Averaged EEL spectra extracted from the corresponding regions arrowed in (c). (e) Averaged concentration profiles extracted from the map in (c), perpendicular to the tube axis.

4.3 Experimental set-up for mechanical and electrical measurements

Similar to the precious experimental set-up in the previous Chapter, the *in situ* experiments were carried out inside a JEOL JEM 3100FEF (Omega filter) TEM by using a scanning tunneling microscope-TEM (STM-TEM) holder (Nanofactory Instruments AB). Firstly, BN-C nanotubes were attached to the Au wire by using the flattened Au wire to scratch the sample, then it was blown by a gas gun and heated at 300 ºC under air

atmosphere to make sure that all the nanotubes are clean and have tight contact with Au wire. Then, the gold support with the sample was loaded into the sample holder and a sharp tungsten probe, which was fabricated by electrochemical etching, was used as a counter electrode. The tungsten probe driven by a piezo-tube was manipulated in three dimensions at a nanometer-range precision to contact and test electrical properties of the selected BN-C nanotubes. For mechanical properties measurements, an AC sinusoidal signal provided by a function generator (Tektronix AFG3152C, with frequency swept up to 150 MHz) was applied between an individual BN-C nanotube and the counter tungsten electrode placed close to the tube. The mechanical resonance would be induced when the applied frequency matches the natural vibration frequency. And the resonance was viewed and recorded by a CCD camera.

For the electrical property measurements, the BN-C nanotubes were contacted by the W probe, and the current-voltage (*I-V*) curves were recorded.

4.4 Results and discussion

4.4.1 Length calibration

Based on the above-mentioned details, thelength calibration process was also employed for the measured nanotubes (chapter 2.2). The clibration results for the BN-C nanotubes are shown in **Figure 4.5**. The comparison between the calibrated lengths and the lengths evaluated from the second mode, shown in **Figure 4.5c,** indicating good agreements between these two methods.

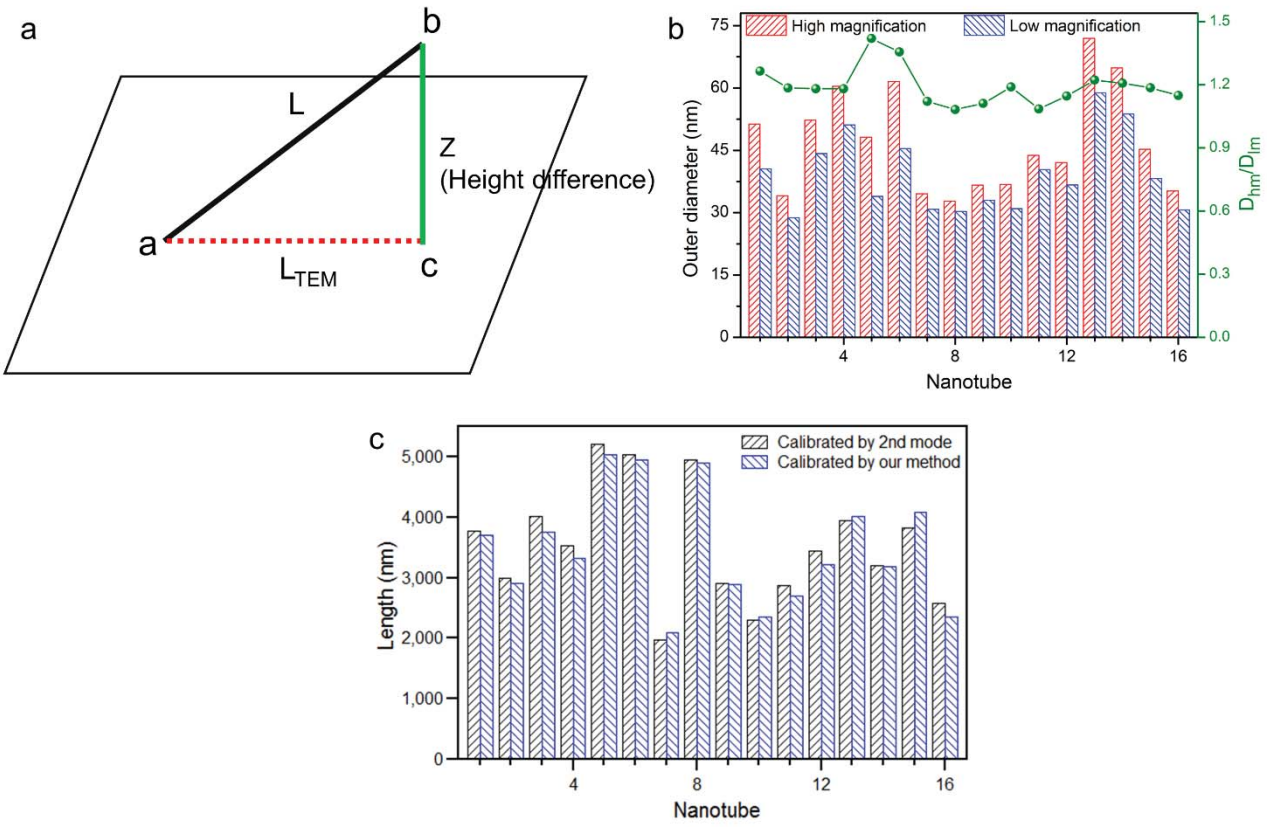

Figure 4.5 (a) Schematic drawing of the relation between the actual nanotube length (*L*) with the projected

nanotube length (L_{TEM}) acquired under TEM imaging. (b) Comparison of the outer diameter at low-magnification (5k-10k, D_{lm}) and high-magnification (200k-300k, D_{hm}). The real nanotube length can be expressed as：$L=(((D_{hm}/D_{lm})\bullet L_{TEM})^2+Z^2)^{1/2}$ (c) Results of the length measurements obtained from the two-step calibration and from the second mode resonance.

4.4.2 Resonance of an individual BN-C nanotube

The experimental setup for the *in situ* TEM mechanical resonance of the BN-C NTs is depicted in **Figure 4.6a**. **Figure 4.6b** shows the TEM image of a selected BN-C nanotube with the outer diameter (D_o), inner diameter (D_i) and length (after calibration) of 52.2, 20.9 and 3757.2 nm, respectively. HRTEM image shown in **Figure 4.6c** reveals the high quality and clean surface of the tube. EEL spectra confirmed the existence of C. (**Figure 4.6d**)The quantification results from EEL spectra give a B/N/C ratio of 1.00:0.93:0.72. By tuning the frequency of the applied potential, the first mode (at f_1=5.60003 MHz) and the second mode harmonic resonances (at f_2=33.88036 MHz) were realized, as shown in **Figure 4.6e** and **f**, respectively. Thus, the f_2/f_1 ratio was estimated to be 6.05, which is in good agreement with the theoretical value of 6.26. Additionally, the node position measured from the second mode resonance (Figure 4.6(f)) was found at 0.749L, which is quite close to the theoretical value of 0.783L. According to the Euler-Bernoulli equation, the elastic modulus of this nanotube calculated from the second mode resonance is 202.9 GPa.

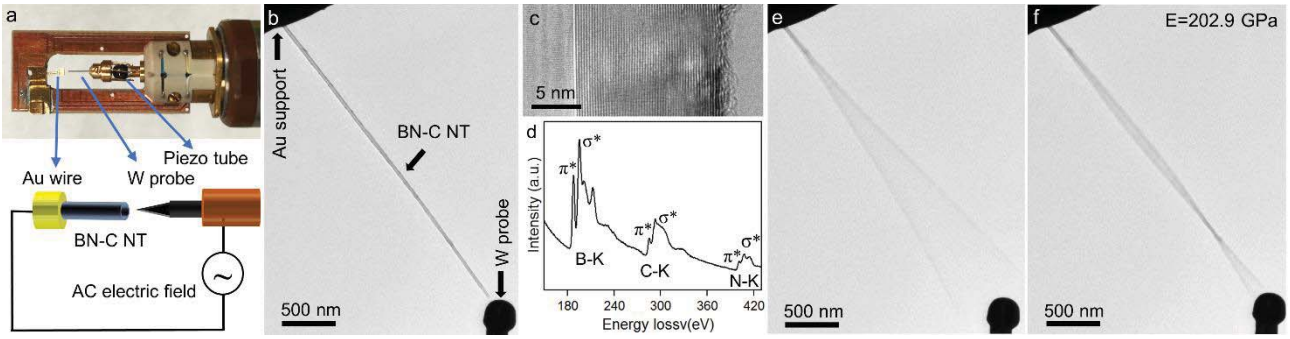

Figure 4.6 (a) Photograph of the front end of the STM-TEM holder and the schematic drawing of the mechanical resonance of an individual core-shell BN-C nanotube. (b) TEM image of an individual cantilevered BN-C nanotube. (c) HRTEM image and (d) EEL spectrum of the BN-C tube chosen for resonant measurements. (e) The first and (f) second mode harmonic resonances of the BN-C nanotube.

4.4.3 Moduli distribution and effects of carbon coating

In order to understand the role which the C graphitic layers play in affecting the mechanical properties of BN-C nanotubes, we performed mechanical resonance experiments (combined with thorough EELS characterization) on 16 individual composite BN-C nanotubes. Additionally, we performed comparative mechanical experiments on the same coaxial nanotube before and after the removal of its graphitic C shells.

A representative experimental result showing the comparison between the same nanotube with and without carbon coating (the latter was removed under the designed thermal treatment) is shown in **Figure 4.7**. No

remarkable structural changes were observed after the removal of the coated graphitic layers (**Figure 4.7a** and **b**). However, the HRTEM images (**Figure 4.7c and d**) clearly revealed that the outer diameter slightly decreased, from around 43.2 nm to 37.7 nm. EELS data, shown in **Figure 4.7e**, confirm that the C peak disappeared after the thermal treatment. Both the first and second mode resonances (**Figure 4.7a** and **b**) were then initiated and the corresponding calculation results from second mode resonance indicate that the elastic modulus of the nanotube after carbon removal (E=373.6 GPa) became higher than that of the initial heterostructured BN-C nanotube (E=308.4 GPa). In addition to the elastic modulus, the quality factor (Q factor) is also an important parameter to evaluate the performance of a mechanical system. It is inversely proportional to energy dissipation. The Q factor is defined as $f_1/\Delta f$, where f_1 is the peak resonant frequency and Δf is the FWHM of the resonant peak that can be evaluated by Lorentz fitting of the amplitude dependency on frequency. Here, Q factors of the nanotubes were measured and compared from their response curves, as displayed in **Figure 4.7f**. It can be seen that the Q factor can be tuned from 386.8 (carbon coated) to 619.7 (carbon removed), which means a faster energy dissipation in the BN-C composite. Finally, the relationship between the elastic modulus of several BN-C nanotubes and their coated graphite content is plotted in **Figure 4.7g**. It is clear that the elastic modulus of the BN-C nanotubes decreases with an increase of C content over a wide range (from ~140 GPa to 706 GPa), which provides a way to tune the mechanical properties of nanotubes for any specific application.

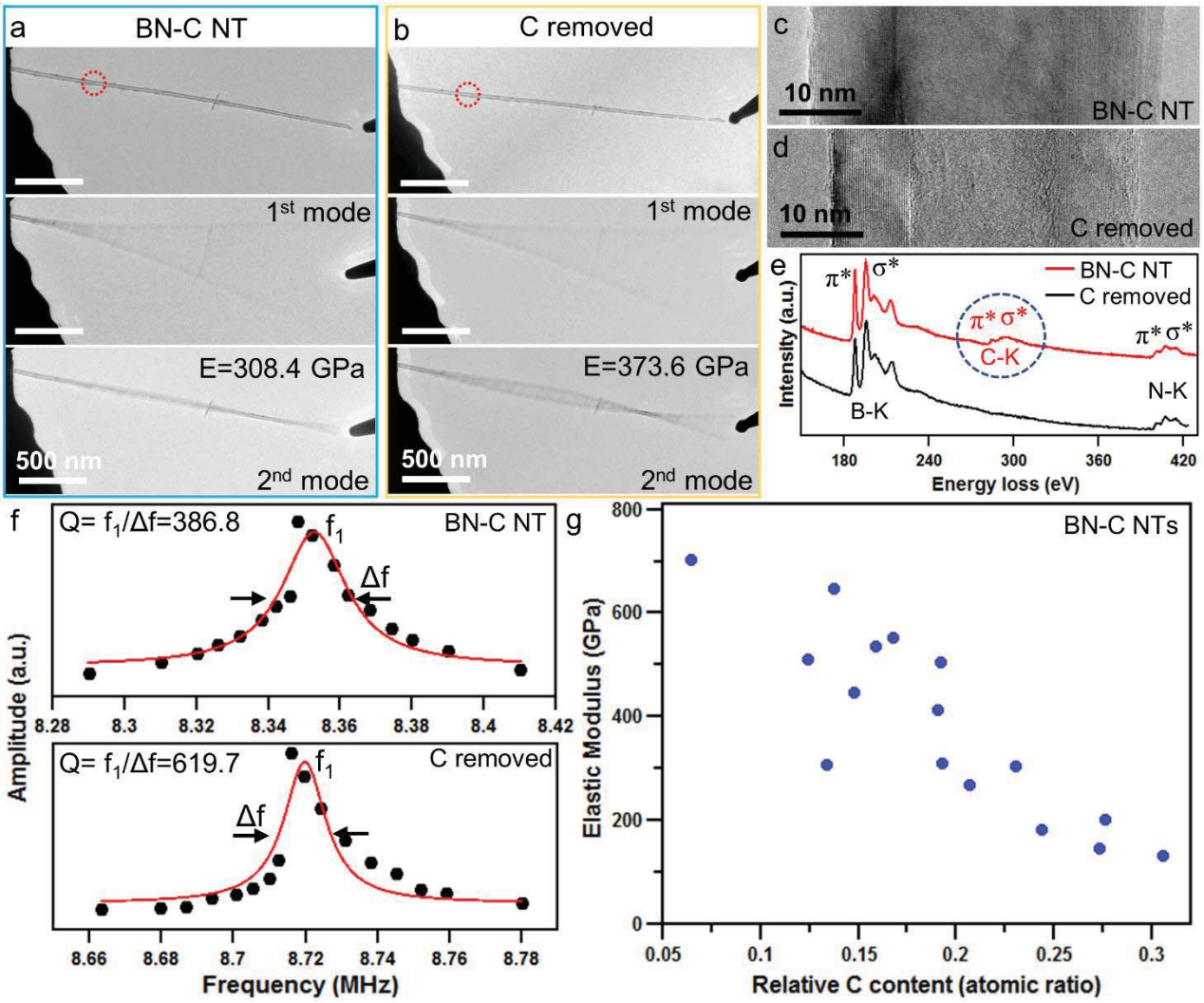

Figure 4.7 (a) and (b) First and second mode harmonic resonances of the same nanotube with graphite layers coated (BN-C NT) and then removed. (c-e) Comparative HRTEM images and EEL spectra taken from the areas marked in (a) and (b), respectively. (f) Response curves of the nanotubes at their first mode resonance. The solid lines are Lorentzian fits for the data points. (g) Calculated relationship between the elastic modulus of 16 individual BN-C nanotubes and the relative coated C content (relative C content is calculated from the EELS quantification results and defined as the atomic ratio between C content and the total content of B, N and C).

The comparative results of mechanical resonance experiments for two additional BN-C nanotubes with and without wrapped graphite layers are illustrated in **Figure 4.8**. Both the elastic modulus and Q factor for these nanotubes can be controlled by adjusting the carbon coating content. (**Figure 4.8a** and **b**) . When trying to evaluate the mechanical properties of the nanotubes using a core-shell model (**Figure 4.8c**), based on the relationship between the effective elastic modulus for each component, we can write that:

$$E_{eff}I=E_cI_c+E_sI_s \quad (4.1)$$

where I_c and I_s are the moments of inertia of the cross section for the core and shell, respectively. In the case of a hollow cylinder, the moment of inertia can be calculated as $I=64\pi(D_o^4-D_i^4)/64$. Using these expressions,

the averaged elastic modulus of the coated graphite layers was calculated as 157.5 GPa (**Figure 4.8d**), which is much smaller than the reported values for CNTs.

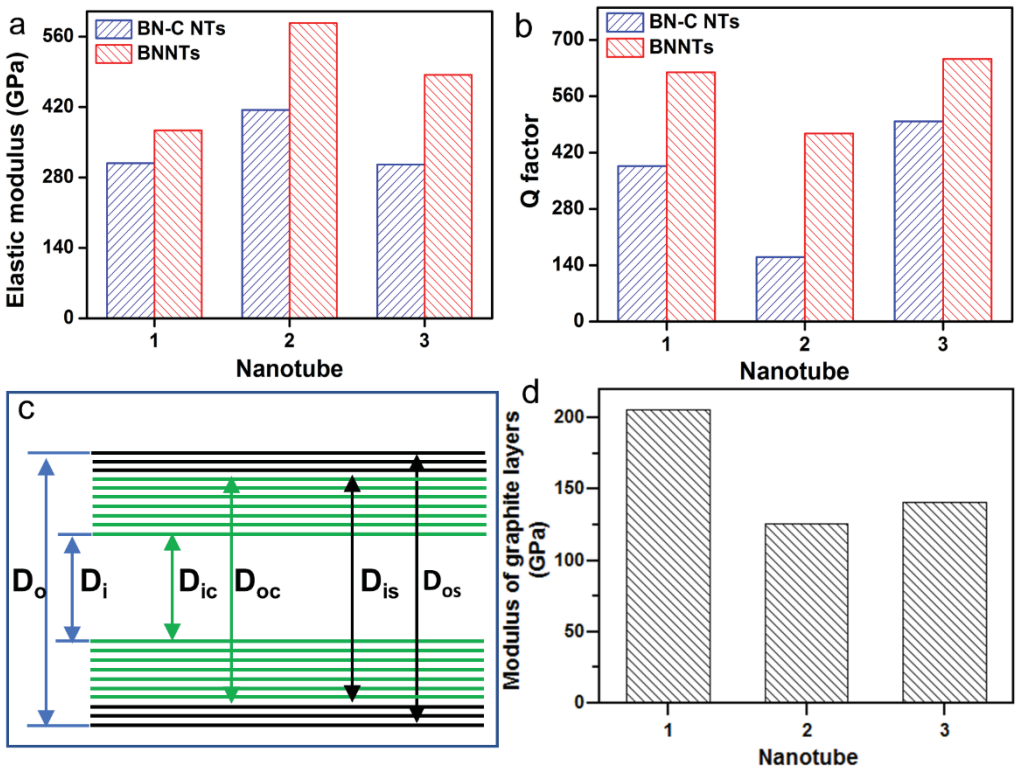

Figure 4.8 (a) and (b) Elastic modulus and Q factors of three individual nanotubes with graphite layers coated and removed, respectively. (c) Schematic illustration of the core-shell composite nanotube model. (d) Elastic modulus of the coated graphite layers by using the core-shell model.

4.4.4 Transport properties of BN-C heterostructures

Electrical property measurements of BN-C nanotubes were then performed using the same *in situ* TEM specimen holder. In order to understand the electrical behavior modulation of BNNTs as a function of the amount of coated C, 20 individual BN-C nanotubes were measured. Representative *I-V* curves acquired from different nanotubes exhibited almost symmetric semiconducting or Ohmic characteristics while the wrapped C content varied (**Figure 4.9a**). By fitting the experimental *I-V* curves and taking into account the geometrical parameters of each nanotube, we can determine the way in which the relative C content influences the composite nanotube transport properties, as shown in **Figure 4.9b**. The resistivity is calculated by considering the total cross-section of the tube, which yields an "effective resistivity". Semiconducting nanotubes can be modeled as a metal-semiconductor-metal structure, with two Schottky barriers and a resistor in between these barriers. At low bias, a reverse Schottky barrier dominates. At higher bias, the nanotube will dominate and its resistance can be accurately calculated.[25] Thus, a bias range from 0.8V to 1V was used to calculate the effective resistivities for these kinds of BN-C nanotubes. In contrast, for Ohmic nanotubes, low bias values were used in order to avoid possible structure damage (**Figure 4.10**) and so their effective resistivities were calculated using the ±0.1 V range. The plot in **Figure 4.9b** allows us to make two important conclusions. First

and most important is the fact that the electrical properties can be tuned over a wide range of effective resistivity values – almost three orders of magnitude – from ~0.16 Ω·m to ~2.5×10^{-4} Ω·m. Secondly, the evolution of the plot can be divided into two distinct regions: a sharp decrease until an C/(B+N+C) atomic ratio of approximately 0.29, followed by a relatively stable region above this number.

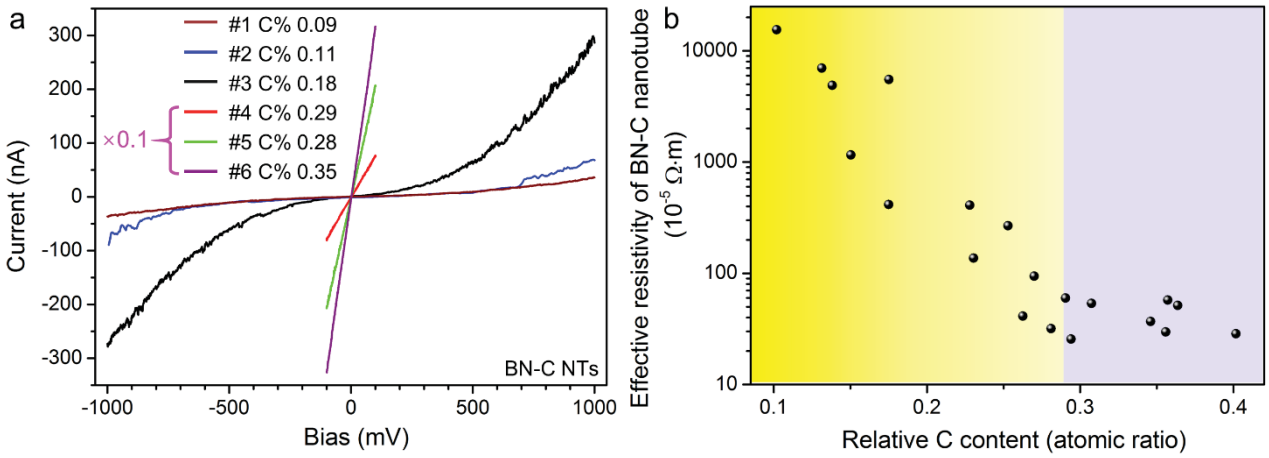

Figure 4.9 (a) Representative *I-V* curves of various individual BN-C nanotubes with different amounts of coated C (averaged values over the whole structures) and (b) relationship between effective resistivity and relative C content for individual BN-C nanotubes. Colored zones represent the areas where the surface graphitic domains are gradually forming and evolving (yellow), and where the formation of an external continuous graphitic shell has ultimately been achieved (purple).

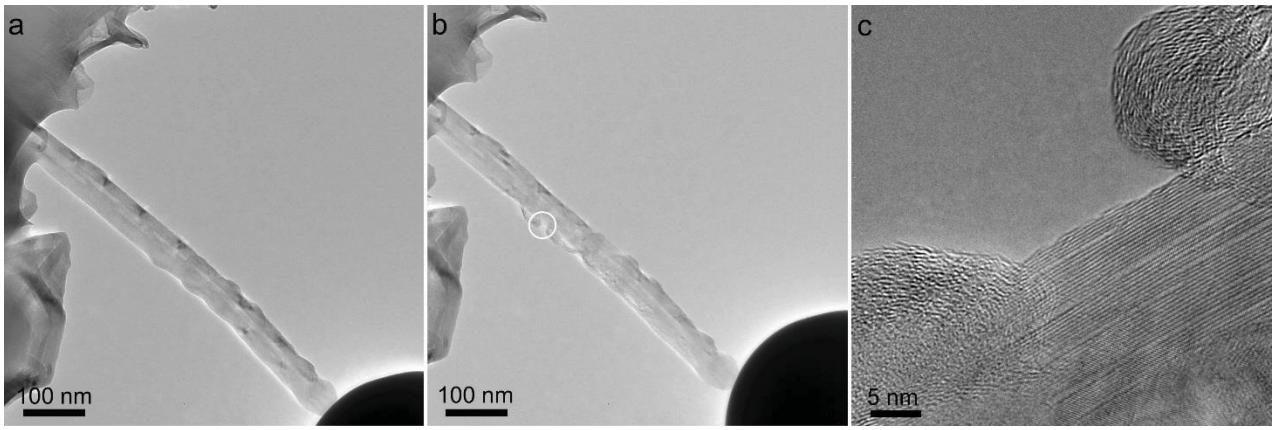

Figure 4.10 (a) TEM image of a BN-C nanotube without bias applied. (b) and (c) TEM and HRTEM image of the same nanotube showing that the external C nanotube layers were damaged and "onion"-like C structures were formed on the BN surface after applying a high bias (10 V).

4.4.5 Effects of carbon coating on transport properties

While the unusual dependency of the electrical resistivity with a relative C content cannot be modeled using this standard core-shell approach. As a result, we have adopted a much more realistic model which takes into account the possible imperfections in the coverage of the tubes by considering that graphitic sections may form discrete island-like structures. This is supported by the details of our growth process. In fact, it is widely

accepted that a CVD process first results in random islands that crystallize and gradually evolve into a continuous network pattern. Electrically, the sharp decrease followed by almost stable resistivity part of the plot is well explained by this 'island growth' model. (**Figure 4.11a**) When the amount of graphitic grains is very small, they form discontinuous and small islands, (**Figure 4.11b**) whose boundaries serve as large potential barriers for electron transport resulting in large resistivity (the extreme case would be a pure BNNT, a good insulator).With the C content increasing, the separation between islands is reduced and the interconnected island network is gradually formed. (**Figure 4.11c**) Consequently, the electron hopping probability from one island to another increases rapidly, thereby leading to the sharp resistivity decrease. With a further increase in the C content a continuous graphite layer is formed. (**Figure 4.11d**) Additional layers provide diminishing contributions to the resistivity, which converges towards a small value. Similar arguments can be considered for mechanical properties. The measurements were mostly performed on nanotubes that had a relative C content of less than 0.29. According to the electrical results, these nanotubes may not be covered by a continuous graphitic shell. As a result, carbon present on these tubes just adds mass, without the benefit of increasing stiffness, leading to a decrease in tube elastic modulus, as observed.

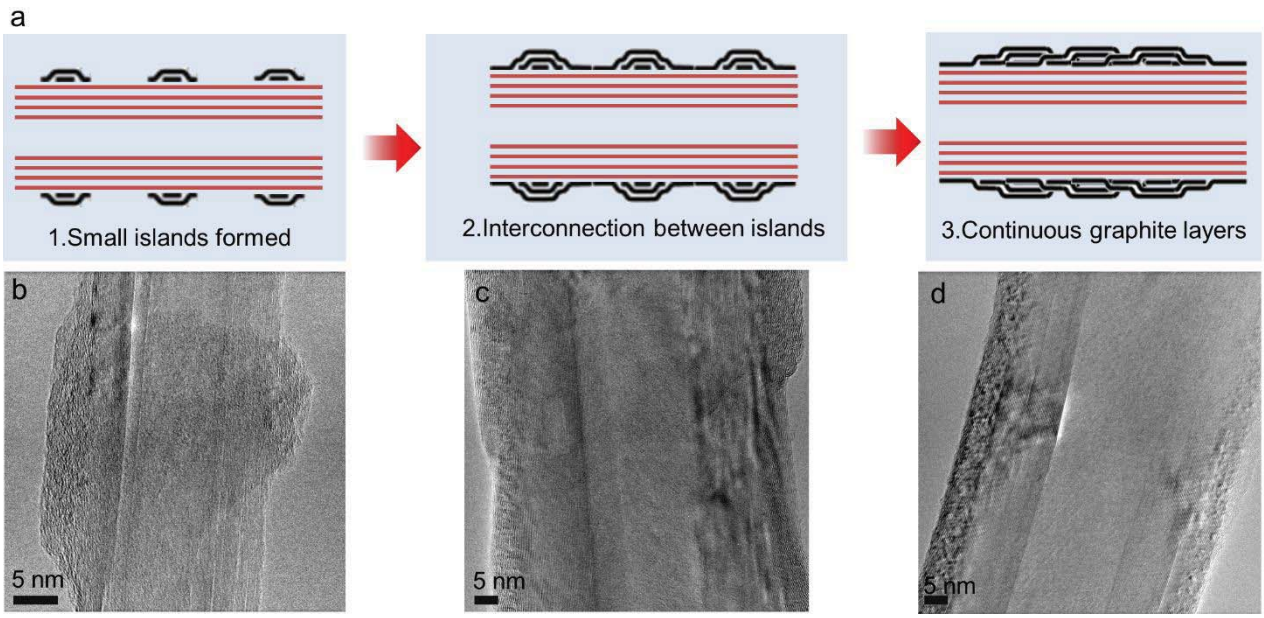

Figure 4.11 (a) Schmatic illustation of the graphite layers foramtion, from small islands to continuous layers. (b-d) TEM images showing the growth of graphite islands, connection of these islands and finally continous layers, respectively.

In order to experimentally test the above-discussed hypothesis, a series of EEL spectra and *I-V* curves were acquired at different contact points along individual nanotubes, as shown in **Figure 4.12**. **Figure 4.12a** and **b** show the TEM images of the nanotube under different contact conditions and the corresponding EEL spectra. The C coverage varies along the tube and in some parts the C signal is missing, implying discontinuous graphitic C islands are formed under small C coverage condition. Such uneven C distribution affects the transport properties of the BN-C nanotube, as indicated in **Figure 4.12c** and **d**. As the contact position moves closer to the counter-contact (Au support), the shapes of the *I-V* curves gradually changed from non-linear to

nearly linear and the resistance decreased exponentially from 1.45×10^5 kΩ to 220 kΩ. Such a dependence of resistance on the length is fully in agreement with the island model. A similar experiment performed on another BN-C nanotube with a higher C coated content, showed purely conductive behavior throughout the structure (**Figure 4.13**). This means that a continuous graphitic outer shell was formed in the latter case. From these experimental results, it can be seen that the coverage of graphitic C varies in each individual BN-C nanotube and indeed affects the electrical properties of the BN-C heterostructure, *i.e.* from a hopping mechanism dominated to a continuous ohmic transport behaviors, which is consistent with our previous results and with our model.

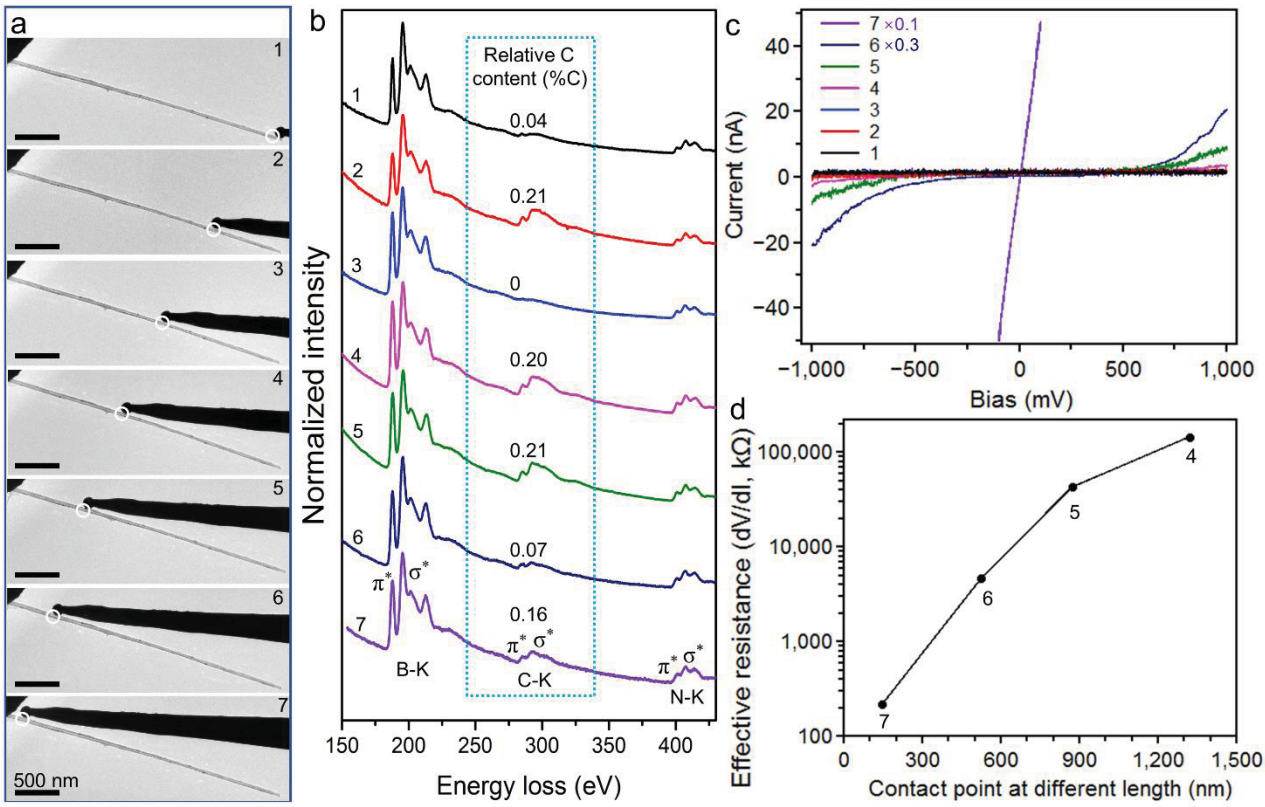

Figure 4.12 (a) TEM images showing consecutive contact points on an individual BN-C nanotube. (b) EEL spectra acquired from the marked regions in (a) revealing the variations in C content in these areas. (c) Recorded *I-V* curves corresponding to each of the points in (a). (d) Electrical resistance values calculated for some of the contact points in (a).

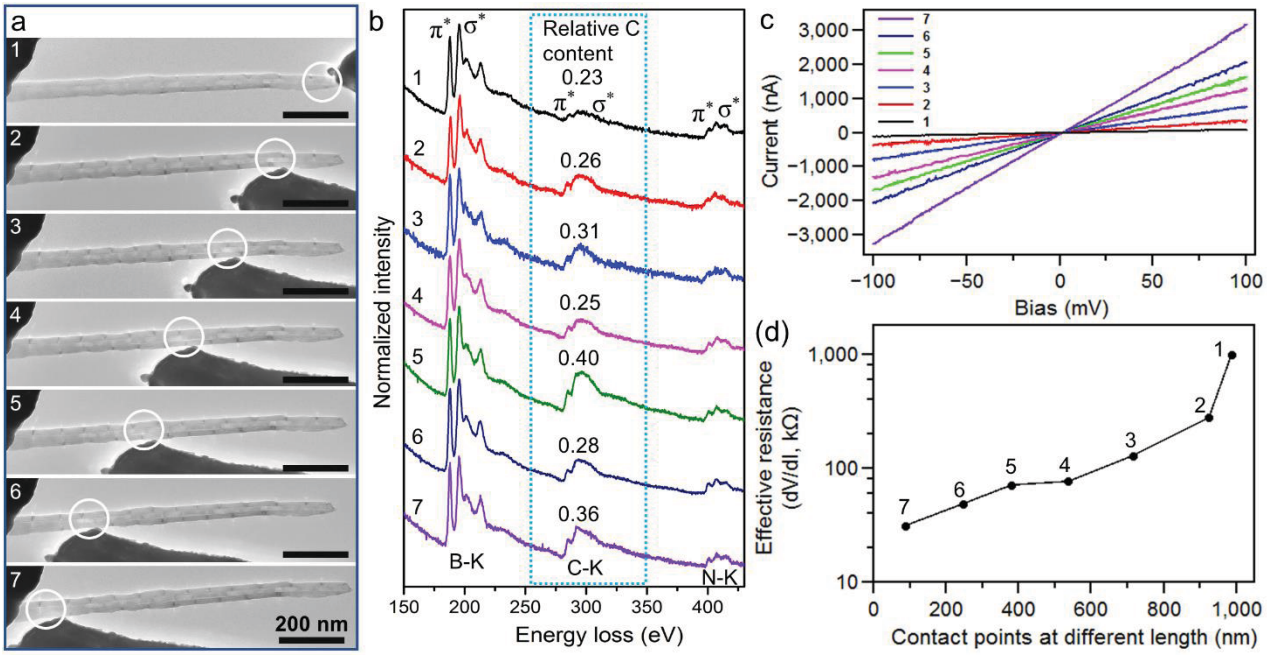

Figure 4.13 (a) TEM images showing consecutive contact points on an individual BN-C nanotube. (b) EEL spectra acquired from the marked regions in (a) revealing the variations in C content in these areas. (c) Recorded *I-V* curves corresponding to each of the points in (a). (d) Electrical resistance values corresponding to each of the contacts in (a).

4.4.6 Advantages of BN-C heterostructures

The mechanical and electrical properties of the present materials were finally plotted and compared to those from previous reports in **Figure 4.14**. Comparing to the high elastic modulus and opposed electrical properties of BNNTs and CNTs, the present BN-C hybrid nanotubes inherit the advantages of each component, while allowing for a wide range modulation of both mechanical and electrical behaviors at the same time. Two other materials with similar 1D morphologies were also compared, *i.e.* metal nanowires (conductors) and intrinsic Si nanowires (semiconductors). Although the elastic moduli show a wide distribution for metal nanowires as a whole, their properties are almost constant for individual elements. Similar arguments can be considered concerning the elastic moduli of intrinsic Si nanowires, which have a narrow range. By adjusting the volume of the wrapped C content, the present BN-C heterostructures can be tuned to cover a wide range of values, both electrically and mechanically, making the present heterostructured BN-C nanotubes readily applicable in different fields.

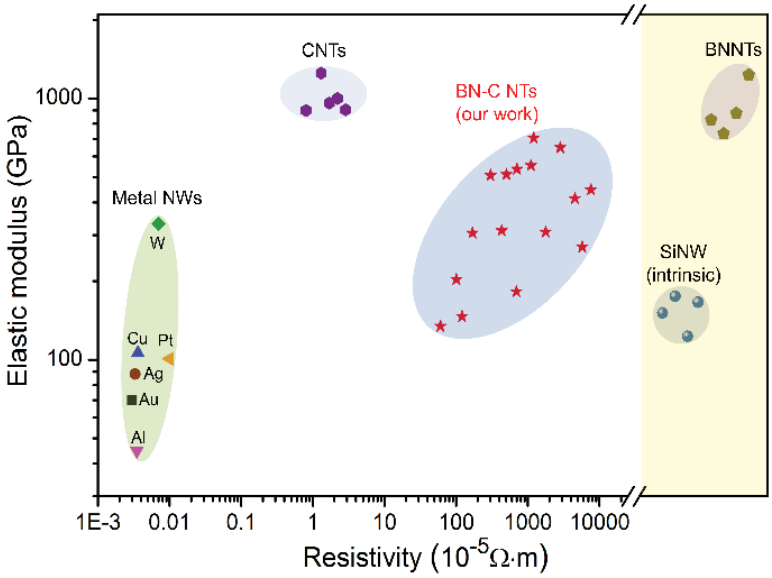

Figure 4.14 Comparison of the present data with the previous reports on different materials (Au, [27,28] Ag, [29,30] Cu, [31] Al, [32,33] Pt, [34,35] and W [36,37] nanowires, CNTs, [17,38–44]BNNTs [45–48] and SiNW[49–52]) in terms of elastic moduli and electrical resistivities at room temperature (different characteristic regions are marked).

4.5 Summary

To sum up, an original way was developed to efficiently tune the properties of core-shell composite C-coated BN nanotubes by adjusting the relative C contents. Rather than limiting ourselves to the individual characteristics of individual C and BN nanomaterials, we have proposed a way to control both the mechanical and electrical behaviors of BN-C hybrids to a large extent. We obtained the composite BN-C nanotubes with elastic moduli ranged from ~140 GPa to 706 GPa and electrical resistivities ranged from ~0.16 Ω·m to ~2.5×10^{-4} Ω·m. The current work is envisaged to provide a promising way to fine-tune mechanical and electrical properties in the binary BN-C nanotube system.

4.6 References

(1) Jorio, A.; Dresselhaus, G.; Dresselhaus, M. S. Carbon Nanotubes - Synthesis, Structure, Properties and Applications. *Springer, Verlag Berlin Heidelberg, Germany*, **2007**. 3-80.

(2) Wildöer, J. W. G.; Venema, L. C.; Rinzler, A. G.; Smalley, R. E.; Dekker, C. Electronic Structure of Atomically Resolved Carbon Nanotubes. *Nature* **1998**, *391*, 59–62.

(3) Rubio, A.; Corkill, J. L.; Cohen, M. L. Theory of Graphitic Boron Nitride Nanotubes. *Phys. Rev. B* **1994**, *49* (7), 5081–5084.

(4) Ayala, P.; Arenal, R.; Loiseau, A.; Rubio, A.; Pichler, T. The Physical and Chemical Properties of Heteronanotubes. *Rev. Mod. Phys.* **2010**, *82*, 1843–1885.

(5) Wei, X.; Wang, M. S.; Bando, Y.; Golberg, D. Post-Synthesis Carbon Doping of Individual Multiwalled Boron Nitride Nanotubes *via* Electron-Beam Irradiation. *J. Am. Chem. Soc.* **2010**, *132*, 13592–13593.

(6) Wang, W.; Bando, Y.; Zhi, C.; Fu, W.; Wang, E.; Golberg, D. Aqueous Noncovalent Functionalization and Controlled Near-Surface Carbon Doping of Multiwalled Boron Nitride Nanotubes. *J. Am. Chem. Soc.* **2008**, *130*, 8144–8145.

(7) Zhang, B.; Zhao, L.; Cheng, Y.; Golberg, D.; Wang, M. S. Reversible Tuning of Individual Carbon Nanotube Mechanical Properties *via* Defect Engineering. *Nano Lett.* **2016**, *16* (8), 5221–5227.

(8) Wang, Z. L.; Dai, Z. R.; Gao, R. P.; Gole, J. L. Measuring the Young's Modulus of Solid Nanowires by *in Situ* TEM. *J. Electron Microsc.* **2002**, *51* (90001), 79S – 85.

(9) Xu, F.; Qin, Q.; Mishra, A.; Gu, Y.; Zhu, Y. Mechanical Properties of Zno Nanowires under Different Loading Modes. *Nano Res.* **2010**, *3* (4), 271–280.

(10) Pickering, E.; Bo, A.; Zhan, H.; Liao, X.; Tan, H. H.; Gu, Y. *In Situ* Mechanical Resonance Behaviour of Pristine and Defective Zinc Blende GaAs Nanowires. *Nanoscale* **2018**, *10* (5), 2588–2595.

(11) Ni, H.; Li, X. Young's Modulus of ZnO Nanobelts Measured Using Atomic Force Microscopy and Nanoindentation Techniques. *Nanotechnology* **2006**, *17* (14), 3591–3597.

(12) Namazu, T.; Isono, Y.; Tanaka, T. Evaluation of Size Effect on Mechanical Properties of Single Crystal Silicon by Nanoscale Bending Test Using AFM. *J. Microelectromechanical Syst.* **2000**, *9* (4), 450–459.

(13) Ferreira, P. J.; Mitsuishi, K.; Stach, E. A. *In Situ* Transmission Electron Microscopy. *MRS Bulletin* **2008**, *33*, 83–90.

(14) Luo, C.; Wang, C.; Wu, X.; Zhang, J.; Chu, J. *In Situ* Transmission Electron Microscopy Characterization and Manipulation of Two-Dimensional Layered Materials beyond Graphene. *Small* **2017**, *13*, 1–18.

(15) Espinosa, H. D.; Bernal, R. A.; Filleter, T. *In Situ* TEM Electromechanical Testing of Nanowires and Nanotubes. *Small* **2012**, 8, 191–226.

(16) Tang, D.; Ren, C.; Wei, X.; Wang, M.; Liu, C.; Bando, Y. Mechanical Properties of Bamboo-like Boron Nitride Nanotubes by *In Situ* TEM and MD Simulations: Strengthening Effect of Interlocked Joint Interfaces. *Nano Lett.* **2011**, *5*, 7362–7368.

(17) Treacy, M. M. J.; Ebbesen, T. W.; Gibson, J. M. Exceptionally High Young's Modulus Observed for Individual Carbon Nanotubes. *Nature* **1996**, *381*,678–680.

(18) Li, X.; Wei, X.; Xu, T.; Pan, D.; Zhao, J.; Chen, Q. Remarkable and Crystal-Structure-Dependent Piezoelectric and Piezoresistive Effects of InAs Nanowires. *Adv. Mater.* **2015**, *27*, 2852–2858.

(19) Zhang, C.; Tian, W.; Xu, Z.; Wang, X.; Liu, J.; Li, S. L.; Tang, D. M.; Liu, D.; Liao, M.; Bando, Y.; Golberg, D. Photosensing Performance of Branched CdS/ZnO Heterostructures as Revealed by *In Situ* TEM and Photodetector Tests. *Nanoscale* **2014**, *6*, 8084–8090.

(20) Tang, C.; Bando, Y.; Sato, T.; Kurashima, K. A Novel Precursor for Synthesis of Pure Boron Nitride

Nanotubes. *Chem. Commun.* **2002**, *2*, 1290–1291.

(21) Song, Y.; Li, B.; Yang, S.; Ding, G.; Zhang, C.; Xie, X. Ultralight Boron Nitride Aerogels *via* Template-Assisted Chemical Vapor Deposition. *Sci. Rep.* **2015**, *5*, 1–9.

(22) Rebelo, S. L. H.; Guedes, A.; Szefczyk, M. E.; Pereira, A. M.; Araújo, J. P.; Freire, C. Progress in the Raman Spectra Analysis of Covalently Functionalized Multiwalled Carbon Nanotubes: Unraveling Disorder in Graphitic Materials. *Phys. Chem. Chem. Phys.* **2016**, *18* (18), 12784–12796.

(23) Gupta, T. K.; Singh, B. P.; Mathur, R. B.; Dhakate, S. R. Multi-Walled Carbon Nanotube-Graphene-Polyaniline Multiphase Nanocomposite with Superior Electromagnetic Shielding Effectiveness. *Nanoscale* **2014**, *6* (2), 842–851.

(24) Zhi, C.; Bando, Y.; Tan, C.; Golberg, D. Effective Precursor for High Yield Synthesis of Pure BN Nanotubes. *Solid State Commun.* **2005**, *135*, 67–70.

(25) Xue, Y.; Dai, P.; Zhou, M.; Wang, X.; Pakdel, A.; Zhang, C.; Weng, Q.; Takei, T.; Fu, X.; Popov, Z. I.; Sorokin, P. B.; Tang, C. C.; Shimamura, K.; Bando, Y.; Golberg, D. Multifunctional Superelastic Foam-Like Boron Nitride Nanotubular Cellular-Network Architectures. *ACS Nano* **2017**, *11*, 558–568.

(26) Kim, S. Y.; Park, J.; Choi, H. C.; Ahn, J. P.; Hou, J. Q.; Kang, H. S. X-Ray Photoelectron Spectroscopy and First Principles Calculation of BCN Nanotubes. *J. Am. Chem. Soc.* **2007**, *129*, 1705–1716.

(27) Wu, B.; Heidelberg, A.; Boland, J. J. Mechanical Properties of Ultrahigh-Strength Gold Nanowires. *Nat. Mater.* **2005**, *4* (7), 525–529.

(28) Critchley, K.; Khanal, B. P.; Górzny, M. L.; Vigderman, L.; Evans, S. D.; Zubarev, E. R.; Kotov, N. A. Near-Bulk Conductivity of Gold Nanowires as Nanoscale Interconnects and the Role of Atomically Smooth Interface. *Adv. Mater.* **2010**, *22* (21), 2338–2342.

(29) Cheng, Z.; Liu, L.; Xu, S.; Lu, M.; Wang, X. Temperature Dependence of Electrical and Thermal Conduction in Single Silver Nanowire. *Sci. Rep.* **2015**, *5*. 1-12.

(30) Li, X.; Gao, H.; Murphy, C. J.; Caswell, K. K. Nanoindentation of Silver Nanowires. *Nano Lett.* **2003**, *3*, 1495–1498.

(31) Xu, W. H.; Wang, L.; Guo, Z.; Chen, X.; Liu, J.; Huang, X. J. Copper Nanowires as Nanoscale Interconnects: Their Stability, Electrical Transport, and Mechanical Properties. *ACS Nano* **2015**, *9*, 241–250.

(32) Liu, Y. L.; Shao, D. K.; Zeng, Y. T.; Wang, W. K.; Lu, M. Q. Molecular Dynamics Study of the Tensile Deformation on Aluminum Nanorod. *Adv. Intell. Syst. Res.* **2016**, *136*, 139–146.

(33) Lee, J. W.; Kang, M. G.; Kim, B. S.; Hong, B. H.; Whang, D.; Hwang, S. W. Single Crystalline Aluminum Nanowires with Ideal Resistivity. *Scr. Mater.* **2010**, *63*, 1009–1012.

(34) Koh, S. J. A.; Lee, H. P.; Lu, C.; Cheng, Q. H. Molecular Dynamics Simulation of a Solid Platinum

Nanowire under Uniaxial Tensile Strain: Temperature and Strain-Rate Effects. *Phys. Rev. B - Condens. Matter Mater. Phys.* **2005**, *72*, 1–11.

(35) Lide, D. R. CRC Handbook of Chemistry and Physics, *CRC Press*, Boca Raton, FL, **2005**, 22-106.

(36) Choi, D.; Moneck, M.; Liu, X.; Oh, S. J.; Kagan, C. R.; Coffey, K. R.; Barmak, K. Crystallographic Anisotropy of the Resistivity Size Effect in Single Crystal Tungsten Nanowires. *Sci. Rep.* **2013**, *3*, 1–4.

(37) Hassel, A. W.; Cimalla, V.; Röhlig, C. C.; Pezoldt, J.; Niebelschütz, M.; Ambacher, O.; Brückner, K.; Hein, M.; Weber, J.; Milenkovic, S.; Smith, A. J.; Hassel, A. W. Nanomechanics of Single Crystalline Tungsten Nanowires. *J. Nanomater.* **2008**, *2008*, 1-9.

(38) Poncharal, P.; Wang, Z. L.; Ugarte, D.; Heer, W. A. Electrostatic Deflections and Electromechanical Resonanses of Carbon Nanotubes. *Science* **1999**, *283*, 1513-1516.

(39) Demczyk, B. G.; Wang, Y. M.; Cumings, J.; Hetman, M.; Han, W.; Zettl, A.; Ritchie, R. O. Direct Mechanical Measurement of the Tensile Strength and Elastic Modulus of Multiwalled Carbon Nanotubes. *Mater. Sci. Eng. A* **2002**, *334* (1–2), 173–178.

(40) Ebbesen, T. W. ; Lezec H. J.; Hiura H.; Bennett J. W.; Ghaemi, H. F.; Thio. T. Electrical Conductivity of Individual Carbon Nanotubes. *Nature* **1996**, *382*,54–56.

(41) Kasumov, A. Y.; Khodos, I. I.; Ajayan, P. M.; Colliex, C. Electrical Resistance of a Single Carbon Nanotube. *Europhys. Lett.* **1996**, *34* (6), 429–434.

(42) Wong, E. W.; Sheehan, P. E.; Lieber, C. M.; Iqbal, B. Q.; Barisci, R.; Spinks, P. M.; Nanobeam Mechanics: Elasticity, Strength, and Toughness of Nanorods and Nanotubes. *Science* **1997**, *277*, 1971–1975.

(43) Santosh, M.; Maiti, P.; Sood, A. K. Elastic Properties of Boron Nitride Nanotubes and Their Comparison with Carbon Nanotubes. *J. Nanosci. Nanotechnol.* **2009**, *9* (9), 5425–5430.

(44) Yu, M.-F.; Files, B. S.; Arepalli, S.; Ruoff, R. S. Tensile Loading of Ropes of Single Wall Carbon Nanotubes and Their Mechanical Properties. *Phys. Rev. Lett.* **2000**, *84*, 5552–5555.

(45) Suryavanshi, A. P.; Yu, M. F.; Wen, J.; Tang, C.; Bando, Y. Elastic Modulus and Resonance Behavior of Boron Nitride Nanotubes. *Appl. Phys. Lett.* **2004**, *84*, 2527–2529.

(46) Chopra, N. G.; Zettl, A. Measurement of The Elastic Modulus of A Multi-walled Boron Nitride Nanotubes. *Solid State Commun.* **1998**, *105 (5)*, 297–300.

(47) Wei, X.; Wang, M. S.; Bando, Y.; Golberg, D. Tensile Tests on Individual Multi-Walled Boron Nitride Nanotubes. *Adv. Mater.* **2010**, *22*, 4895–4899.

(48) Arenal, R.; Wang, M. S.; Xu, Z.; Loiseau, A.; Golberg, D. Young Modulus, Mechanical and Electrical Properties of Isolated Individual and Bundled Single-Walled Boron Nitride Nanotubes.

Nanotechnology **2011**, *22* (26), 1-7.

(49) Zhang, H.; Tersoff, J.; Xu, S.; Chen, H.; Zhang, Q.; Zhang, K.; Yang, Y.; Lee, C. S.; Tu, K. N.; Li, J.; Lu, Y. Approaching the Ideal Elastic Strain Limit in Silicon Nanowires. *Sci. Adv.* **2016**, *2*, 2–10.

(50) Hsin, C. L.; Mai, W.; Gu, Y.; Gao, Y.; Huang, C. Te; Liu, Y.; Chen, L. J.; Wang, Z. L. Elastic Properties and Buckling of Silicon Nanowires. *Adv. Mater.* **2008**, *20*, 3919–3923.

(51) Röhlig, C. C.; Niebelschütz, M.; Brueckner, K.; Tonisch, K.; Ambacher, O.; Cimalla, V. Elastic Properties of Nanowires. *Phys. Status Solidi Basic Res.* **2010**, *247*, 2557–2570.

(52) Zhu, Y.; Xu, F.; Qin, Q.; Fung, W. Y.; Lu, W. Mechanical Properties of Vapor−Liquid−Solid Synthesized Silicon Nanowires. *Nano Lett.* **2009**, *9*, 3934–3939.

Chapter 5

Kinking effects and transport properties of coaxial BN-C nanotubes as revealed by *in situ* transmission electron microscopy and theoretical analysis

5.1 Introduction

Over the last several years, flexible devices have attracted tremendous attention due to various potential applications in electronic devices, sensor chips, and photodetectors.[1-3] Thus, the mechanical elasticity, structural changes and electrical transport of the constituting materials under cycling bending are of crucial importance with respect to reliable practical applications. Boron nitride nanotubes (BNNTs) and carbon nanotubes (CNTs) have intensively been studied and are currently regarded as materials of choice for many structural applications; they reveal extremely high Young's moduli, high fracture strength, and excellent flexibility.[4-8] By contrast, they have just the opposite electrical characteristics, *i.e.* BNNTs are insulators,[9,10] whereas CNTs are metals or semiconductors depending on tubes' helicity.[11,12] It worth noting that BNNT electrical properties are rather difficult to tune. This fact results in blocking their possible applications in flexible stress sensors or switches. Thus, it is of great interest and challenge to modify BNNT electrical response and create nanostructures having a tunable percolation threshold and to facilitate their applications in flexible electronics. Actually to date, both theoretically and experimentally, tremendous efforts have already been put to modulate the transport behaviors of BNNTs, using doping,[13] strain engineering,[14] heterostructure design,[15] structure unwrapping,[16,17,] *etc*. Another prospective approach is to fabricate BN-C heterostructures, usually regarded as nanoscale "Lego" blocks, and provide the engineers with diverse possibilities for tuning properties and promoting advanced applications.[18] For instance, Xiang *et al.* have reported on a design of BN/C Van der Waals heterostructures, showing the similar transport behavior to bare CNTs, but much better thermal stabilities of the material.[19] Lin *et al.* developed the C@BN nanotube arrays and revealed the enhanced shape recovery and improved compressive strength. These reports clearly demonstrate the interesting potentials of BN-C related composites.[20]

Herein, we have designed and synthesized core-shell coaxial BN-C nanotubes and applied an *in situ* transmission electron microscopy (TEM) technique to study their transport characteristics and the effects of external bending deformation on their structural evolution and electrical transport. Ballistic transport within the tube contact lengths of ~250 nm, diffusive transport within the lengths ranging from 250 nm to 750 nm; and the hopping transport for the larger lengths have been documented. When a bending deformation has been applied, all these three transport modes are not notably affected while a peculiar kinking deformation is observed. It has been found that the kink positions are strictly related to the structural nanotube parameter, *i.e.* a ratio between the tube diameter and its length. Interestingly, after deformation, BN-C nanotubes have fully recovered, even after very high angles of bending, without any traces of failure or structural defects appearance, showing excellent electrical and structural stability. Combination of *in situ* TEM and molecular dynamic (MD) simulations has then provided us with an effective way to uncover the transport and mechanical behaviors of composite BN-C nanotubes and paved the way toward their realistic and smart applications in flexible electronics.

5.2 Methods

5.2.1 Materials synthesis and characterization

Tubular BN-C heterostructures were synthesized *via* a three-step chemical vapor deposition (CVD) method, which is described in our previous work in detail.[29,30] TEM imaging and electron energy loss spectra (EELS) mapping of individual BN-C nanotubes were performed using a JEOL 3000F TEM, by using an *in situ* heating holder to alleviate/avoid the possible contamination during the scanning process.

5.2.2 *In situ* TEM experiments

In situ bending experiments on individual coaxial BN-C nanotubes were performed inside a JEOL 3100FEF (Omega filter) TEM by using a scanning tunneling microscopy-TEM holder (Nanofactory Instruments AB). Hybrid BN-C nanotubes were firmly attached to the edge of a flat Au wire using conductive silver epoxy, and a freshly electrochemically etched W probe was used as the counter electrode. The W probe was controlled by a piezo-motor to contact the selected nanotube and to record the current-voltage (*I-V*) curves. Bending deformation of the BN-C nanotubes was initiated by moving the W probe forward (after the two sides of the setup had physically contacted each other), thus the bending angles could be traced and precisely measured at every stage of deformation.

5.2.3 Computational details

To describe the features of a possibly polygonal cross-section of hybrid coaxial BN-C nanotubes and to further study the atomic structure of CNT layers wrapped around a BNNT core, a newly developed potential of interlayer interaction based on ReaxFF was used.[31,32] This potential contains three terms describing the interlayer attraction due to dispersive interactions, repulsion due to anisotropic overlaps of electron clouds, and, also, monopolar electrostatic interactions. Simulations of the bending process were carried out by means

of molecular dynamics calculations based on the program software LAMMPS.[33] We simulated hybrid BN-C nanotubes with various diameters, lengths, and the ratios between the number of C and BN layers. Bending of hybrid coaxial nanotubes was modelled *via* interaction with an atomic force microscopy tip which pushed the structure with a step of ~1.4 Å. Interactions between the tube and the simulated tip were described with a purely repulsive force. Before the mechanical test and at each bending step, the system was annealed at a temperature decreasing from 300 to 10 K, while the maximum interatomic forces became less or equal to 0.05 eV/Å. Annealing time at each step was chosen as 3.5 ps with the time step of 10^{-3} fs. Atomic structure of considered hybrid nanotubes contained 5×10^4 to 6×10^5 atoms in total. The atomic interactions between B and N atoms in a BNNT were described by the Tersoff 3-body potential implemented in LAMMPS.[34,35] Redistribution of electronic density on the kink area of hybrid BN-C nanotubes was calculated using Density Functional Theory (DFT) within LCAO (DZP basis set) approximation, implemented in SIESTA software.[36] Due to a large number of atoms containing in the kink area of a hybrid BN-C nanotube (more than 2000) energy mesh cutoff was set as 125 Ry, which is enough for a quantitative description of electronic properties of large structures. To obtain the information on electron density redistribution between the hybrid nanotube walls only electronic structure optimization was carried out using DFT, while ion relaxation was performed under MD approximation, as described earlier in this section.

5.3 Results and discussion

5.3.1 Structure characterization

Coaxial BN-C hybrid nanotubes were synthesized *via* a three-step high-temperature process. Firstly, pure BNNTs were prepared by boron and metal oxide-assisted chemical vapor depostion (BOCVD) method in an induction furnace, followed by a high temperture purification process at 1800 ºC. Subsequently, carbon coating was deposited on tubes *via* a CVD method by using hexane as a carbon source and Ar as a carrier gas. This process was conduced in a horizontal electrical furnace under ambient pressure, at 1100 ºC for 60 s. Finally, the carbon-coated BNNT samples were annealed at 1800 ºC for 6 h to induce complete graphitization and to remove possible impurities.[29,30] A typical TEM image, shown in **Figure 5.1a**, reveals a hollow one-dimensional structure which perfectly maintains its structural integrity even after the employed high-temperature synthesis. The corresponding HRTEM image of the tube walls is depicted in **Figure 5.1b**. The distance between the adjacent tubular layers is ~0.33 nm over the whole structure, implying its excellent crystallinity. Electron energy loss spectroscopy (EELS) maps were created to confirm the overall composition and spatial distribution of the constituting elements. **Figure 5.1c** depicts an annular dark field (ADF) scanning TEM (STEM) image of segment from a different nanotube, and **Figure 5.1d-f** presents the corresponding elemental spatially-resolved EELS maps for constituting elements. EELS mapping unambiguously confirms the coexistence of B, N, and C species within the nanotube walls. It is worth noting that the C signal becomes more intense on the tube periphery, suggesting that C layers form the outer shells. This is further confirmed by the EEL spectra extracted from the different regions in **Figure 5.1c**, as shown in Figure **5.1g**. In regions "1" and "3", only peak at 284 eV originated from C is recognized, while in the middle area "2", three distinct peaks are seen at 188

eV, 284 eV and 401 eV, corresponding to the K-shell ionization edges of B, C, and N, respectively. The peaks reveal sharp π* features and σ* bands and imply typical sp^2 bonding conFigureuration.[21-23] The atomic ratio from the EELS data (region "2") is calculated as B:C:N = 1.00:0.36:0.94. Elemental composition for the core and shell was further verified by comparative EEL spectra analysis on the same nanotube before and after the annealing process. The results showed that only the peaks for B and N remained after thermal treatment, indicating that the core is made of the pure BN (**Figure 5.2**). All these results confirm that as-obtained samples are sandwich-like coaxial BN-C tubular nanostructures.

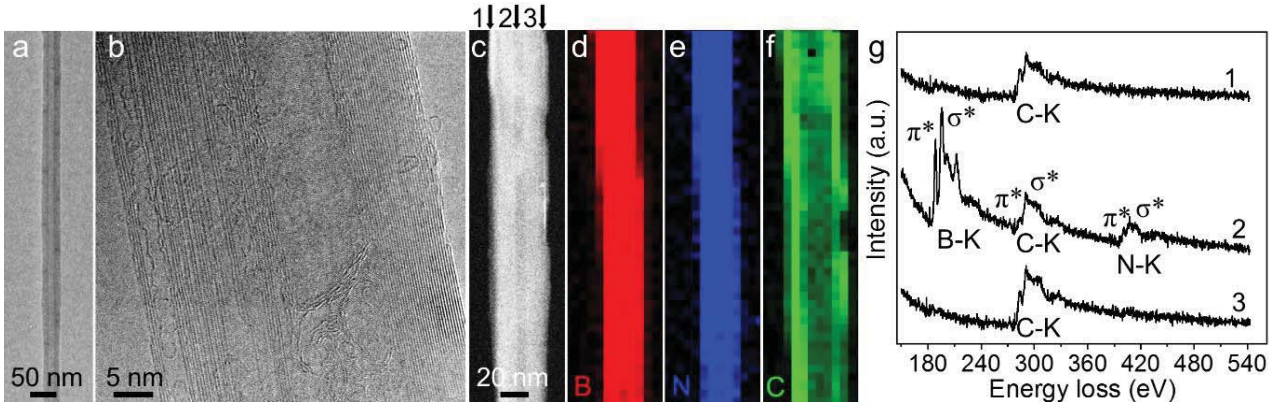

Figure 5.1 Low-magnification TEM (a) and high-resolution TEM image (b) of a core-shell sandwich-like coaxial BN-C nanotube showing perfect crystallinity. (c) ADF-STEM image acquired from a nanotube segment. (d-f) Spatially resolved EELS elemental maps corresponding to the image in (c) revealing B, N, and C species distribution. (g) EEL spectra extracted from the corresponding regions arrowed in (c).

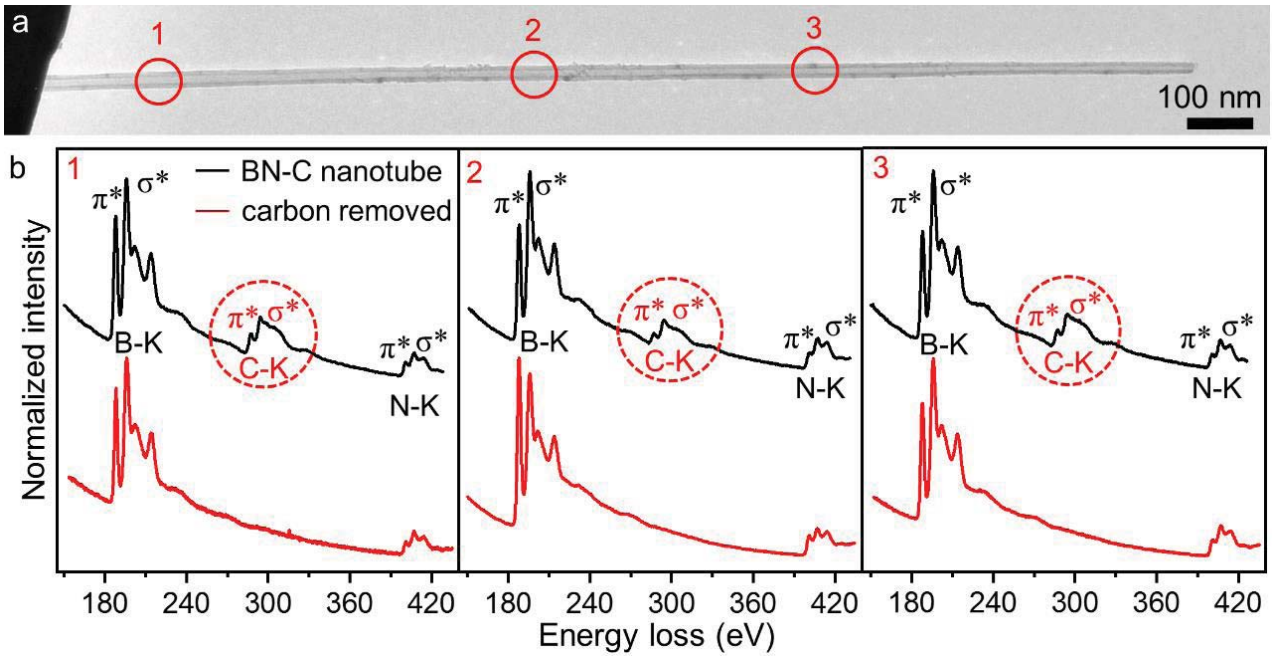

Figure 5.2 (a) TEM image of a nanotube. (b) EEL spectra taken from the red circles marked regions in (a) before and after thermal treatment, showing that only BN peaks remained while the carbon signals disappeared.

5.3.2 Evaluation of contact resistance

For the present two-terminal contact measurements, the total resistance R is the sum of three contributions: R_g, R_w, and R_n, where R_g and R_w are the contact resistances of a nanotube to the gold wire and W probe, respectively. R_g may vary from one BN-C nanotube to another, but it is constant for a selected nanotube, whereas R_w may fluctuate between two individual contact experiments, albeit such fluctuation is rather small. The evaluation of the contact resistance of an individual BN-C nanotube was conducted as follows: (1) the total resistance (R_g+R_w+R_t) was obtained by doing the linear fitting for the I-V curves at different contact lengths. (2) the total resistance as a function of contact length was plotted and the linear fitting for the length range was made, this showed an approximate linear variation trend, then the intercept was considered as the whole contact resistance (R_g+R_w). Here, the contact resistance was evaluated to be 14.2 kΩ (**Figure 5.3a**). In total, we estimated the contact resistance for 5 nanotubes, this ranged from 9.5 kΩ to 17.5 kΩ (**Figure 5.3b**).

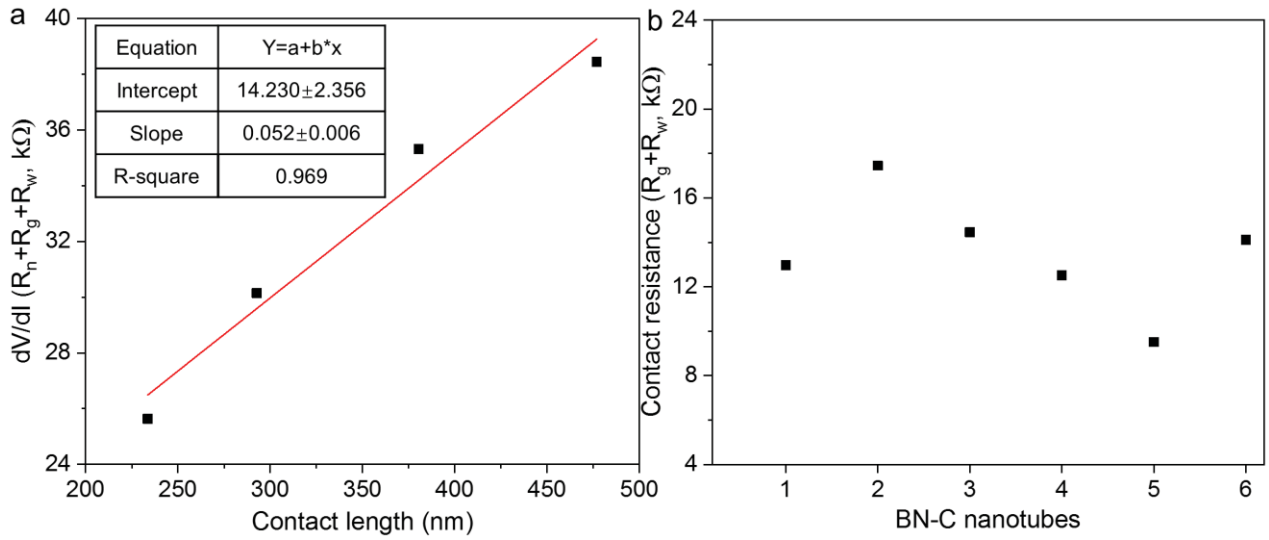

Figure 5.3 (a) The linear fitting for the relationship between the total resistance and the contact length., showing that the contact resistance is about 14.2 kΩ. The total resistance was acquired from the *I-V* curves shown in Figure 5.4c. (b) The contact resistance distribution obtained from 5 individual BN-C nanotubes.

5.3.3 Length-dependent transport properties of BN-C nanotubes

Transport behavior of nanotubes with uniform C coating as a function of tube length was first studied. The schematic of the experimental setup and TEM image showing the measurement process are presented in **Figure 5.4a** and **b**, respectively. Representative *I-V* curves at different contact lengths were recorded by moving the W probe to contact the different segments of the selected BN-C nanotube, as illustrated in **Figure 5.4c**. Clearly, all these *I-V* curves reveal a linear characteristic. However, the current values vary a lot at different contact lengths. Then, we evaluated the resistance of a nanotube (R_n) as a function of the contact length. **Figure 5.4d** presents the evolution of the nanotube resistance along with contact length change as acquired from -100 mV to +100 mV, the value excludes the contact resistances R_g and R_w, ranging from 9.5 kΩ to 17.5 kΩ, as evaluated from different BN-C nanotubes (**Figure 5.3b**). The plot shows that R_n increases sharply from 11.3 kΩ at 90.3 nm, to 1110.3 kΩ at 809.8 nm and displays a nonlinear behavior. Interestingly, combining the enlarged region with contact length smaller than 476.9 nm and considering the whole plot, one may conclude that the

relationship between the tube resistance and the contact length can be divided into three definite areas, *i.e.* (1) resistance values lower than 12.9 kΩ within the contact lengths smaller than 233.7 nm, which can be considered as the ballistic transport (region 1); (2) resistances increasing linearly with the contact lengths, from 292.7 nm to 476.9 nm, corresponding to a diffusive transport[24] (region 2); and (3) resistances increasing exponentially (see the exponential fitting) under further length increasing, up to ~930.4 nm, which can be ascribed to a hopping mechanism.[25] These regions correspond to three different transport regimes. In the case of ballistic transport, carriers easily travel within the length range corresponding to the mean free path *l*. Within this contact length range, the resistances are independent of the contact length. For a single channel medium, the resistance of the ballistic conductor is given as: $R = \frac{h}{2q^2} \approx 12.9\ k\Omega$ (where *h* is the Planck's constant, and *q* is the electron charge). At scales longer than *l*, the electrons will be elastically scattered and the transport becomes diffusive. Within this range, the resistance is linearly dependent on the contact length and can be approximately expressed as: $R \approx \rho \frac{L}{S}$ (where ρ is the resistivity, *L* is the contact length, and *S* is the cross-section area). Our previous work has verified that with longer distances, instead of a uniform coating made of carbon shells, the tubes are covered by small carbon islands. Thus, under further increasing of the contact length, electron hopping from one island to another becomes dominant and the resistance shows an exponential dependence on the length.[30] The observed non-linear dependence of R_n indicates that the electronic transport over the whole tube is not Ohmic and the electron-defect interactions are the main source of resistance, *i.e.* the electrons suffer from the scattering events with defects inside the conductor.[26] *I-V* measurements on different BN-C nanotubes also show the similar resistance *vs* contact length plots, though the ballistic and diffusive transport ranges differ for different BN-C nanotubes (**Figure 5.5**). This fact can be ascribed to different patterns of defect distributions in each particular nanotube. The above experiments imply that the nonlinear resistance *vs* contact length is a common intrinsic phenomenon for the present coaxial BN-C nanotubes.

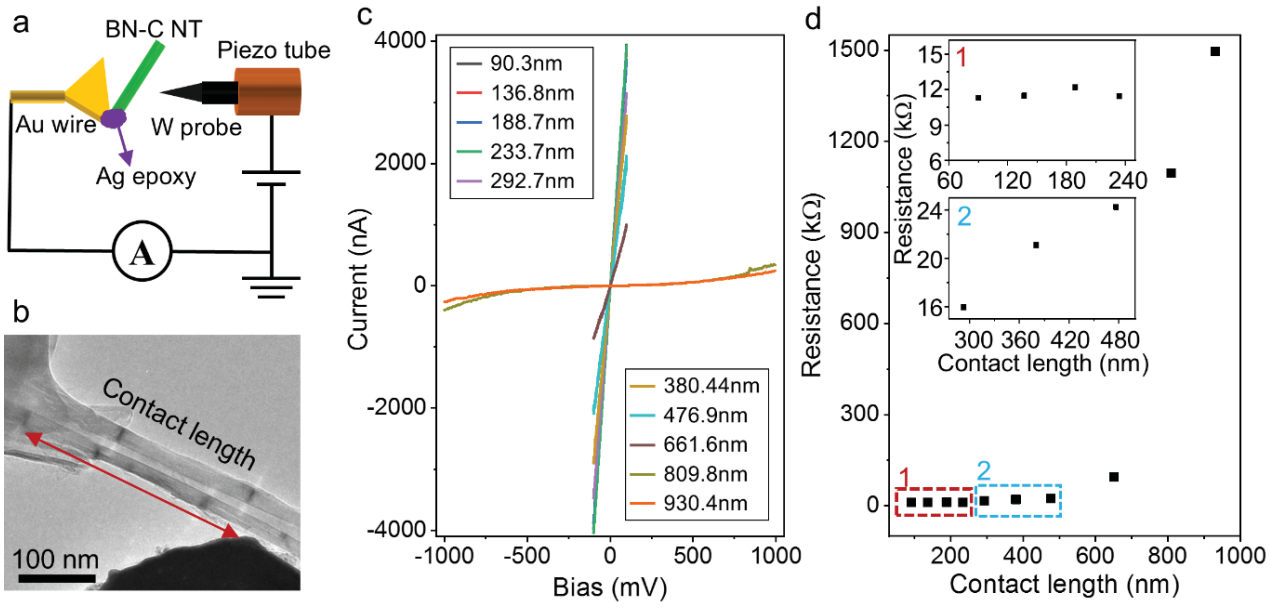

Figure 5.4 (a) Schematic drawing of the electrical measurement on an individual coaxial BN-C nanotube. (b) TEM image of the selected BN-C nanotube contacted by the sharp W probe; the contact length denotes the

nanotube length between the Au support and W probe. (c) Representative *I-V* curves of the BN-C nanotube at different contact lengths. (d) Relationship between the nanotube resistances and the contact length. Insets in (d) are the enlarged regions marked by the colored rectangles, showing the ballistic (red) and diffusive (blue) transport modes.

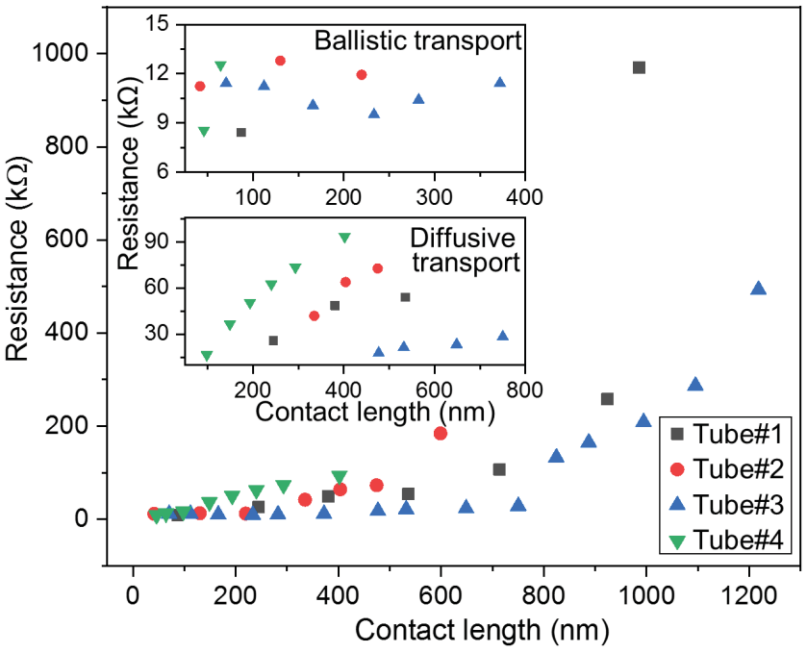

Figure 5.5 Resistance *vs* contact length plots for different nanotubes, indicating a nonlinear behavior for the hybrid BN-C nanotube.

5.3.4 Bending effect on transport properties of BN-C nanotubes

The experiments clearly show that the transport in BN-C nanotubes is remarkably enhanced as compared to pure BNNTs, which are electrically insulating. For the potential applications in flexible electronics, a stable transport is undoubtedly preferable. To understand how the external mechanical deformations influence the atomic structure and electrical properties, the structural evolution observations in-tandem with in parallel *I-V* curve recording and tube resistance measurements were performed under *in situ* bending in TEM (**Figure 5.6**). A series of TEM images, shown in **Figure 5.6a**, illustrates a structural evolution during deformation. Under moving the W probe forward, the hybrid BN-C nanotube first undergoes structural changes *via* generation of a sharp kink,(**Figure 5.6b**) instead of uniform arc-like tube bending as a whole.[27] Once the kink appears, further deformation develops *via* increasing the kink angle, which can reach a value of up to ~67.2°. The corresponding *I-V* curves recorded at different bending angles are presented in **Figure 5.6c**, showing that the output current only marginally changes (from -1.1% to 7.2%). Such small variations can be ascribed to the slight contact condition changes (between the W probe and the nanotube). Importantly, though both core BN and covering C layers are severely deformed and intertwined, the kink immediately disappeared and the nanotube entirely recovered to its initial state (both structurally and electrically) once the probe had been retracted (**Figure 5.7**). Thus, neglecting the marginal contact changes, the present BN-C tube shows quite

stable transport behavior under bending. **Figure 5.6d** depicts the relationship between resistances and bending angles of the nanotubes showing different transport characteristics. No matter what type of transport is dominating, *i.e.* the ballistic, diffusive or hopping, the resistances vary within a very small range, implying that the deformation does not dramatically enhance carrier scattering (**Figure 5.8**). These results indicate that the present BN-C heterostructures should be of advantageous use for novel flexible devices that can withstand exceptionally high bending strains.

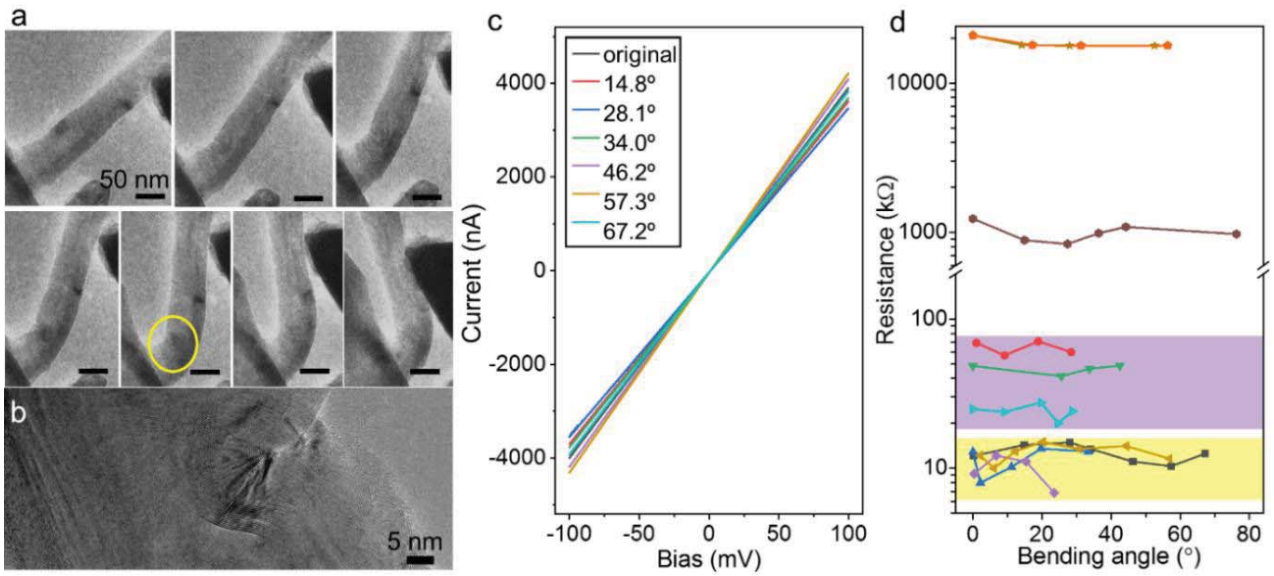

Figure 5.6 (a) Sequential TEM images of a selected BN-C nanotube showing its bending process. (b) High-resolution TEM image of the marked region in (a), confirming a severe deformation for both core BN and outer C layers. (c) A series of *I-V* curves recorded from the same BN-C nanotube in (a) at different bending angles; (d) Dependence of resistance of different BN-C nanotubes against their bending angles.

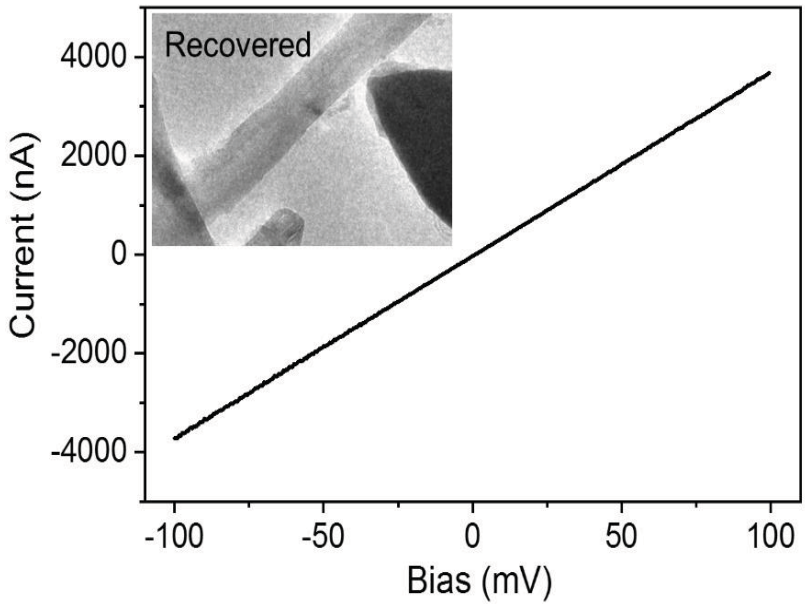

Figure 5.7. *I-V* curve and TEM image (inset) revealing that the BN-C nanotube fully recovers both structurally and electrically after severe deformation.

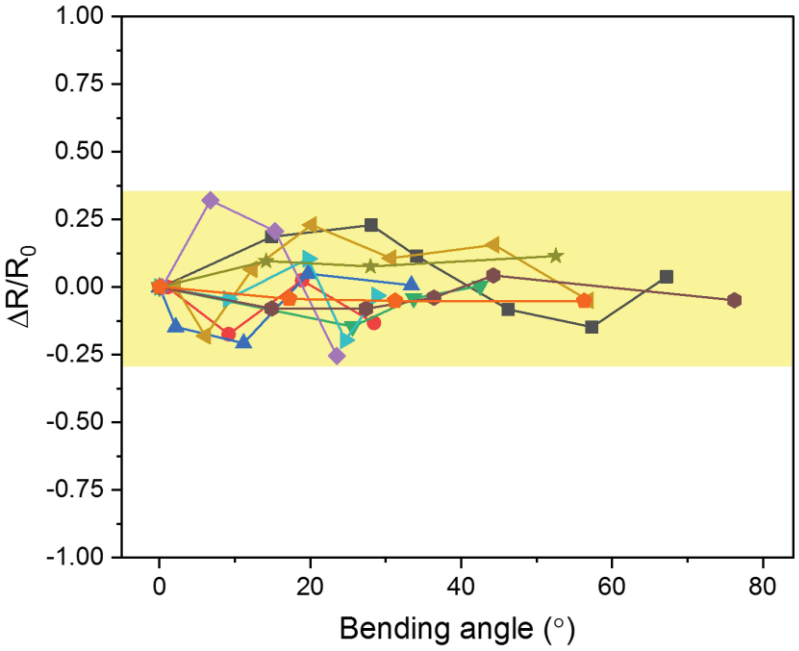

Figure 5.8 Variation of *ΔR* for BN-C nanotubes showing different transport behaviors at different bending angles. The variation of resistance doesn't show an obvious trend, but the average variation is about 0.7 %, implying the stable transport behavior.

5.3.5 Comparative study on transport properties of BNNTs and CNTs

In addition, comparative studies on the transport properties of BNNTs and CNTs as a function of the contact length, as well as the bending angles were conducted. The results are shown in Figure 5.10. For BNNTs, even at large bias range, the *I-V* curves at different contact lengths show purely insulating characteristics (**Figure 5.9a**), and these are not affected by bending. (**Figure 5.9b**). For CNTs, all the recorded *I-V* curves at different contact lengths exhibit linear characteristics (**Figure 5.9c**). The relationships between the resistances of CNTs and the contact lengths reveal that these CNTs only show ballistic and diffusive transport characteristics, without switching to the hopping transport regime, which is different from the coaxial BN-C hybrid nanotubes (**Figure 5.9d**). This difference can be understood based on structural integrity. Within the large length range BN-C nanotubes are not entirely covered with carbon shells, some carbon islands form instead, leading to the appearance of the hopping transport. However, the CNTs have well-crystalline shells that ensure that they are able to keep the diffusive transport over long distances. In the meantime, the bending effect on the transport properties of CNTs was also studied. The corresponding *I-V* curves for CNTs recorded at different bending angles are shown in **Figure 5.9e**, revealing that the output current exhibits only minor changes (from -0.6% to 5.6%). Such small variations can be ascribed to the slight contact condition changes. A summary of the resistances of different CNTs as a function of bending angles is depicted in **Figure 5.9f**, showing that the CNTs can keep their transport features without being severely affected by bending.

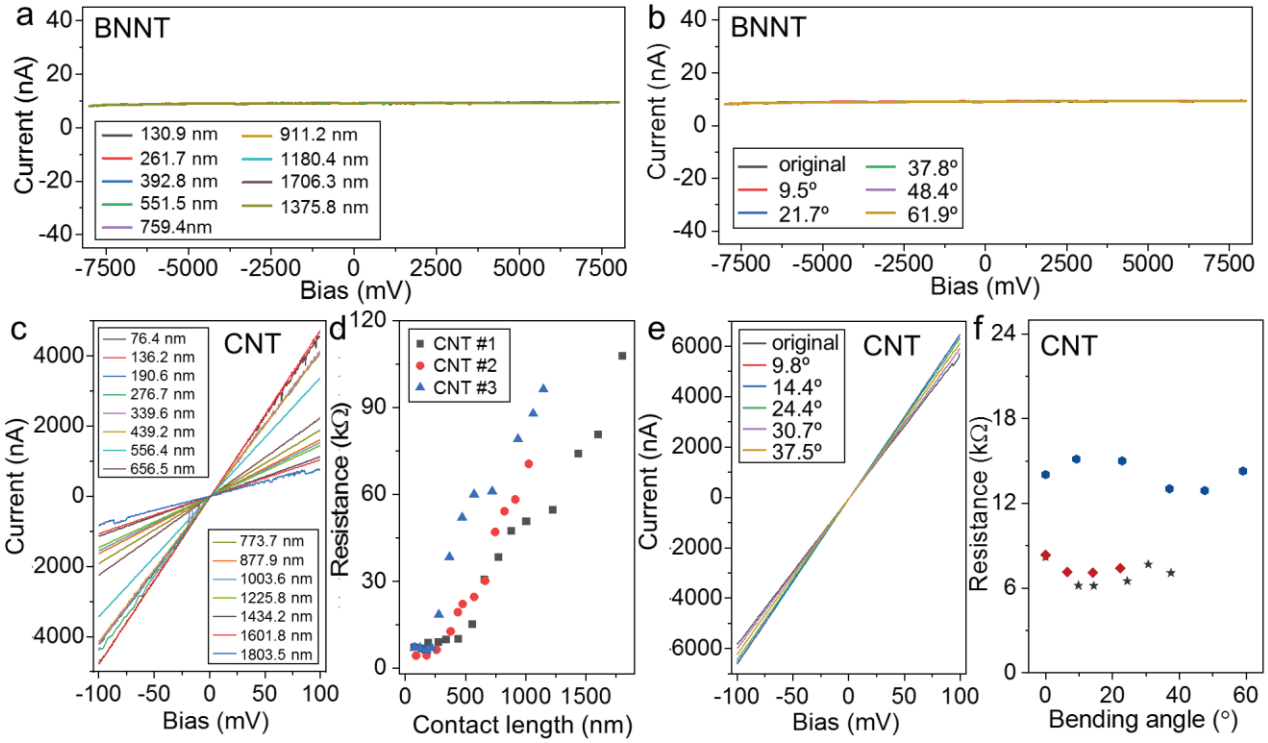

Figure 5.9 (a) and (b) *I-V* curves recorded from an individual BNNT as a function of contact length and bending angle, respectively. (c) Representative *I-V* curves of a CNT at different contact lengths. (d) Relationship between the resistances of CNTs and the contact length, only shows the ballistic and diffusive transport modes. (e) A series of *I-V* curves recorded from the same individual CNT at different bending angles; (f) Dependence of resistance of different CNTs against their bending angles.

5.3.6 Understand the fundamental from the perspective of theoretical calculation

To obtain fundamental insights into both electrical and mechanical properties of hybrid BN-C nanotubes under external loading, direct simulation of the bending process was performed. Unlike CNTs, BNNTs may have a polygonal cross-section caused by interlayer electrostatic interactions that are sufficient to induce the interwall correlation, which will undoubtedly affect their mechanical and electronic properties. Thus, first, we studied in detail the features of the atomic structure of hybrid nanotubes having a BNNT core and a CNT shell (**Figure 5.10**). Here we considered only "zigzag" nanotubes, due to the fact that in the previous studies[28] it was predicted that only zigzag nanotubes could form a polygonal cross-section, while, in case of the armchair and chiral nanotubes, polygonization could change and even disappear. Theoretical calculations show that the polygonal shape of the BN core is transmitted to the outer C layers. As a result, external CNT cross-section also becomes a polygon. Our calculations show that the polygonal shape of the inner BNNT influences the C shell only up to four outer C layers. After 4 layers the outer shell polygonization effect mostly vanishes.

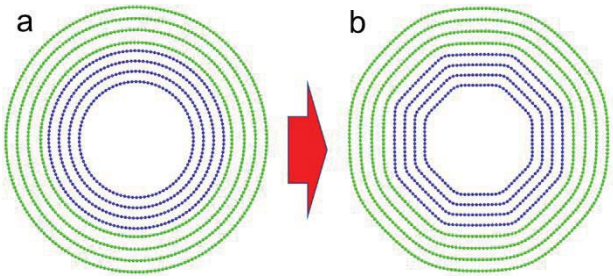

Figure 5.10 Atomic structure of a hybrid BN-C nanotube (cross-sectional view, BN-blue, C-green) before (a) and after (b) geometry relaxation.

In addition to changes in the atomic structure, the polygonization effect can affect the mechanical properties of hybrid nanotubes. The presence of edges in the structure of polygonal nanotubes can initiate anisotropy in behavior under mechanical loading. Therefore, we performed MD calculations of transverse compression of hybrid BN-C nanotubes in various directions and found that the formed polygons only slightly influence the hybrid tube behavior under external transverse mechanical stresses (the slopes of the curves are similar, **Figure 5.11**).

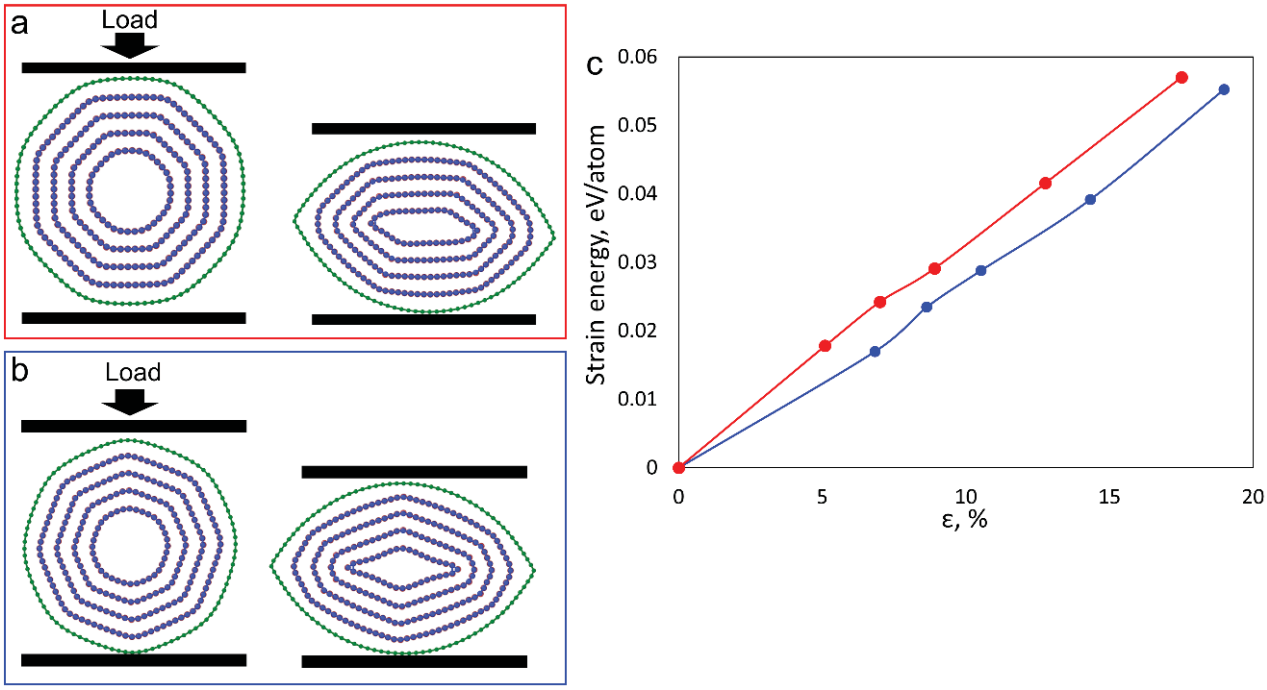

Figure 5.11 (a) and (b) Initial and final geometries of hybrid BN-C nanotubes before and after transverse compression with different load directions; (c) The dependence of the strain energy of nanotube on the strain. The red and blue lines correspond to the compression directions presented in (a) and (b), respectively. BN-purple layers, green - C layers.

We then elucidated the behavior of hybrid coaxial BN-C nanotubes under bending at the atomic level by performing large-scale MD simulations. We studied hybrid structures with various diameters, lengths, and the number of layers. Close to the experimental procedure, we considered the stepwise tip movement, which is associated with the consecutive movement of the tip in the horizontal direction and, then, in the vertical

direction. In order to directly compare our calculation results with the experimental data on the same plot, we used a dimensionless D/L ratio between tube diameter (D) and its length (L). According to experimental data in the considered model, one end of the tube was fixed, while the force was applied to another end. It this case the length of the tube and the applied force position are both defined as *L*. It should be noted that during test calculations it was found that the shift of the tip position leads to the variation of the kink position. The shift of the applied force toward the fixed end of the tube allows us to consider such a process similarly to a bending process of the shorter hybrid tube. Such parameter allows us to analyze properties of structures with sufficiently different sizes and, therefore, is very useful in the comparison between larger experimental structures and studied computational models. Figure 5.13a and b show two hybrid nanotubes with the same number of C and BN layers (2 C layers and 2 BN layers) but with a difference in the D/L ratio (0.16 and 0.08). Under the stress loading process, in case of a smaller D/L value, a nanotube kink (L_{kink}) appears closer to the nanotube center, while the kink for the tube with a larger D/L value is located closer to the fixed end. General correspondence of theory with the experiments is illustrated by the recorded BN-C nanotubes bending processes in **Figure 5.12c**. Even at the critical ratio of bending there are no defects formed (**Figure 5.12a** and **b**). These simulation results suggest the reason behind the excellent structural flexibility during bending. In **Figure 5.12d** the dependence of the nanotube kink position, described as the L_{kink}/D ratio on the D/L ratio is presented. Here, the calculated data obtained from MD calculations (red circles) show the behavior of small hybrid nanotubes, whereas experimental data expand this dependence toward the larger nanotubes (blue squares). Red dots correspond to theoretical results of kink position estimation for hybrid nanotubes with a various number of layers varied from 4 to 9 (from 2 BN and 2 C to 3 BN and 6 C layers). With decreasing the D/L ratio the kink position monotonically shifts and approaches the middle of the tube. Based on MD simulations it could be concluded that the main geometrical parameter, which is responsible for the kink position during bending, is indeed the D/L ratio. This fact originates from a competition of the moment of inertia and nanotube bending stiffness. Moreover, decreasing the number of inner BN layers within hybrid BN-C nanotubes does not lead to the changes in the position of the kink, while the overall mechanical response could be significantly different.

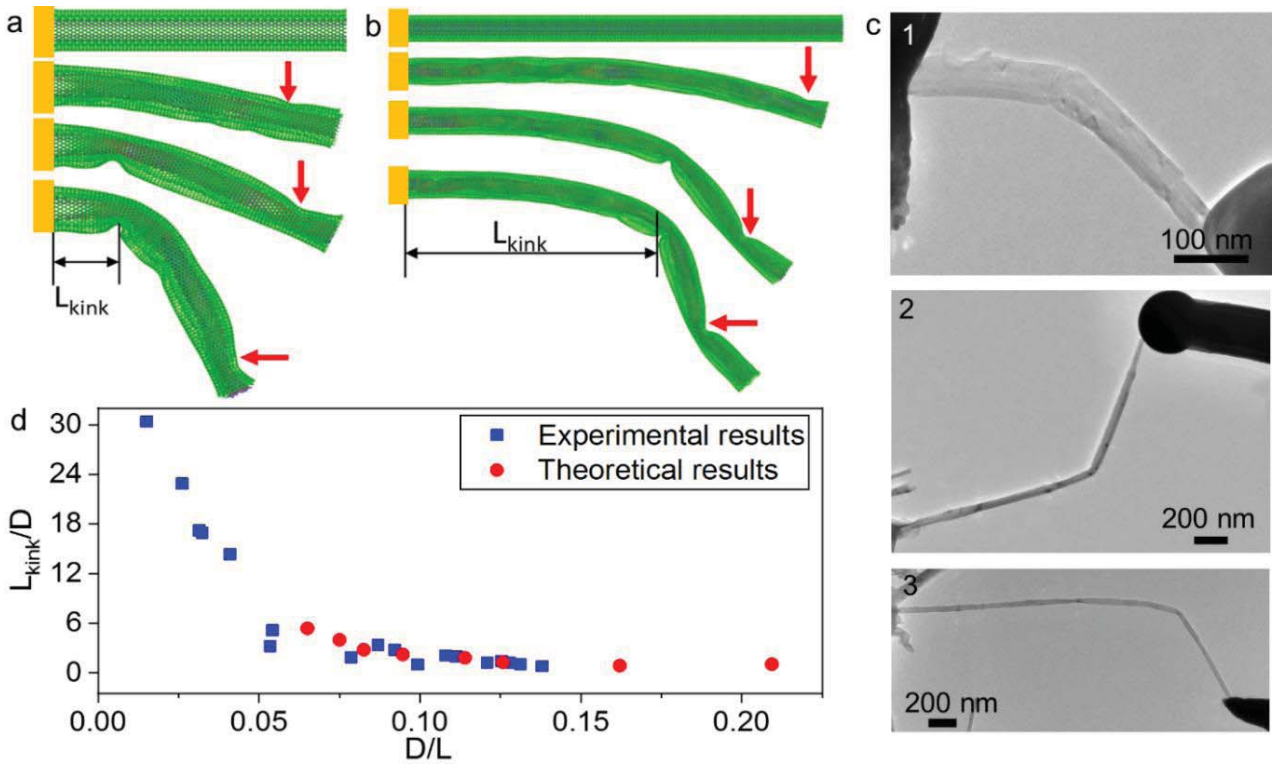

Figure 5.12 Main steps of a hybrid BN-C bending process exemplified by coaxial nanotubes with 2 inner BN layers and 2 outer C layers (diameter of 2.8 nm) with a length of (a) 17 nm and (b) 45 nm. Schematic representation of the external acting force is presented by red arrows; (c) Experimental TEM images of bent hybrid BN-C nanotubes with various lengths and diameters. (d) Dependence of the L_{kink}/D ratio on the D/L ratio for hybrid nanotubes. Calculated and experimental data are shown by red and blue symbols.

Significant bending of hybrid BN-C nanotubes can significantly impact their local electronic properties in the vicinity of a kink region (**Figure 5.13**). We found that in the critical bending regime the distance between the layers in the multiwalled hybrid nanotubes significantly decreases (from 3.35 Å to 2.17 Å), but the misorientation of atomic layers hinders the phase transition activation. The reduction tendency of the interlayer distance in the kinking regions was further confirmed by the HRTEM observation (**Figure 5.14**). Nevertheless, such a phenomenon leads to strong redistribution of electronic density between layers, which contributes to the formation of local conductive channels near the kink area (**Figure 5.13a**). Indeed, systematic study of electron density evolution upon decreasing the regarded distance for the case of 2 C layers covered on 2 BN layers shows strong charge redistribution and joint electron density between the layers when the distance is reduced to 2.17 Å. In **Figure 5.13b** the electron density distribution in the $e/Å^3$ units between C and BN layers upon the interlayer distance decrease is presented. In **Figure 5.13a** we show a slice of electron density in the middle of a coaxial BN-C tube. The formation of the joint electron density from all layers of BN-C tubes from the inner side of the kink area is apparent. Strong interaction between the layers is also observed within the kink area thus shrinking the distance. Such a reduction of the distance between the nanotube walls could lead to an interesting physical property change *via the* formation of quantum dots in the kink regions. Such

phenomenon may be important for future applications of the present hybrid nanotubes in advanced optical and optoelectronic fields.

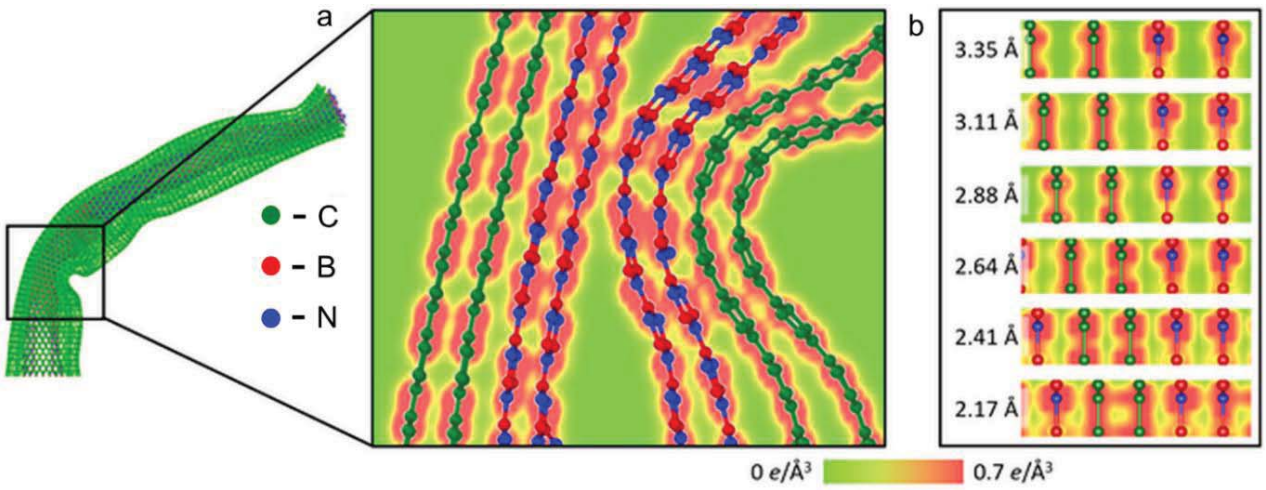

Figure 5.13 (a) Analysis of the kink area of a hybrid coaxial BN-C nanotube with 2 BN and 2 C walls. (b) The magnified image of the atomic structure within the formed kink. (b) Dependence of electron density distribution on the distance between the tubular walls. B, N and C atoms are depicted by red, blue and green colors.

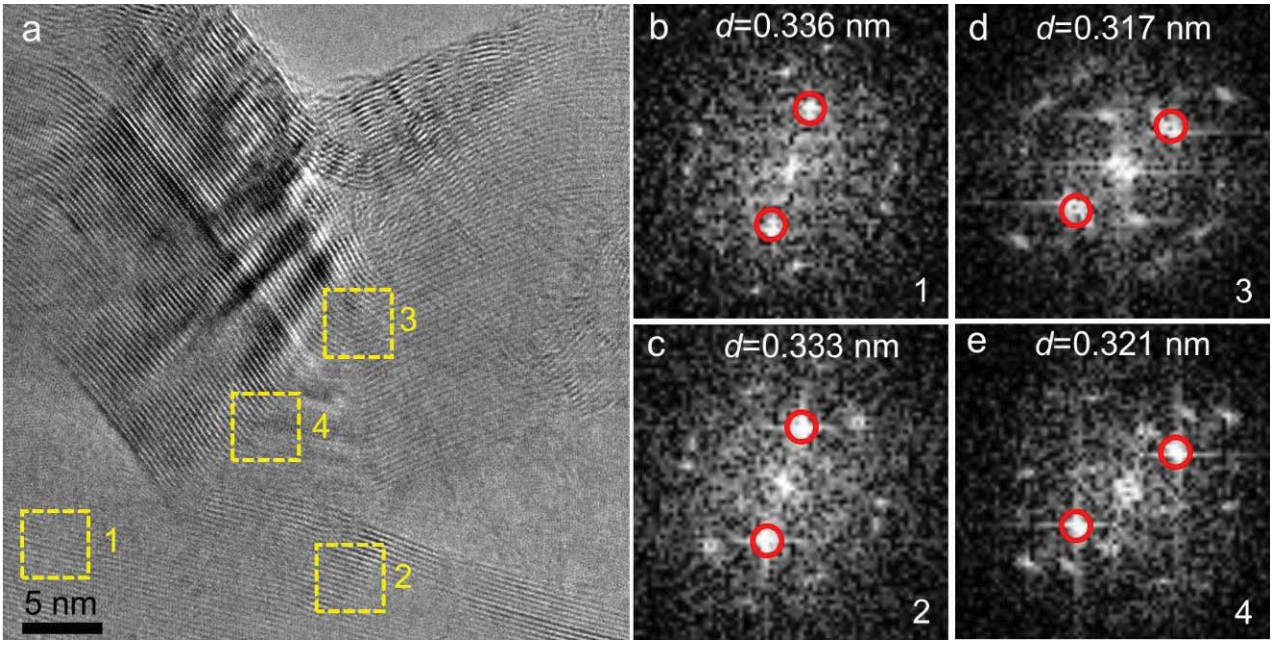

Figure 5.14 (a) High-resolution TEM image of the kinked region. (b-e) Fast Fourier transform (FFT) patterns corresponding to the marked regions in (a). The interlayer distance was calculated for the spots marked by red circles. It was found that the layer spacing is reduced from the pristine value of around 0.335 nm (b and c) to 0.317 nm (d) and 0.321 nm (e) in the marked kink region. These experimental observations agree well with the reduction tendency of the layer distance in the kink areas, exactly as predicted by the theoretical calculations.

5.4 Summary

In summary, we designed core-shell hybrid BN-C nanotubes and studied their mechanical and electrical properties under bending to further promote their potential applications in flexible devices. *In situ* TEM investigations revealed that such nanotubes possess a nonlinear transport behavior along their lengths. The effects of peculiar kinking deformation on both structural and electrical parameters were analyzed in detail. It has been found that even the sharp kinks appeared, the transport behavior was not notably affected. Importantly, the tubes could fully recover their shape after bending, implying their excellent structural flexibility. Computations showed that the kink positions had closely been related to the tube geometrical parameter, *i.e.* tube diameter to its length ratio, which is in good agreement with the *in situ* TEM bending tests. In the meantime, the analysis of atomic structures in the kink area confirmed the absence of permanent structural defects and full structural recovery of the tubes. Bending led to significant redistribution of electron density between the layers which could be directly connected with the formation of quantum dots in the kink regions.

5.5 References

(1) Lin, C.-H.; Fu, H.-C.; Cheng, B.; Tsai, M.-L.; Luo, W.; Zhou, L.; Jang, S.-H.; Hu, L.; He, J.-H. A Flexible Solar-Blind 2D Boron Nitride Nanopaper-Based Photodetector with High Thermal Resistance. *npj 2D Mater. Appl.* **2018**, *2* (1), 1-6.

(2) Zubair, A.; Wang, X.; Mirri, F.; Tsentalovich, D. E.; Fujimura, N.; Suzuki, D.; Soundarapandian, K. P.; Kawano, Y.; Pasquali, M.; Kono, J. Carbon Nanotube Woven Textile Photodetector. *Phys. Rev. Mater.* **2018**, *2* (1), 1-8.

(3) Gao, W.; Ota, H.; Kiriya, D.; Takei, K.; Javey, A. Flexible Electronics toward Wearable Sensing. *Acc. Chem. Res.* **2019**, *52* (3), 523-533.

(4) Hernández, E.; Goze, C.; Bernier, P.; Rubio, A. Elastic Properties of C and $B_xC_yN_z$ Composite Nanotubes. *Phys. Rev. Lett.* **1998**, *80* (20), 4502-4505.

(5) Yu, M.; Lourie, O.; Dyer, M. J.; Moloni, K.; Kelly, T. F.; Ruoff, R. S. Strength and Breaking Mechanism of Multiwalled Carbon Nanotubes Under Tensile Load. *Science*, **2000**, *287*, 637-641.

(6) Yu, M.-F.; Files, B. S.; Arepalli, S.; Ruoff, R. S. Tensile Loading of Ropes of Single Wall Carbon Nanotubes and Their Mechanical Properties. *Phys. Rev. Lett.* **2000**, *84* (24), 5552-5555.

(7) Arenal, R.; Wang, M. S.; Xu, Z.; Loiseau, A.; Golberg, D. Y Suryavanshi Boron Nitride Nanotubes. *Nanotechnology* **2011**, *22* (26).

(8) Kudin, K. N.; Scuseria, G. E.; Yakobson, B. I. BN, and C Nanoshell Elasticity from Ab Initio Computations. *Phys. Rev. B - Condens. Matter Mater. Phys.* **2001**, *64* (23), 1-10.

(9) Lee, C. H.; Xie, M.; Kayastha, V.; Wang, J.; Yap, Y. K. Patterned Growth of Boron Nitride Nanotubes by Catalytic Chemical Vapor Deposition. *Chem. Mater.* **2010**, *22* (5), 1782-1787.

(10) Cohen, M. L.; Zettl, A. The Physics of Boron Nitride Nanotubes. *Phys. Today* **2010**, *63* (11), 34-38.

(11) Lu, X.; Chen, Z. Curved Pi-Conjugation, Aromaticity, and the Related Chemistry of Small Fullerenes (< C60) and Single-Walled Carbon Nanotubes. *Chem. Rev.* **2005**, *105* (10), 3643-3696.

(12) Laird, E. A.; Kuemmeth, F.; Steele, G. A.; Grove-Rasmussen, K.; Nygard, J.; Flensberg, K.; Kouwenhoven, L. P. Thune, E.; Strunk, C. Quantum Transport in Carbon Nanotubes. *Rev. Mod. Phys.* **2015**, *87* (3), 703-764.

(13) Ban, C.; Li, L.; Wei, L. Electrical Properties of O-Self-Doped Boron-Nitride Nanotubes and the Piezoelectric Effects of Their Freestanding Network Film. *RSC Adv.* **2018**, *8* (51), 29141-29146.

(14) Bai, X.; Golberg, D.; Bando, Y.; Zhi, C.; Tang, C.; Mitome, M.; Kurashima, K. Deformation-Driven Electrical Transport of Individual Boron Nitride Nanotubes. *Nano Lett.* **2007**, *7* (3), 632-637.

(15) Wang, W.; Bando, Y.; Zhi, C.; Fu, W.; Wang, E.; Golberg, D. Aqueous Noncovalent Functionalization and Controlled Near-Surface Carbon Doping of Multiwalled Boron Nitride Nanotubes. *J. Am. Chem. Soc.* **2008**, *130* (26), 8144-8145.

(16) Zeng, H. B.; Zhi, C. Y. ; Zhang, Z. H.; Wei, X. L.; Wang, X. B.; Guo, W. L.; Bando, Y.; Golberg, D. "White Graphenes": Boron Nitride Nanoribbons *via* Boron Nitride Nanotube Unwrapping. *Nano Lett.* **2010**, 5049-5055.

(17) Zhang, Z.; Guo, W. Energy-Gap Modulation of BN Ribbons by Transverse Electric Fields: First-Principles Calculations. *Phys. Rev. B - Condens. Matter Mater. Phys.* **2008**, *77* (7), 1-5.

(18) Ayala, P.; Arenal, R.; Loiseau, A.; Rubio, A.; Pichler, T. The Physical and Chemical Properties of Heteronanotubes. *Rev. Mod. Phys.* **2010**, *82* (2), 1843-1885.

(19) Xiang R, Inoue T, Zheng Y, Kumamoto A, Qian Y, Sato Y, Liu M, Gokhale D, Guo J, Hisama K, Yotsumoto S, Ogamoto T, Arai H, Kobayashi Y, Zhang H, Hou B, Anisimov A, Miyata Y, Okada S, Chiashi S, Li Y, Kong J, Kauppinen E I, Ikuhara Y, Suenaga K and Maruyama. One-Dimensional van Der Waals Heterostructures. arXiv:1807.06154.

(20) Jing, L.; Tay, R. Y.; Li, H.; Tsang, S. H.; Huang, J.; Tan, D.; Zhang, B.; Teo, E. H. T.; Tok, A. I. Y. Coaxial Carbon@boron Nitride Nanotube Arrays with Enhanced Thermal Stability and Compressive Mechanical Properties. *Nanoscale* **2016**, *8* (21), 11114-11122.

(21) Tang, C. C.; Bando, Y.; Sato, T.; Kurashima, K. A Novel Precursor for Synthesis of Pure Boron Nitride Nanotubes. *Chem. Commun.* **2002**, *2* (12), 1290-1291.

(22) Zhou, X.; Hsia, F.-C.; Xue, Y. M.; Tang, D.-M.; Cretu, O.; Zhang, C.; Mitome. M.; Bando, Y.; Sasaki, T.; Golberg, D. Tunable Mechanical and Electrical Properties of Coaxial. *Phys. Status Solidi RRL.* **2018**, *1800576*, 1-7.

(23) Leven, I.; Maaravi, T.; Azuri, I.; Kronik, L.; Hod, O. Interlayer Potential for Graphene/h-BN Heterostructures. *J. Chem. Theory Comput.* **2016**, *12* (6), 2896-2905.

(24) Leven, I.; Azuri, I.; Kronik, L.; Hod, O. Inter-Layer Potential for Hexagonal Boron Nitride. *J. Chem. Phys.* **2014**, *140* (10), 104106.

(25) Plimpton, S.; Fast Parallel Algorithms for Short-Range Molecular Dynamics, *J. Comput. Phys.* **1995**, *117*, 1-19.

(26) Tersoff, J. New Empirical Approach for the Structure and Energy of Covalent Systems, *Phys. Rev. B* **1988**, *37* (12), 6991-6999.

(27) KInacI, A.; Haskins, J. B.; Sevik, C.; ÇağIn, T. Thermal Conductivity of BN-C Nanostructures. *Phys. Rev. B - Condens. Matter Mater. Phys.* **2012**, *86* (11), 1-8.

(28) Soler, M.; Artacho, E.; Gale, J. D.; Garc, A.; Junquera, J.; Ordej, P.; Daniel, S. The SIESTA Method for Ab Initio Order-N Materials. *J. Phys. Cond. Mat.* **2002**, *14* (11), 2745-2779.

(29) Kim, S. Y.; Park, J.; Choi, H. C.; Ahn, J. P.; Hou, J. Q.; Kang, H. S. X-Ray Photoelectron Spectroscopy and First Principles Calculation of BCN Nanotubes. *J. Am. Chem. Soc.* **2007**, *129* (6), 1705-1716.

(30) Arenal, R.; Blase, X.; Loiseau, A. Boron-Nitride and Boron-Carbonitride Nanotubes : Synthesis, Characterization and Theory. *Adv. Phys*. **2010**, *59*, 101-179.

(31) Nakanishi, R.; Kitaura, R.; Warner, J. H.; Yamamoto, Y.; Arai, S.; Miyata, Y.; Shinohara, H. Thin Single-Wall BN-Nanotubes Formed inside Carbon Nanotubes. *Sci. Rep.* **2013**, *3*, 3-8.

(32) Dresselhaus, G.; Riichiro, S. Physical properties of carbon nanotubes. *World Scientific*, **1998**.

(33) Liu, H. D.; Zhao, Y. P.; Ramanath, G.; Murarka, S. P.; Wang, G. C. Thickness Dependent Electrical Resistivity of Ultrathin (<40 nm) Cu Films. *Thin Solid Films* **2001**, *384* (1), 151-156.

(34) Pablo, P. J.; Gómez-Navarro, C.; Colchero, J.; Gómez-Herrero, J.; Baró, A. M.; Serena, P. A. Nonlinear Resistance versus Length in Single-Walled Carbon Nanotubes. *Phys. Rev. Lett.* **2002**, *88* (3), 4-10.

(35) Huang, Y.; Lin, J.; Zou, J.; Wang, M. S.; Faerstein, K.; Tang, C.; Bando, Y.; Golberg, D. Thin Boron Nitride Nanotubes with Exceptionally High Strength and Toughness. *Nanoscale* **2013**, *5* (11), 4840-4846.

(36) Golberg, D.; Mitome, M.; Bando, Y.; Tang. C. C.; Zhi, C. Y. Multi-Walled Boron Nitride Nanotubes Composed of Diverse Cross-Section. *Appl. Phys. A* **2007**, *352*, 347-352.

Chapter 6

Conclusions and Outlook

Boron nitride nanotubes (BNNTs) are important functional materials and promising candidates for applications in diverse fields, especially for mechanical applications in extreme environments, since BNNTs are as mechanically strong as the CNTs, but chemically inert, as opposed to CNTs. However, up to now, several issues on the research of BNNTs have still been not well-understood: (1) Intrinsic elastic properties have not been precisely evaluated; (2) Effects of extrinsic defects on the mechanical properties of BNNTs are not studied, which is important for their space shielding application; (3) Effects of composition on tuning their electro-mechanical properties have not been realized, and still the large bandgap and electrical insulating characteristic largely block their applications in flexible devices; (4) The response of transport properties of the BN-C heterostructure to mechanical bending has not been established. Despite these aspects, when the structure decreases to a nanoscale size, the issues of how to 'see, fix, manipulate, apply load' to the target are preventing us from getting deep insight into its properties. In the meantime, with further explorations, it's been revealed that the size, crystal orientations, interfaces, as well as defects play essential roles in determining the mechanical properties of a nanomaterial. Thus, it becomes challenging, yet essential, to develop a precise measurement method for the material properties when it comes to the nanoscale size. Nowadays, several microscopic measurement methods have been developed to understand the mechanical and electrical behaviors of 1D nanomaterials. Among these methodologies, *in situ* TEM has the advantages of high spatial resolution, real-time imaging and spatially-resolved chemical analysis, which provide us with a perfect platform to understand the structure-properties-processing relationships of nanomaterials.

The presented Thesis used the advanced *in situ* TEM technique to study the mechanical properties of 1D BNNTs and realized the simultaneous electro-mechanical properties modulation *via* the design of coaxial BN-C heterostructures, and finally the transport properties of hybrid BN-C nanotubes to the mechanical bending were studied. The conclusions of this work are given in the following four segments:

(1) **Precise evaluation of the intrinsic elastic properties of BNNTs:** A high-order resonance method was developed to precisely evaluate the elastic properties of individual BNNTs, and up to 4th order resonances were observed for the first time. Significantly, the method exhibits an ultra-high precision (1 %). The average

modulus of BNNTs was evaluated to be 906.2 GPa with a standard deviation of ~ 8.9 %. In addition, a combination of the detailed structure investigation and statistical analysis let me understand that the intrinsic void defects are responsible for the modulus distribution. The technique provides a straightforward way to precisely determine the elastic properties of BNNTs, and can be also applied to other 1D structures.

(2) Defect effects on mechanical properties of BNNTs: Electron beam irradiation was applied to deliberately introduce defects into BNNTs to evaluate their space shielding application proposed by the National American Space Association (NASA). Surprisingly, during irradiation, the moduli of BNNTs decreased not continuously but reached a plateau, at a high modulus of ~ 662.9 GPa, 3 times that of steel (~220 GPa). In the meantime, a comparative study on carbon nanotubes (CNTs) revealed that the moduli of CNTs kept decreasing with the irradiation dose and CNTs exhibited a much more remarkable loss than that of BNNTs. This comparison clearly indicates that BNNTs have a superior capability with respect to radiation resistance. In addition, it was found that the fracture strength for BNNTs had been kept decreasing along with the irradiation dose. Interestingly, the reduction of the maximum force (40.5 %) was not as significant as the loss of the strength (53.4 %) implying that interlinking bridges may be formed between tube walls during irradiation.

(3) Tunable mechanical and electrical properties of coaxial BN-C heterostructures: An original way to synthesize novel BN-C nanotubes with high quality was invented. Instead of constant elastic moduli and resistivities for CNTs and BNNTs, the elastic moduli of hybrid nanotubes could be tuned from ~140 GPa to ~700 GPa, and their electrical resistivities could be adjusted within three orders of magnitude, from ~0.16 Ω·m to ~2.5×10^{-4} Ω·m, just by changing the carbon shell thickness. The roles of carbon shells on modulating the electro-mechanical properties of coaxial BN-C nanotubes were well explained by a core-shell model and the proposed hopping mechanism, respectively.

(4) **Kinking effects and transport properties of coaxial BN-C nanotubes:** Coaxial BN-C nanotubes were fabricated and their intrinsic transport properties, as well as structural and electrical response to bending deformation, were studied inside a high-resolution transmission electron microscope. Ballistic, diffusive and hopping transports within different tube length ranges were observed. When a bending deformation had been applied to the tubes, though severe kinking became apparent, their transport properties were not notably affected. Meanwhile, both theoretical and experimental analyses confirmed that the kink positions are dependent on the ratio of tube diameter to its length. Possible formation of quantum dots, directly within the kink areas, was predicted through calculations of electron density redistribution between nanotube walls at bending.

This study demonstrated a versatile universal strategy, *i.e*. high-order-high frequency electric field-induced resonance method with a precision of 1% to investigate the elastic properties of 1D nanostructures. Combining with the high-resolution imaging, a deep insight into the effects of defects was obtained and correlated with the mechanical properties, which could guide the researchers and engineers toward a design of devices based on nanoarchitectures with optimal performances. On the other hand, the novel idea for the construction of 1D heterostructures to realize the modulation of various properties of the functional materials is critical for realizing their multiple functions. Being accompanied with a high-precision manipulation using *in situ* TEM

techniques, we may achieve the construction of 2D heterostructures inside TEM. This approach may help us solve many current problems peculiar to 2D heterostructure fabrication, *e.g*. lack of structural control during fabrication, or the limitations of hybrid materials with large lattice mismatch growth using the traditional CVD methods. Furthermore, *in situ* exploration of external stimuli, like applied strain, electric field, Joule heating, on tuning the electro-mechanical properties of 2D heterostructures should promote the establishment of clear structure-property relationships which is the Holy Grail of Materials Science.

List of Figures

Figure 1.12 (a-c) TEM images showing the introduction and growth of triangle-shaped vacancy defects under different irradiation stage. (d) Schematic illustration of a single vacancy in a single BNNT. (e) Schematic illustration of the growth direction of the irradiation-induced vacancy.

Figure 1.13 Elastic moduli and electric resistivities for various nanostructured materials.

Figure 2.1 Schematic illustration of BN nanotubes' synthesis.

Figure 2.2 (a) SEM image of as-prepared BNNTs. Inset is a photograph of BN sample. (b) and (c) XRD pattern and Raman spectrum of BNNTs.

Figure 2.3 (a) Low-magnification TEM image, (b) High-resolution TEM image, (e) Outer diameter distribution diagram for BNNTs. The inset in (a) is SAED pattern taken from BNNT.

Figure 2.4 Schematic of the experimental setup of *in situ* TEM high-order resonance for measuring the elastic moduli. BNNTs were attached to an Au support by silver epoxy. An Au probe, used as a counter electrode, was controlled by a piezo-motor. An arbitrary/function generator provides a sinusoidal signal. By carefully tuning the signal frequency, up to 4th order normal and parametric resonances were excited.

Figure 2.5 (a) Schematic drawing of the relation between the actual nanotube length (L) with the projected nanotube length (L_{TEM}) acquired under TEM imaging. (b) The relationship between nanotube lengths estimated from $L= (((D_{o\text{-}hm}/D_{o\text{-}lm})\cdot L_{TEM})^2+Z^2)^{1/2}$ and high order resonance.

Figure 2.6 (a) and (b) TEM images showing a BNNT resonating at natural (n=2) and parametric (n=1) modes of from 1st to 4th and 1st to 3rd orders. Node positions are marked by blue circles. (c) The plot of experimentally recorded and theoretically predicted resonance frequencies for each resonance mode and order.

Figure 2.7 (a) Resonance frequencies ratio between high order and 1st order resonance for five BNNTs at the natural resonance mode (n=1, integer i denotes different resonance orders). (b) Resonance frequencies ratio between parametric (n=1 and n=*4*) and natural resonances (n=2) at different orders for five different BNNTs, n denotes different resonance modes. The dashed line represents the theoretical value.

Figure 2.8 (a)-(e) Natural (n=2) and parametric (n=1 and n=4) resonance modes for 5 additional individual BNNTs at different resonance orders. Nodes in each resonance order and mode are marked by yellow circles.

Figure 2.9 (a-c) Elastic moduli distribution for 15 individual BNNTs acquired from 1st, 2^{nd,} and 3rd order resonance, respectively. The dashed line in each panel denotes the average value of elastic modulus. (d) Histograms showing the comparison of the elastic modulus distributions of BNNTs between our results and those reported in the literatures.

Figure 2.10 Resonances of three individual BNNTs with different moduli and HRTEM images showing the details of their structure. Cavities are marked by dashed yellow lines.

Figure 3.1 Schematic illustration of the experimental set-up for tensile test to evaluate the fracture strength of BNNTs: (a) for pristine BNNT, (b) the "sheath" of the BNNT in (a). The Au support or probe was manipulated

by a piezo-motor to perform the tensile test. And the loading force is recorded by a Si cantilever. (c) Optical microscope image of the sensing cantilever along with a reference cantilever.

Figure 3.2 (a) HRTEM images of an individual BNNTs during irradiation process; (b) Variation of inner diameters of 4 individual BNNTs along with increasing irradiation dose. D_{it} and D_i denote the inner diameter at different irradiation dose and original inner diameters, respectively; (c)The reduction of outer diameters of 4 individual BNNTs with increasing irradiation dose.

Figure 3.3 (a) The reduction of resonance frequencies of 4 individual BNNTs with increasing irradiation dose; (b) The relationship between elastic moduli of BNNTs and irradiation dose.

Figure 3.4 TEM images of the fractured BNNTs after the tensile test (upper panel), HRTEM images of the fractured BNNTs (middle panel), and time-force and time-stress curves of a pristine BNNT (a) and that subjected to different irradiation doses (b-d).

Figure 3.5 (a) Variation of the maximum force when the BNNT was fractured under a tensile test along with increasing the tube electron irradiation dose; (b) Reduction of fracture strength along with irradiation dose.

Figure 3.6 (a) TEM images showing the 1st and 2nd order resonances of a CNT. (b) A series of HRTEM images showing the structural evolution of a CNT during electron irradiation, corresponding to the points in (f). (c) Dependence of outer and inner diameters of CNTs on irradiation dose. (d) The reduction of resonance frequencies with increasing irradiation dose. (e) and (f) Modulus value change and reduction of modulus during irradiation.

Figure 3.7 A series of HRTEM images illustrating the structural evolution of a BNNT during electron beam irradiation, this reveals a continuously decreased outer diameter and formation of a defective surface layer with a thickness of ~ 3.2 nm.

Figure 3.8 Defects density as a function of irradiation dose. Defects density is estimated *via* knock-on displacement theory.

Figure 3.9 The elastic modulus of a defective shell evaluated from the steady modulus region for 4 BNNTs in Figure 4(c) *via* applying the core-shell model.

Figure 3.10 Comparison of shell thickness for BNNTs obtained from real-time HRTEM images (solid line) and the theoretical calculation results (dash line) *via* applying the core-shell model.

Figure 4.1 Schematic illustration of the core-shell BN-C nanotubes' synthesis.

Figure 4.2 (a) SEM image of core-shell BN-C nanotubes. Inset is the photograph of BN-C sample. (b) Raman spectrum of the sample.

Figure 4.3 (a) Low-magnification TEM image, (b) High-resolution TEM image, (c) Outer diameter distribution diagram of BN-C sample; (d) Comparision of EEL spectra for BNNTs and core-shell BN-C NTs, respectively. The inset in (a) is SAED pattern taken from the BN-C nanotube.

Figure 4.4 (a) HRTEM image of a BN-C nanotube. (b) ADF STEM image acquired next to the area in (a). (c) RGB composite map of the region in (b), showing the distribution of B (red), C (green) and N (blue) species. (d) Averaged EEL spectra extracted from the corresponding regions arrowed in (c). (e) Averaged concentration profiles extracted from the map in (c), perpendicular to the tube axis.

Figure 4.5 (a) Schematic drawing of the relation between the actual nanotube length (L) with the projected nanotube length (L_{TEM}) acquired under TEM imaging. (b) Comparison of the outer diameter at low-magnification (5k-10k, D_{lm}) and high-magnification (200k-300k, D_{hm}). The real nanotube length can be expressed as： $L=(((D_{hm}/D_{lm})\bullet L_{TEM})^2+Z^2)^{1/2}$ (c) Results of the length measurements obtained from the two-step calibration and from the second mode resonance.

Figure 4.6 (a) Photograph of the front end of the STM-TEM holder and the schematic drawing of the mechanical resonance of an individual core-shell BN-C nanotube. (b) TEM image of an individual cantilevered BN-C nanotube. (c) HRTEM image and (d) EEL spectrum of the BN-C tube chosen for resonant measurements. (e) The first and (f) second mode harmonic resonances of the BN-C nanotube.

Figure 4.7 (a) and (b) First and second mode harmonic resonances of the same nanotube with graphite layers coated (BN-C NT) and then removed. (c-e) Comparative HRTEM images and EEL spectra taken from the areas marked in (a) and (b), respectively. (f) Response curves of the nanotubes at their first mode resonance. The solid lines are Lorentzian fits for the data points. (g) Calculated relationship between the elastic modulus of 16 individual BN-C nanotubes and the relative coated C content (relative C content is calculated from the EELS quantification results and defined as the atomic ratio between C content and the total content of B, N and C).

Figure 4.8 (a) and (b) Elastic modulus and Q factors of three individual nanotubes with graphite layers coated and removed, respectively. (c) Schematic illustration of the core-shell composite nanotube model. (d) Elastic modulus of the coated graphite layers by using the core-shell model.

Figure 4.9 (a) Representative *I-V* curves of various individual BN-C nanotubes with different amounts of coated C (averaged values over the whole structures) and (b) relationship between effective resistivity and relative C content for individual BN-C nanotubes. Colored zones represent the areas where the surface graphitic domains are gradually forming and evolving (yellow), and where the formation of an external continuous graphitic shell has ultimately been achieved (purple).

Figure 4.10 (a) TEM image of a BN-C nanotube without bias applied. (b) and (c) TEM and HRTEM image of the same nanotube showing that the external C nanotube layers were damaged and “onion”-like C structures were formed on the BN surface after applying a high bias (10 V).

Figure 4.11 (a) Schmatic illustation of the graphite layers foramtion, from small islands to continuous layers. (b-d) TEM images showing the growth of graphite islands, connection of these islands and finally continous layers, respectively.

Figure 4.12 (a) TEM images showing consecutive contact points on an individual BN-C nanotube. (b) EEL spectra acquired from the marked regions in (a) revealing the variations in C content in these areas. (c) Recorded *I-V* curves corresponding to each of the points in (a). (d) Electrical resistance values calculated for some of the contact points in (a).

Figure 4.13 (a) TEM images showing consecutive contact points on an individual BN-C nanotube. (b) EEL spectra acquired from the marked regions in (a) revealing the variations in C content in these areas. (c) Recorded *I-V* curves corresponding to each of the points in (a). (d) Electrical resistance values corresponding to each of the contacts in (a).

Figure 4.14 Comparison of the present data with the previous reports on different materials (Au, [27,28] Ag, [29,30] Cu, [31] Al, [32,33] Pt, [34,35] and W [36,37] nanowires, CNTs, [17,38–44]BNNTs [45–48] and SiNW[49–52]) in terms of elastic moduli and electrical resistivities at room temperature (different characteristic regions are marked).

Figure 5.1 Low-magnification TEM (a) and high-resolution TEM image (b) of a core-shell sandwich-like coaxial BN-C nanotube showing perfect crystallinity. (c) ADF-STEM image acquired from a nanotube segment. (d-f) Spatially resolved EELS elemental maps corresponding to the image in (c) revealing B, N, and C species distribution. (g) EEL spectra extracted from the corresponding regions arrowed in (c).

Figure 5.2 (a) TEM image of a nanotube. (b) EEL spectra taken from the red circles marked regions in (a) before and after thermal treatment, showing that only BN peaks remained while the carbon signals disappeared.

Figure 5.3 (a) The linear fitting for the relationship between the total resistance and the contact length., showing that the contact resistance is about 14.2 kΩ. The total resistance was acquired from the *I-V* curves shown in Figure 5.4c. (b) The contact resistance distribution obtained from 5 individual BN-C nanotubes.

Figure 5.4 (a) Schematic drawing of the electrical measurement on an individual coaxial BN-C nanotube. (b) TEM image of the selected BN-C nanotube contacted by the sharp W probe; the contact length denotes the nanotube length between the Au support and W probe. (c) Representative *I-V* curves of the BN-C nanotube at different contact lengths. (d) Relationship between the nanotube resistances and the contact length. Insets in (d) are the enlarged regions marked by the colored rectangles, showing the ballistic (red) and diffusive (blue) transport modes.

Figure 5.5 Resistance *vs* contact length plots for different nanotubes, indicating a nonlinear behavior for the hybrid BN-C nanotube.

Figure 5.6. (a) Sequential TEM images of a selected BN-C nanotube showing its bending process. (b) High-resolution TEM image of the marked region in (a), confirming a severe deformation for both core BN and outer C layers. (c) A series of *I-V* curves recorded from the same BN-C nanotube in (a) at different bending angles; (d) Dependence of resistance of different BN-C nanotubes against their bending angles.

Figure 5.7. *I-V* curve and TEM image (inset) revealing that the BN-C nanotube fully recovers both structurally and electrically after severe deformation.

Figure 5.8 Variation of ΔR for BN-C nanotubes showing different transport behaviors at different bending angles. The variation of resistance doesn't show an obvious trend, but the average variation is about 0.7 %, implying the stable transport behavior.

Figure 5.9 (a) and (b) *I-V* curves recorded from an individual BNNT as a function of contact length and bending angle, respectively. (c) Representative *I-V* curves of a CNT at different contact lengths. (d) Relationship between the resistances of CNTs and the contact length, this only shows the ballistic and diffusive transport modes. (e) A series of *I-V* curves recorded from the same individual CNT at different bending angles; (f) Dependence of resistance of different CNTs against their bending angles.

Figure 5.10 Atomic structure of a hybrid BN-C nanotube (cross-sectional view, BN-blue, C-green) before (a) and after (b) geometry relaxation.

Figure 5.11 (a) and (b) Initial and final geometries of hybrid BN-C nanotubes before and after transverse compression with different load directions; (c) The dependence of the strain energy of nanotube on the strain. The red and blue lines correspond to the compression directions presented in (a) and (b), respectively. BN-purple layers, green - C layers.

Figure 5.12 Main steps of a hybrid BN-C bending process exemplified by coaxial nanotubes with 2 inner BN layers and 2 outer C layers (diameter of 2.8 nm) with a length of (a) 17 nm and (b) 45 nm. Schematic representation of the external acting force is presented by red arrows; (c) Experimental TEM images of bent hybrid BN-C nanotubes with various lengths and diameters. (d) Dependence of the L_{kink}/D ratio on the D/L ratio for hybrid nanotubes. Calculated and experimental data are shown by red and blue symbols.

Figure 5.13 (a) Analysis of the kink area of a hybrid coaxial BN-C nanotube with 2 BN and 2 C walls. (b) The magnified image of the atomic structure within the formed kink. (b) Dependence of electron density distribution on the distance between the tubular walls. B, N and C atoms are depicted by red, blue and green colors.

Figure 5.14 (a) High-resolution TEM image of the kinked region. (b-e) Fast Fourier transform (FFT) patterns corresponding to the marked regions in (a). The interlayer distance was calculated for the spots marked by red circles. It was found that the layer spacing is reduced from the pristine value of around 0.335 nm (b and c) to 0.317 nm (d) and 0.321 nm (e) in the marked kink region. These experimental observations agree well with the reduction tendency of the layer distance in the kink areas, exactly as predicted by the theoretical calculations.

List of Tables

List of Publications

1. Xin Zhou, Dai-Ming Tang, Masanori Mitome, Yoshio Bando, Takayoshi Sasaki, Dmitri Golberg. Intrinsic and Defect-Related Elastic Moduli of Boron Nitride Nanotubes As Revealed by *in Situ* Transmission Electron Microscopy. *Nano Letters,* 2019, 19, 4974-4980.

2. Xin Zhou, Feng-Chun Hsia, Yanming Xue, Dai-Ming Tang, Ovidiu Cretu, Chao Zhang, Masanori Mitome, Yoshio Bando, Takayoshi Sasaki, Dmitri Golberg. Tunable Mechanical and Electrical Properties of Coaxial BN-C Nanotubes. *Physica Status Solidi RRL: Rapid Research Letters*, 2018, 1800576.

3. Xin Zhou, Dmitry G. Kvashnin, Yanming Xue, Dai-Ming Tang, Ovidiu Cretu, Masanori Mitome, Yoshio Bando, Pavel B. Sorokin, Takayoshi Sasaki, Dmitri Golberg. Kinking Effects and Transport Properties of Coaxial BN-C Nanotubes As Revealed by *in Situ* Transmission Electron Microscopy and Theoretical Analysis. *APL Materials,* 2019*, Just Accepted.*

4. Yanming Xue, Xin Zhou, Tianzhou Zhan, Baozhen Jiang, Quansheng Guo, Xiuwei Fu, Kiyoshi Shimamura, Yibin Xu, Takao Mori, Pengcheng Dai, Yoshio Bando, Chengchun Tang, Dmitri Golberg, Densely Interconnected Porous BN Frameworks for Multifunctional and Isotropically Thermoconductive Polymer Composites, *Advanced Functional Materials*, 2018, 28, 1801205.

5. Haibo Tan, Jing Tang, Xin Zhou, Dmitri Golberg, Suresh K. Bhatia, Yoshiyuki Sugahara, Yusuke Yamauchi, Preparation of 3D Open Ordered Mesoporous Carbon Single-Crystals and Their Structural Evolution during Ammonia Activation, *Chemical Communications*, 2018, 54, 9494-9497.

6. Feng-Chun Hsia, Dai-Ming Tang, Wipakoran Jevasuwan, Naoki Fukata, Xin Zhou, Masanori Mitome, Yoshio Bando, Torbjorn E. M. Nordling, Dmitri Golberg, Realization and Direct Observation of Five Normal and Parametric Modes in Silicon Nanowire Resonators by *in Situ* Transmission Electron Microscopy. *Nanoscale Advances,* 2019, 1, 1784-1790.

7. Dai-Ming Tang, Dmitry G Kvashnin, Ovidiu Cretu, Yoshihiro Nemoto, Fumihiko Uesugi, Masaki Takeguchi, Xin Zhou, Feng-Chun Hsia, Chang Liu, Pavel B Sorokin, Naoyuki Kawamoto, Masanori Mitome, Hui-Ming Cheng, Dmitri Golberg, Yoshio Bando. Chirality Transitions and Transport Properties of Individual Few-Walled Carbon Nanotubes As Revealed by *in Situ* TEM Probing. *Ultramicroscopy*, 2018, 194, 108-116.

Acknowledgements

I deeply appreciate the strong help and support from many kind people during my three years of study in Japan. This dissertation could not have been completed without their warm support.

First and foremost, I would like to express my gratitude to my supervisors, Professor Takayoshi Sasaki and Professor Dmitri Golberg, for accepting me as a graduate student for the Joint Graduate Program between the University of Tsukuba and National Institute for Materials Science (NIMS), and for their support, guidance, patience, encouragement as well as criticism throughout my doctoral career. With their strong support, I have learned the basics about the advanced TEM technique, also the preparation of 2D nanosheets by chemical exfoliation, which is essential and meaningful for my research career. In addition to the scientific knowledge I have learned from them, the attitude of an independent researcher, the importance of personal responsibility and collaboration with other people. These are all valuable treasures to me.

I would like to express my sincere acknowledgement to Dr. Dai-Ming Tang and Dr. Ovidiu Cretu, for helping me so much in many facets of scientific research. They have taught me lots of experimental skills on the TEM and *in situ* holders. Also, I can always gain new ideas and knowledge from the discussion with them, which helps a lot to conduct the experiments smoothly. I would like to thank Mitome-san so much for solving technical problems with the microscope, to make sure all the experiments going well. I would also like to thank Prof. Yoshio Bando and Dr. Naoyuki Kawamoto for their kind help and advice.

I would like to give my sincere appreciate for their valuable suggestions and warm accompanies from the present and past members of at the International Center for Materials Nanoarchitectonics (MANA): Professor Renzhi Ma, Dr. Shisheng Li, Dr, Xinming Li, Dr. Xueyi Lu, Dr. Pan Xiong, Dr. Yeji Song, Dr. Chao Zhang, Dr. Min Zhou, Dr. Yanming Xue, Dr. Yanna Guo, Dr. Bo Jiang, Dr. Haibo Tan, Dr. Fengniu Lv, Dr. Xiaofang Jia, Dr. Xiuwei Fu, Mr. Akihiko Ohi, Ms. Yumiko Sawabe. Our philosophical debates, exchanges of knowledge, skills, and advice make my experience in Japan colorful.

I would also like to express my sincere acknowledgement to the professors of my defense committee: Professor Takao Mori, Professor Naoki Fukata, and Professor Takashi Sekiguchi. Their insightful comments and suggestions allowing me to get deeper understanding of the research and really helped a lot to improve the quality of this Thesis.

I also greatly appreciate Ms. Eiko Yokota, Ms. Shiina Kasaya and Ms. Ryoko Hayakawa for supporting me a lot in addressing official matters.

Finally, I would like to express my sincere gratitude to my family, for their endless encouragement, support, and love within the past three years